

Dissertation for the degree of doctor of philosophy

An Interacting Particle Model and Dynamic Energy Budget Theory: Analysis and Applications

Baldvin Einarsson



UNIVERSITY OF ICELAND

School of Engineering and Natural Sciences

Faculty of Physical Sciences

Reykjavík, April 2011

A dissertation presented to the University of Iceland School of Engineering and Natural Sciences in candidacy for the degree of doctor of philosophy

Doctoral committee

Prof. Björn Birnir

Department of Mathematics, University of California, Santa Barbara

Prof. Sven Sigurðsson

Faculty of Industrial Engineering, Mechanical Engineering and Computer Science, University of Iceland

Prof. Ragnar Sigurðsson

Faculty of Physical Sciences, University of Iceland

Opponents

Prof. José Antonio Carrillo de la Plata

Universidad Autonoma de Barcelona

Dr. Geir Huse

Institute of Marine Research in Norway

An Interacting Particle Model and Dynamic Energy Budget Theory:
Analysis and Applications

© 2011 Baldvin Einarsson

Printed in Iceland by Háskólaprent

Science Institute Report RH-01-2011

ISBN 978-9979-9953-8-8

Contents

Abstract	viii
Ágrip (in Icelandic)	x
Acknowledgements	xii
1 Introduction	1
1.1 Background	1
1.2 Outline of thesis	2
1.3 The Icelandic capelin	4
I Interacting particle models	7
2 Interacting particle model	9
2.1 Introduction	9
2.2 Model description	10
2.3 Basic equations of motion	11
2.3.1 Sensory zones	12
2.3.2 Directional heading determined by neighbors	14
2.4 The environment	15
2.4.1 Currents	15
2.4.2 Temperature	16

2.4.3	The directional angle with environmental influence	17
2.4.4	Equations of motion with the environment	18
2.5	Discussion	19
3	Case studies and sensitivity analysis	23
3.1	Introduction	23
3.2	Simulations of spawning migrations	24
3.2.1	Temperature and currents for the 2008 simulation	24
3.2.2	Parameter and simulation specifications	26
3.2.3	The 2008 case study	28
3.3	Sensitivity analysis	29
3.3.1	Scenarios	33
3.4	Discussion	35
4	Scaling of parameters	43
4.1	Introduction	43
4.2	Model description	44
4.3	Scaling arguments	46
4.3.1	Case study	47
4.4	Measures	49
4.4.1	Global order parameter, R	49
4.4.2	Average local order parameter, \bar{r}	50
4.4.3	Global versus local	51
4.4.4	Particle density and the radii	53
4.4.5	Average number of neighbors, \bar{n}	54
4.4.6	Relaxation times to equilibrium	55
4.5	Simulations	56
4.5.1	Scenarios (a)-(i)	57
4.6	Results	65
4.7	Discussion	72

II	Dynamic Energy Budget models	75
5	Dynamic Energy Budget (DEB) model	77
5.1	Introduction	77
5.2	DEB theory	79
5.2.1	The κ -rule:	80
5.2.2	State variables	80
5.2.3	Equations of the standard DEB model	83
5.2.4	Roe energy, E_r , and roe production	85
5.2.5	Arrhenius temperature	86
5.3	Measurements and DEB	87
5.3.1	Daily averages from the 1999-2000 season	88
5.3.2	Temperature estimates for the 1999-2000 season	88
5.3.3	Food availability	91
5.4	DEB and observed quantities	92
5.4.1	Physical length	92
5.4.2	Physical weight	93
5.4.3	Fat and roe content	94
5.4.4	Water content of roe	95
5.5	Results	96
5.6	Discussion	100
5.6.1	Low value of κ	101
5.6.2	Scatter in data plots	101
6	A model for the spawning migration of capelin	103
6.1	Speed and preferred speed	104
6.1.1	Speed of a particle during the 1999-2000 season	106
6.1.2	Reaction time τ_R	107
6.2	Preferred temperature range	108
6.3	New maps of currents	109
6.4	Discussion	113

7	Conclusions	115
A	Appendix A	119
A.1	State variables and basic equations	119
A.1.1	Reserve energy	119
A.1.2	Volume, V , and volumetric length, L	120
A.1.3	Maturity energy and reproduction energy	120
A.2	Further derivations	124
A.2.1	Assimilation and maintenance rates, p_A and p_M	124
A.2.2	Maximum length	124
A.2.3	Reserve energy density, $[E]$	125
A.2.4	Volumetric length, L	126
A.2.5	Maturity energy and reproduction energy	127
A.2.6	Primary parameters	130
A.2.7	Dimensionless state variables	131
B	Appendix B	133
B.1	DEB and von Bertalanffy growth equations	133

Abstract

An interacting particle model is described and applied to the Icelandic capelin stock (*Mallotus villosus*). Using available temperature data and approximated currents, and without using artificial forcing terms or a homing instinct, the model was able to reproduce the observed spawning migration routes for three different years, successfully predicting the route for 2008. By means of a sensitivity analysis the oceanic temperature and the balance between the influence of interaction among particles and the particles' response to temperature are identified as the control parameters most significant in determining the migration route. One significant contribution of the simulations is the inclusion of orders of magnitude more particles than similar models, which affects the global behavior of the model by propagating information about surrounding temperature through the school more efficiently. In order to maintain the same dynamics between different simulations, we argue a linear relationship between the time step, radii of interactions, and the spatial resolution, and we argue that these scale as $N^{-1/2}$, where N is the number of particles. In order to investigate this argument, several measures are presented and in turn analyzed, e.g. global and local order parameters, average number of neighbors and relaxation times to equilibrium. Simulations are performed on a torus without environmental factors in order to examine the behavior of these measures. The scaling arguments are shown to maintain the average number of neighbors. Another interesting

result is that the local relaxation time of the system is much shorter than the global relaxation time, $t_r \ll t_R$, and that the ratio \bar{n}_E/\bar{n}_U remains constant for a spectrum of simulations. The temporal resolution of the system is discussed, as well as its effect on the behavior of the system.

In order to capture the inner dynamics of capelin such as roe production and fat content, a Dynamic Energy Budget (DEB) model is developed for the Icelandic capelin. A new state variable is introduced to the DEB model to capture the roe production of individual fish. Species-specific coefficients are found for the capelin such as the shape coefficient and the Arrhenius temperature. Shown is how to link the DEB model to measurable quantities such as weight, length, fat, and roe content. Data on measured three year old female capelin from the 1999-2000 season from the Marine Research Institute of Iceland (MRI) and Matis, an Icelandic Food and Biotech R&D, is used. Plausible parameter values for the DEB model are found by fitting the output of the model to these data. Good fits are obtained between theory and observations, and the DEB model successfully reproduces weight, length, fat percentage and roe percentage of capelin. The effect of maturity on the spawning route of capelin is then emphasized; temperature preference and speed of individual fish are known to be affected by the state of maturity of the individual fish. Described is how the DEB model can be integrated with the interacting particle model, by letting the speed and preferred temperature range depend on the roe content of individuals.

Ágrip (in Icelandic)

Eindalíkani er lýst og því beitt á hinn íslenska loðnustofn (*Mallotus villosus*). Líkanið notast við tiltæk gögn um sjávarhitastig og nálgun á straumum og tekst þannig að framkalla hrygningargöngu loðnunnar fyrir þrjár mismunandi vertíðir. Sér í lagi spáði líkanið rétt fyrir um hrygningargöngu ársins 2008. Líkanið notast ekki við neina utanaðkomandi krafta til að stýra eindum að hrygningarslóðum. Framkvæmd var næmnigreining sem sýnir fram á að sjávarhitastig ásamt samspili samskipta milli einda og næmni þeirra gagnvart hitastigi eru þeir stikar sem ráði að mestu leyti leið hrygningargöngunnar. Í hermununum er fjöldi einda mun meiri en áður hefur tíðkast í sambærilegum líkönum. Hinn mikli fjöldi hefur áhrif á víðfeðma hegðun kerfisins og sökum samskipta milli einda berast upplýsingar um hitastig mun skilvirkar og hraðar. Við höldum því fram að til þess að viðhalda hegðun kerfisins milli hermana þurfi línulega skölun milli tímaskrefs og samskiptageisla. Sett er fram skölunin $N^{-1/2}$, þar sem N er fjöldi einda. Til þess að rannsaka hegðun kerfisins með tilliti til þessarar skölunar eru settar fram nokkrar kennistærðir og þær rannsakaðar. Kennistærðirnar eru meðal annars víðfeðmur og staðbundinn reglustiki, meðalfjöldi nágranna og tími sem tekur kerfið að ná jafnvægi. Hermanir eru gerðar á kleinuhring án umhverfisþátta til þess að rannsaka hegðan kerfisins með tilliti til kennistærðanna. Sýnt er fram á að skölun milli stika viðheldur meðalfjölda nágranna. Einnig er áhugavert að í öllum hermununum nær kerfið staðbundnu jafnvægi mun fyrir heldur

en það nær víðfeðmu jafnvægi, $t_r \ll t_R$. Einnig kemur í ljós að meðalfjöldi nágranna í jafnvægisástandi er hærri en búist er við og er hlutfallið \bar{n}_E/\bar{n}_U fast í hermununum. Við ræðum hlutverk tímaskrefs og áhrif þess á hegðun kerfisins.

Til þess að lýsa innri breytistærðum loðnu, eins og hrognafyllingu og fituhlutfalli, er líkan kvíks orkubúskaps (DEB) þróað fyrir íslensku loðnuna. Innleidd er ný breytistærð fyrir hrognamyndun einstakra fiska. Fundnir eru stíkar, sem eru háðir lífverunni, eins og stærðarstuðull og Arrheniusarhitastig. Sýnt er hvernig fá má út frá DEB líkninu mælanlegar stærðir eins og þyngd, lengd, fitu- og hrognahlutfall. Notast er við gögn frá þriggja ára gamalli kvenkyns loðnu frá 1999-2000 vertíðinni frá Hafrannsóknarstofnuninni og Matís. Fundnir eru trúverðug stikagildi með því að fella líkanið að mælingum. Gott samræmi fæst milli DEB líkansins og mælinga á þyngd, lengd, fitu- og hrognahlutfalli loðnunnar. Bent er á mikilvæg áhrif þroska á hrygningargönguna; þekkt er að kjörhitastig og hraði einstakra fiska taka mið af þroskastigi. Lýst er hvernig DEB líkanið verður tengt við hreyfilíkanið þannig að hraði og kjörhitastig einda muni ráðast af hrognahlutfalli einstaklingsins.

Acknowledgements

I have been quite fortunate, having two different but great advisors. I sincerely thank both of them for their encouragement and help throughout my academic career.

I dedicate this thesis to the memory of the late Dr. Kjartan G. Magnússon. I started working for Kjartan and Sven during my undergraduate years on a project which eventually proved to be the start of my research career. Having been given that opportunity meant a lot for a young student, and was both highly educational and great fun.

My parents have supported and encouraged me in whatever I have undertaken. They are responsible for most of my achievements. Mummi I thank for a life long friendship, all the fishing trips, and being someone I can always talk to.

Grace for being wonderful and my loving future wife. Thank you for cheering me on! I look forward to starting a life together with you.

I thank Benni for a great companionship (and technical support) through the years. Erling, Siggi and Sigrún I thank for being genuinely nice and fun people. I thank Dr. Alethea Barbaro and Dr. Brittany Erickson for great company and fun. The people in the Math Department in UCSB also made my stay in Santa Barbara enjoyable.

The following funding is greatly appreciated and made these studies possible: The project was funded during the years 2007-2009 by the Marine Research Institute of Iceland. The Research Fund of the Uni-

versity of Iceland funded the studies during 2009-2010. During the year 2010-2011 I was awarded a Nils-Abel grant to work in Madrid.

1

Introduction

1.1 Background

During the summer of 2004 I started working for Kjartan G. Magnússon, professor of mathematics, and Sven Þ. Sigurðsson, professor of computational science, programming an interacting particle model with applications to the Icelandic capelin stock [48]. This was my first taste of research, and gave me invaluable programming experience. Furthermore, it sparked my interest in such models, which have proved to be an endless source of fascination.

I have continued on this path of working with interacting particle models to describe the migratory behavior of the Icelandic capelin [3]. The model has been analyzed with scaling arguments on the interacting particle model.

At UC Santa Barbara, where I stayed during 2006-2009 with Björn Birnir, professor of mathematics, I participated in the Theoretical Ecology Seminars, where I learned about a Dynamic Energy Budget (DEB) model. The previous migration models all lacked the effect of maturation. I have to that end tailored the DEB model to the Icelandic capelin [18]

to capture e.g. the roe production and fat content of the capelin. I hope to continue along these lines, by combining the two models.

Working on such a diverse problem, spanning several disciplines, has allowed me to not only work with mathematicians, but also with biologists, chemical engineers, oceanographers, and even fishermen. Not only do I enjoy working with other people but I think that the outcome of collaboration is often greater than the sum of its parts.

1.2 Outline of thesis

This thesis is divided into two parts. Part I describes an interacting particle model (or Individual Based Model, IBM). We describe how it has been used to model the spawning migration of the Icelandic capelin [3]. In chapter 2 we describe in detail the mathematical model and equations of motion. An introduction to the model's background is also given, with references to various papers and other similar models. We discuss various aspects of the model, such as the link between the time step and reaction times to certain behavior. We also show how information of the environment, involving oceanic currents and temperature, is integrated into the model. In particular, we model the capelin's reaction to temperature with a temperature reaction function.

With the model described in Chapter 2 we reproduced the spawning migration of the Icelandic capelin for three different years in [3]. Chapter 3 describes the simulations and in detail the simulation of the 2007-2008 season. That simulation, described in Section 3.2.3, predicted the spawning migration route of the capelin, and serves as a reference simulation for the sensitivity analysis presented in [3]. We give in Section 3.3 the sensitivity analysis, which explores the simulations' sensitivity to certain parameters. An interesting result is that the sensitivity analysis elicits the temperature reaction and neighbor interactions to be the parameters

most significant in reproducing the migration paths. Chapter 4 describes and derives scaling arguments from [3]. We apply the scaling arguments to the parameters in the 2008 spawning migration, obtaining biologically plausible values.

In order to quantify the behavior of the system of particles, and investigate the scaling arguments, we confine the model to a torus as further explained in Section 4.2. Several measures are introduced and analyzed in Section 4.4, such as global and local order parameters, as well as each particle's number of neighbors. We note that the simulations reach an equilibrium state with respect to these measures, and we describe how to find relaxation times to the equilibrium state. Scenarios are simulated, and the resulting measures and relaxation times found. An interesting result is how quickly the system reaches a local consensus, compared to the global consensus.

Part II describes a Dynamic Energy Budget (DEB) theory. The model of Part I did not take into account the effect of maturity, which observation have shown to play an important role in the migration. In Chapter 5 we describe the DEB model and tailor it to the Icelandic capelin. We estimate several of the species-specific parameters of the model, and show results from [18]. We introduce a new variable to capture the roe production, since the DEB theory does not specifically treat the energy transfer to roe. In that chapter we finally propose how to infer measurable quantities such as weight, length, fat content and roe content from the variables of the DEB model. Comparison to data show good fits between the DEB theory and observations.

In Chapter 6 we describe how we integrate the DEB model with the interacting particle model described in Part I. The DEB model will determine several triggers for the behavior of individuals of the IBM and we propose how the speed and preferred temperature range of each individual depend on its roe content. We conclude the thesis in Chapter

7 with a broad discussion on the role of models for oceanic currents and temperature, their applications, and future research.

A general description of the life cycle of the Icelandic capelin is given below, in Section 1.3. Appendix A derives the equations used in the DEB model. Appendix B describes how von Bertalanffy growth equations can be obtained from the DEB model.

1.3 The Icelandic capelin

Capelin (*Mallotus villosus*) is a pelagic species which, like the herring (*Clupea harengus*), covers several hundred kilometers in its migration between feeding and spawning grounds [49,64,65,67]. We focus on the stock inhabiting the Iceland Sea, hereafter referred to as the Icelandic capelin. Its role in the ecosystem of the Icelandic waters is highly significant, bringing large amounts of biomass from the Arctic to more southerly latitudes.

A separate capelin stock resides in the Barents Sea, north of the coast of Norway and Russia. That stock has been widely studied and exhibits similar migration patterns between feeding and spawning grounds [23,24]. Much effort has been put into modeling this stock [19,31–33,46,57,58]. However, the Barents Sea migration route differs significantly from the Icelandic one, because it contains no islands or other obstacles.

Capelin is a vital part of the diet of fish species such as cod (*Gadus morhua*) [44,45]. Capelin catches are exported or processed into fishmeal and oils, and in recent years the Icelandic fishing industry has relied on its value. However, the size of the stock has been diminishing and much research effort has been put into stock estimation [26,65]. It is therefore of importance to be able to model the whereabouts of Icelandic capelin in order to control catches. A brief account will be given of pertinent details of this species here, but the interested reader is referred to [64],

where extensive details of the stock and its life cycle are provided.

Icelandic capelin spends the first 2-3 years of its life in waters north of Iceland, along the edge of the continental shelf. When it approaches maturity, usually either during the spring of its second or third year, it undertakes an extensive migration, herein referred to as the feeding migration, to the plankton-rich waters of the Iceland Sea as far north as the island of Jan Mayen. There, zooplankton is plentiful and it feeds on the vernal phytoplankton bloom in the region. The maturing capelin eat these zooplankton and grow extensively. In October and November, fully grown capelin return to the waters northwest and north of Iceland. In January, this portion of the stock undertakes a spawning migration clockwise around Iceland to the spawning grounds on the southern and western coasts. The spawning migration generally follows the continental shelf edge to the northeast and east of Iceland. However, in some years a portion of the capelin migrates against the coastal current and takes a westerly anti clockwise route to the spawning grounds. The capelin spawn in February/March and then die, leaving the eggs to hatch and the larvae to drift with the coastal currents to the continental shelf waters north of Iceland and to begin the cycle again. The migrations of capelin are seasonal and vary by year, so it is clear that the environment has a significant impact on the migration pattern [10, 64, 65].

Part I

Interacting particle models

2

Interacting particle model

2.1 Introduction

In this chapter we give an account of the interacting particle models used in subsequent chapters. We begin by describing the equations of motion without environmental effects in Section 2.3. The interaction between neighboring particles is discussed in Section 2.3.1. This model is the underlying interacting particle model which we later modify and extend. The scaling analysis in Chapter 4 applies to this model.

We then introduce the effect of the environment in Section 2.4 and describe how it is incorporated into the model, such as currents and temperature in Sections 2.4.1 and 2.4.2, respectively. With this extended model we model the spawning migrations of the Icelandic capelin. Simulations and sensitivity analysis are presented in Chapter 3. We refer to Section 1.3 and references therein for a description of the Icelandic capelin.

2.2 Model description

The model is a discrete off-lattice interacting particle model, and each particle represents an individual or a group of individuals. Particles look to their neighbors to determine their directional heading at each time step, averaging the neighbors' directional headings to determine their own. This allows the particles to move together as a group. The model introduced in [63], and further analyzed and developed in [13–15], is hereafter called the CV model. This type of model originated in physics and was adapted by the biological community to model group dynamics of social animals. It has been applied to herds of mammals, swarms of locusts, and schools of fish [8, 12, 13, 63]. A European project called STARFLAG (<http://angel.elte.hu/starling>) uses similar models for swarms of starlings, and explores various interdisciplinary connections. For a wonderful model in 3 dimensions, with many additional features to those discussed below, see [29].

Experiments have shown that fish interact differently with each neighbor depending on the distance to the neighbor; fish use their vision and their lateral lines, sense organs running down the sides of many species, to align themselves with neighbors and organize themselves into schools [52, 53]. Fish tend to both aggregate and avoid collisions when traveling, and the number of and distance to nearest neighbors seems to play a role in the organization of a school [25, 68, 69].

To simulate the internal dynamics of a group of interacting animals, many models incorporate different sensory regions into their simulations. The distance between two particles in such models determines how they react to each other and the strength of this interaction. These models include both individual and continuum (density) models, and the shape and the size of the sensory regions tend to differ depending on the model, see for example [11, 12, 16, 28, 40, 41, 60].

Partridge [52] pointed out that fish align their velocity to that of their neighbors. This feature was first introduced into the CV model in [30]. Birnir [7] analyzed the continuous time limit of this type of model and found several solutions and symmetries. In [6], solutions to both models presented in [7] were verified numerically. With sensory zones added, the discrete model exhibits rich behavior, and swarming solutions induced by noise were found. The latter work explored the interdependence of noise and the size and weights of the sensory zones in eliciting certain behavior from the model.

We follow [2] and [34] in employing three sensory zones around each particle to determine its reaction to the particles around it. Unlike many similar models [2, 12, 27, 28, 34, 40, 41, 68, 69], we do not employ a blind region behind the particle. It is ambiguous whether this blind region is biologically relevant in the case of fish, because the lateral line could allow a fish to sense the region behind it as it swims. In addition, the presence of such a region does not seem to affect the outcome of simulations [35].

2.3 Basic equations of motion

Let $\mathbf{q}_k(t) = (x_k(t), y_k(t))^T$ and $v_k(t)$ denote the planar position and speed of particle k at time t , respectively. The particles then update their speeds as the average of the speeds of neighboring particles within the zone of orientation, described in Section 2.3.1 below :

$$v_k(t + \Delta t) = \frac{1}{|O_k|} \sum_{j \in O_k} v_j(t), \quad (2.1)$$

and their positions

$$\mathbf{q}_k(t + \Delta t) = \mathbf{q}_k(t) + \Delta t v_k(t + \Delta t) \begin{pmatrix} \cos(\phi_k(t + \Delta t)) \\ \sin(\phi_k(t + \Delta t)) \end{pmatrix}, \quad (2.2)$$

where $\phi_k(t)$ is the directional angle of particle k . Below, we show how the directional angle of particle k is updated according to the position and directional angle of its neighbors, see Equations (2.8) and (2.7).

In Section 2.4.3 the directional angle will be determined by two factors, the reaction to neighboring particles, and reaction to the environment; see Equation (2.10).

We stress the fact that the above model is discrete in time. Ideally the time step Δt should reflect the time it takes the individual to react to its surroundings. That time constant we will denote τ . To appreciate this assume e.g. that we would replace Equation (2.1) with the following differential equation:

$$\frac{d}{dt}v_k(t) = \frac{1}{\tau} \left(\frac{1}{|O_k|} \sum_{j \in O_k} v_j(t) - v_k(t) \right). \quad (2.3)$$

The discretizing in time with time step Δt would result in

$$v_k(t + \Delta t) = v_k(t) + \frac{\Delta t}{\tau} \left(\frac{1}{|O_k|} \sum_{j \in O_k} v_j(t) - v_k(t) \right), \quad (2.4)$$

which reduces to Equation (2.1) if and only if $\Delta t = \tau$. If this is not the case it may be more appropriate to use Equation (2.4).

We discuss this issue further in Section 2.5, and it is central to our scaling analysis in Chapter 4.

2.3.1 Sensory zones

The sensory zones are three regions around each particle, defined as shown in Figure 2.1. The innermost region is the zone of repulsion, and a particle heads directly away from other particles in this region, so avoiding collisions. The outermost region is the annular zone of attraction; a particle heads directly towards other particles in this region,

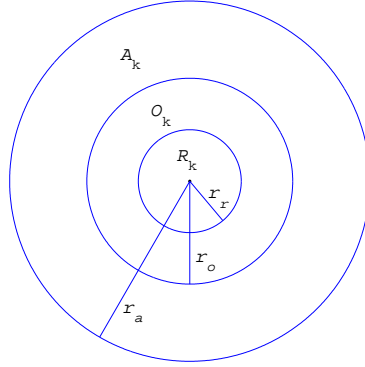


Figure 2.1: Zones of interaction (sensory zones) of particle k . A_k is its zone of attraction, O_k its zone of orientation, and R_k its zone of repulsion. These zones have radii r_a , r_o , and r_r , respectively.

adding to the cohesiveness of a group of particles. The annular region between the zones of repulsion and attraction is referred to as the zone of orientation, and a particle attempts to align itself in speed and in direction with particles within this zone. These directional headings often conflict, so each particle takes a weighted average of these directions, see Equation (2.7).

We denote the set of indices of the particles within particle k 's zone of repulsion at time t by $R_k(t)$, its zone of orientation by $O_k(t)$, and its zone of attraction by $A_k(t)$. In order to simplify notation we omit the dependence on time below. At all times $k \in O_k$, ensuring that particle k 's directional heading is taken into account. Now, introduce

$$I_k(t) := R_k(t) \cup O_k(t) \cup A_k(t) \quad (2.5)$$

as the set of indices of all the particles within particle k 's zones of in-

teraction, including itself because $k \in O_k$. The set I_k thus contains the indices of all the particles by which particle k determines its directional heading. We denote the number of particles within each zone by $|\cdot|$. Note that at each time step we have

$$|I_k| = |R_k| + |O_k| + |A_k| \quad (2.6)$$

since all the sets on the right hand side are disjoint. Finally, $|I_k| \geq 1$ because $k \in O_k$.

2.3.2 Directional heading determined by neighbors

At each time step, we calculate how a particle reacts to neighboring particles within its zones of interaction as a directional heading, \mathbf{d}_k . To avoid conflicts with neighboring particles, a weighted average is taken:

$$\begin{aligned} \mathbf{d}_k(t + \Delta t) := & \frac{1}{|I_k|} \times \left(\sum_{r \in R_k} \frac{\mathbf{q}_k(t) - \mathbf{q}_r(t)}{\|\mathbf{q}_k(t) - \mathbf{q}_r(t)\|} \right. \\ & \left. + \sum_{o \in O_k} \begin{pmatrix} \cos(\phi_o(t)) \\ \sin(\phi_o(t)) \end{pmatrix} + \sum_{a \in A_k} \frac{\mathbf{q}_a(t) - \mathbf{q}_k(t)}{\|\mathbf{q}_a(t) - \mathbf{q}_k(t)\|} \right). \end{aligned} \quad (2.7)$$

In the expression above, we sum up unit vectors according to the interaction rules described in Section 2.3.1.

We thus calculate the directional angle, ϕ_k , of Equation (2.2) as the direction of the vector \mathbf{d}_k :

$$\begin{pmatrix} \cos(\phi_k(t + \Delta t)) \\ \sin(\phi_k(t + \Delta t)) \end{pmatrix} = \frac{\mathbf{d}_k(t + \Delta t)}{\|\mathbf{d}_k(t + \Delta t)\|}. \quad (2.8)$$

This is the directional angle used for the basic interacting particle model of Equation (2.2). As mentioned before, the scaling analysis of Chapter 4 analyzes this model on a torus.

In the next section we include environmental factors to the model. In Section 2.4.3 we show how we include particles' reaction to temperature, and subsequently how the directional angle is modified, see Equations (2.9) and (2.10).

2.4 The environment

To model the migration route accurately, we include environmental data in the simulations to allow particles to respond to their environment. To this end, we introduce an environmental grid containing information about the current and the oceanic temperature at a depth of 50 m. The grid also has information about landmasses, encoded as points on the grid with extreme heat, thus indirectly forcing the particles to move away from landmasses. We describe in more detail in Section 2.4.4 how this is handled. The data contained in the grid allow each particle to be translated by the current and to adjust its direction depending on the temperature of the surrounding ocean.

Previous models of the migratory behavior of capelin use some sort of attraction towards the feeding or spawning grounds [30, 46–48, 58]. Promising results for the Barents Sea stock were presented by [32] using only environmental factors, but with some discrepancies between predictions and observations. Here, we use an interacting particle model based on the work of [3, 30, 48]. A notable difference between our model and previous models of capelin migration is the absence of an artificial attracting forcing term.

2.4.1 Currents

The speed of a migrating capelin has been recorded to reach $>25 \text{ km d}^{-1}$ [64]. The clockwise coastal current around Iceland is quite strong and its

speed can be of the same order of magnitude as the speed of fish relative to the surrounding sea. Although the current changes seasonally and even varies from day to day based on weather conditions, for simplicity we took it to be constant in [3]. We show a map of these currents in Figure 3.2. Its maximum translation is about 15 km d^{-1} .

We assume that fish do not change directional heading dependent on the current, so it translates them independent of their own movement. This assumption is reasonable and in fact integral to the physicality of the model, because in some years a portion of the capelin stock migrates counter-clockwise around Iceland, against the current. The currents used in [3] is the same approximated oceanic current field as [47], and can be seen in Figure 3.2. Hereafter, the current field is denoted \mathbf{C} . In Section 6.3 we describe a new model on currents and temperature around Iceland by Dr. Kai Logemann [43], which we intend to use for future simulations.

2.4.2 Temperature

It is well known that capelin are sensitive to oceanic temperatures, both during their feeding migration and during their spawning migration [64, 65]. Capelin have a relatively narrow temperature preference, and prefer temperatures from about 3°C up to 10°C , although they are known to enter much colder waters [64]. We therefore model this behavior in the following way.

The particles sense the surrounding temperature, T , according to the gradient of the function r :

$$r(T) := \begin{cases} -(T - T_1)^4 & \text{if } T \leq T_1, \\ 0 & \text{if } T_1 \leq T \leq T_2, \\ -(T - T_2)^2 & \text{if } T_2 \leq T \end{cases} \quad (2.9)$$

where T_1, T_2 are constants, and $[T_1, T_2]$ is referred to as the preferred

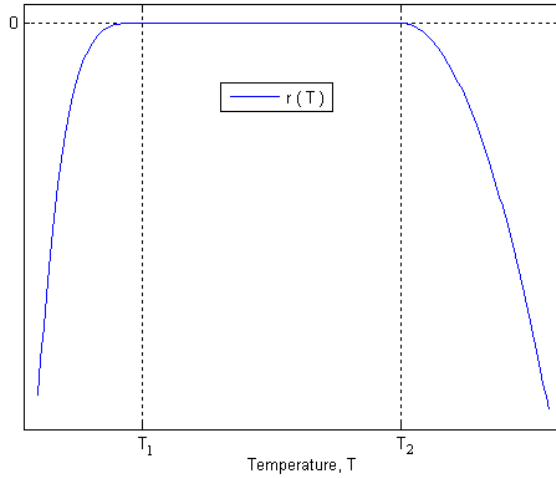


Figure 2.2: Graph of the temperature response function r from Equation (2.9)

temperature range. Figure 2.2 shows the graph of r . This is the same function previously used in [46–48].

By looking at the gradient of r , we see that fish should move towards areas within the preferred temperature range, the tendency being stronger in colder water. However, the last tendency does not often come into effect in practise, since only the direction of the gradient of the function r is used.

2.4.3 The directional angle with environmental influence

Now, we have the directional heading according to neighbor interactions, Equation (2.7), and the particles' reaction to temperature via ∇r , see Equation (2.9). These two factors need to be weighed together in \mathbf{D}_k ,

where

$$\mathbf{D}_k(t + \Delta t) := (1 - \beta) \frac{\mathbf{d}_k(t + \Delta t)}{\|\mathbf{d}_k(t + \Delta t)\|} + \beta \frac{\nabla r(T(\mathbf{q}_k(t)))}{\|\nabla r(T(\mathbf{q}_k(t)))\|}. \quad (2.10)$$

The factor β we refer to as the temperature weight factor. We note that the model's behavior is highly dependent on β [3], which we detail in the next chapter. In the discussion below we discuss details about the above equation and the complexities of β .

Alternatively, we can rewrite Equation (2.10) as

$$\mathbf{D}_k(t + \Delta t) = \frac{\mathbf{d}_k(t + \Delta t)}{\|\mathbf{d}_k(t + \Delta t)\|} + \beta \left(\frac{\nabla r(T(\mathbf{q}_k(t)))}{\|\nabla r(T(\mathbf{q}_k(t)))\|} - \frac{\mathbf{d}_k(t + \Delta t)}{\|\mathbf{d}_k(t + \Delta t)\|} \right). \quad (2.11)$$

The second term of the right hand side of Equation (2.11) is proportional to β and the difference between the direction of temperature preference and the direction determined by neighbor interactions. We see that β determines how much a particle adjusts to its temperature preference at each time step. This, in turn, affects how information of the environment propagates through a school of particles.

We thus calculate the directional angle ϕ_k , with reaction to environment included, as the angle of the vector \mathbf{D}_k . We now have everything to describe the full model, as Equation (2.12) below.

2.4.4 Equations of motion with the environment

We now modify the Equation of motion (2.2) to include the environmental fields as following:

$$\mathbf{q}_k(t + \Delta t) = \mathbf{q}_k(t) + \Delta t v_k(t + \Delta t) \frac{\mathbf{D}_k(t + \Delta t)}{\|\mathbf{D}_k(t + \Delta t)\|} + \Delta t \mathbf{C}(\mathbf{q}_k(t)). \quad (2.12)$$

Equation (2.12) is the model of motion with environmental factors

included, which we use to model the spawning migration of the capelin [3]¹. In the next chapter we describe the simulation from the 2007-2008 season. In Section 3.3 we discuss how the temperature and currents affect the model and present a sensitivity analysis to investigate the model's dependence to the parameters described above.

We note that in order to ensure that particles do not swim onto land, we go through the following process if a particle gets close to land, i.e. senses a point of extreme temperature. We calculate Equation (2.10) and determine its next location according to Equation (2.12). If that location is still close to land we temporarily increase the particle's sensitivity to temperature. We then recalculate Equation (2.12) and go through the same process until the particle only responds to the temperature, i.e. as if β has the value 1. By doing so, we effectively reflected particles from land with a minimal angle needed to avoid swimming onto dry land.

2.5 Discussion

It is plausible to assume that there is a difference between the time it takes an individual fish to react to temperature and the time it takes it to react to its neighbors. The factor β , to which we refer as the temperature weight factor, reflects the relation between the time constant of the reaction to its neighbors, τ_N and the time constant of the reaction to temperature, τ_T .

To appreciate this assume, similarly to Equation (2.3), that we have the following differential equation governing the change in the [unit] di-

¹Equation (6) in [3] does not multiply the currents with the time step, which is simply a typographical error.

rection:

$$\frac{d}{dt} \tilde{\mathbf{D}}_k(t) = \frac{1}{\tau_N} \left(\mathbf{D}_{k,N}(t) - \tilde{\mathbf{D}}_k(t) \right) + \frac{1}{\tau_T} \left(\mathbf{D}_{k,T}(t) - \tilde{\mathbf{D}}_k(t) \right), \quad (2.13)$$

where $\mathbf{D}_{k,N}(t)$ denotes the directional heading according to neighbor interactions,

$$\mathbf{D}_{k,N}(t) := \frac{\mathbf{d}_k(t + \Delta t)}{\|\mathbf{d}_k(t + \Delta t)\|}, \quad (2.14)$$

and $\mathbf{D}_{k,T}(t)$ denotes the directional heading according to the reaction to temperature,

$$\mathbf{D}_{k,T}(t) := \frac{\nabla r(T(\mathbf{q}_k(t)))}{\|\nabla r(T(\mathbf{q}_k(t)))\|}. \quad (2.15)$$

Discretizing Equation (2.13) with time step Δt results in

$$\tilde{\mathbf{D}}_k(t + \Delta t) = \tilde{\mathbf{D}}_k(t) + \frac{\Delta t}{\tau_N} \left(\mathbf{D}_{k,N}(t) - \tilde{\mathbf{D}}_k(t) \right) + \frac{\Delta t}{\tau_T} \left(\mathbf{D}_{k,T}(t) - \tilde{\mathbf{D}}_k(t) \right), \quad (2.16)$$

which reduces to Equation (2.10) by choosing $\Delta t = \tau_N \tau_T / (\tau_N + \tau_T)$ and subsequently obtaining

$$\beta = \frac{\tau_N}{\tau_N + \tau_T}. \quad (2.17)$$

We note that with β as in Equation (2.17) and $\tau_T = \sigma \tau_N$ we obtain

$$\beta = \frac{1}{1 + \sigma}, \quad (2.18)$$

which results in $\beta \in [0, 1]$.

On the other hand, if we choose the time step to correspond to the reaction time to neighbors, $\Delta t = \tau_N$, then we get

$$\tilde{\mathbf{D}}_k(t + \Delta t) = \mathbf{D}_{k,N}(t) + \frac{\tau_N}{\tau_T} \left(\mathbf{D}_{k,T}(t) - \tilde{\mathbf{D}}_k(t) \right), \quad (2.19)$$

which is again similar to Equation (2.11) with

$$\beta = \frac{\tau_N}{\tau_T}, \quad (2.20)$$

and with $\tau_T = \sigma\tau_N$ as before we obtain

$$\beta = \frac{1}{\sigma}, \quad (2.21)$$

which results in $\beta \in [0, 1]$, assuming that $\sigma > 1$.

Finally, we note that neighbor interactions are due to both vision and sensing through the lateral line of the fish. It is biologically plausible that visual and lateral line sensing is information a fish processes fairly quickly, and much quicker than information about the temperature is processed. In addition, changes to the order of neighboring fish happen faster than changes to the temperature, which on small scales is close to being constant. Thus the reaction time to temperature, τ_T , is much longer than the reaction time to neighbors, τ_N , resulting in $\sigma \gg 1$ and hence $\beta \ll 1$ in either Equation (2.18) or Equation (2.21). In the next Chapter, Section 3.2, we indeed simulate the model of Section 2.4.4 with β small.

However, the time constants τ_N and τ_T are data which is hard to measure and not available for capelin, and so the choice of the correct form of β has to be based on simulations.

3

Case studies and sensitivity analysis

3.1 Introduction

In [3] we presented simulations of the spawning migrations of the Icelandic capelin from three different seasons; 1984-1985, 1990-1991, and 2007-2008. With parameter values given in Equation (3.1) and discussed in Section 3.2.2, we reproduced the spawning migration route of the capelin for each season. In particular, the simulations recreated characteristics of the migration route particular to each of the three seasons, closely matching acoustic data from [64].

Below, in Section 3.2.3, we describe the simulation of the 2007-2008 spawning migration in detail, but refer to [3] for further information, figures, and details on the other two case studies. The simulation of the 2007-2008 spawning migration is of interest and included here for two reasons. Firstly, it successfully predicted the migration route of the capelin that year. Secondly, it serves as the reference simulation to which we compare the scenarios of the sensitivity analysis in Section 3.3.

In the sensitivity analysis of Section 3.3 we show the temperature reaction and neighbor interactions to be the parameters most significant in reproducing the migration paths [3].

3.2 Simulations of spawning migrations

3.2.1 Temperature and currents for the 2008 simulation

In the 2007-2008 case study, we used temperature data extracted from a German weather website (<http://www.wetterzentrale.de/topkarten/...fsfaxsem.html>) on February 5 of 2008. These data were then extrapolated to our grid using Ocean Data View. The nature of these data is different from temperature data from the MRI, which had not been collected at that time; the website averages data from various surface measurements from buoys, satellites, and ships. If data are missing or beyond a certain distance from available measurements, the website uses the average temperature of the current month from 1961 to 1990. It is reasonable to assume that these surface data approximate the temperature at a depth of 50 m because, in winter, strong winds and storms cause turbulent mixing of the water near the surface down to a few dozen meters, as temperature data corroborate. Hence, the temperature data is comparable among the three case studies in [3]. Contour plots of the extrapolated temperatures are shown in Figure 3.1.

In all three case studies in [3] we used the map of the currents shown in Figure 3.2. Its maximum translation is about 15 km d^{-1} . This is the same approximated oceanic current field as used in [47]. These currents come into play as the currents field \mathbf{C} in Equation (2.12).

As mentioned before, for simplicity we took the currents field to be constant although the current changes seasonally and even varies from

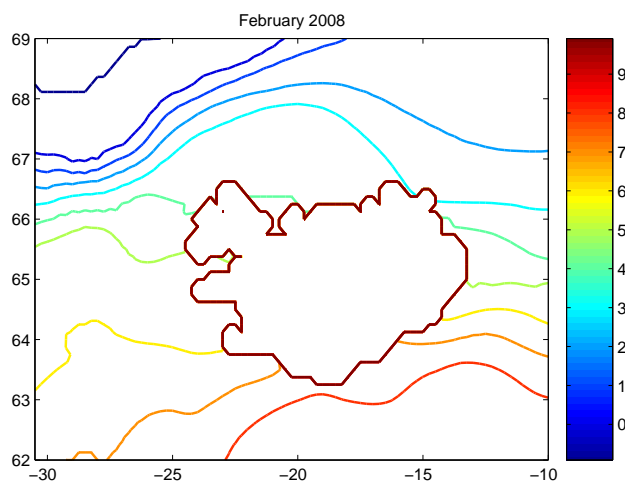


Figure 3.1: Contour lines of extrapolated surface temperature data used in the simulations of the 2008 spawning migration. From February of 2008

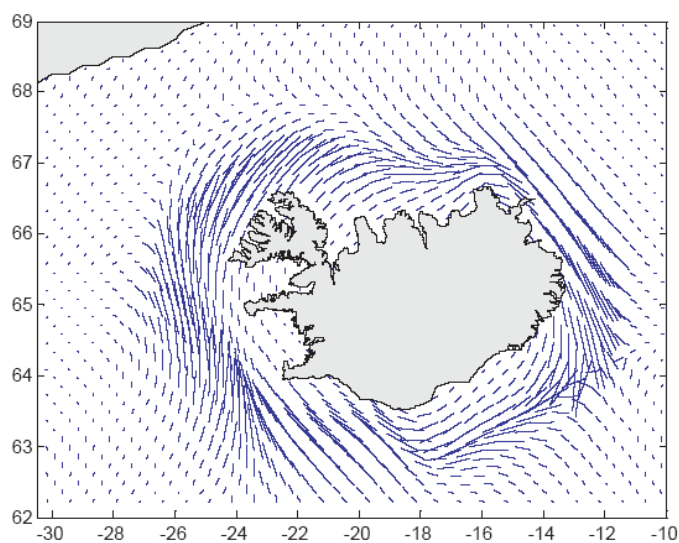


Figure 3.2: Simulated ocean current field around Iceland [47]. The strength of the current is given by the length of the line segments. The stronger coastal current runs clockwise around Iceland.

day to day based on weather conditions. We show in Section 6.3, once the new currents of the CODE model have been included, how such changes will be handled.

3.2.2 Parameter and simulation specifications

In the simulations of the spawning migrations, we use a general xy -coordinate system of dimensions 82 by 56. The temperature and oceanic currents are stored in a grid defined at points $(i, j) \in \mathcal{Z}^2 \cap ([0, 82] \times [0, 56])$, corresponding to the area from 30.5–10.0°W to 62.0–69.0°N. Hence, the spacing between points on the environmental grid is 0.25° in longitude and 0.125° in latitude. This means that the grid has a spatial resolution of roughly 12 km in each direction, although the longitudinal length varies slightly depending on the latitude. This discrepancy is not significant for our simulations, so is not taken into account here.

We initially placed particles in areas where data indicated a high density of mature capelin [64]. For the simulation of the 2008 spawning migration, the initial distribution of particles is shown in Figure 3.4(a), as reported by the MRI. The simulation runs from early January to early April. The general route of the simulation can be seen in Figure 3.4 and is discussed in more detail below in Section 3.2.3.

We held the number of particles per “main school” to be between 40 000 and 50 000 in each simulation, with a uniform density in each school across the simulations. This ensures that the dynamics of the migration are similar across years, although the total number of particles differs between simulations. According to the scaling arguments presented in Section 4.3, by keeping the particle density constant in areas containing fish, we avoid the need to change parameter values between simulations.

Icelandic capelin generally spawn in water between 3 and 10°C [64].

In the simulations, we set the temperature preferences to be between 3 and 6.5°C. Interaction among particles and the relatively high interaction weight enables particles to enter water that is outside their preferred range. We set the temperature weight factor $\beta = 0.010$ [Equation (2.10)], but because of the form of the temperature preference function (2.9), the particles tend to leave water that is outside their preferred range. This preference function combined with the fact that all the particles are reacting to the same temperature map keeps them in water of a temperature close to the actual preferred range of the capelin.

We measure time t in days and speed v_k in grid units (about 12 km) per day, and the radii of a particle's sensory zones in grid units. We set $\Delta t = 0.050$ (i.e. 1.2 h); speeds v_k were initialized uniformly in $[0, 0.375]$ (i.e. $[0, 4.5]$ km d⁻¹), then updated according to Equation (2.1). Initial direction angles are assigned randomly. Once the particles are east of 13.5°W, the algorithm sets $v_k = 1.25$, or about 15 km d⁻¹, which is significantly faster than the initial speeds and crudely models the observed increase in speed. We discuss the interplay between the spatial resolution of the grid and the time step in the Discussion below. In Section 6.1 we describe how this increase in speed will depend on the roe content of each individual particle, once changes in roe content have been incorporated into the model.

The other parameter values were $r_r = 0.010$ and $r_o = 0.100$, which correspond roughly to $r_r \simeq 120$ m and $r_o \simeq 1.2$ km. We found that including the zone of attraction causes the particles to cluster unnaturally and fails to reproduce the large schools observed by researchers. The zone of attraction was therefore excluded here from the simulations by setting $r_a = r_o$.

In the simulations of the three spawning migrations in [3] the param-

eter values are therefore

$$\begin{aligned}
 \Delta t &= 0.050 \\
 (r_r, r_o, r_a) &= (0.010, 0.100, 0.100), \\
 [T_1; T_2] &= [3.0; 6.5]^\circ\text{C}, \\
 \beta &= 0.010.
 \end{aligned}
 \tag{3.1}$$

In Section 3.2 we briefly describe these simulations, but for details, discussion and figures, we refer to [3]. However, below we present the sensitivity analysis from that paper. In the simulations of the three spawning migrations, the value of β was set to 0.010.

We let Δq denote the distance a particle travels in one time step. We note that with these parameter values the average initial spatial resolution Δq is similar to the radius of repulsion, r_r , allowing faster moving particles to fall close to each other. We discuss this issue further in Section 3.4.

Finally, the code used is written in C++, and the run time with around 50 000 particles was on average 3-5 h. All simulations were done on a dual-core Intel Pentium 4 (2.60 GHz per core, 512 L2 cache, 1GB main memory). In [70], the run time of the code is shown to be $O(N^{1.8})$, when run in parallel. For further details about the implementation, and how the simulations can be run in parallel, see [70].

3.2.3 The 2008 case study

An important result of [3] is the successful prediction of the route of the 2007-2008 spawning migration using only initial fish density and temperature measurements taken by research and fishing vessels during January 2008. Capelin proved to be difficult to find and a very low fishing quota was set. Subsequently, the fisheries were closed in late February as a result of poor and low estimates of stock size. Eventually, a large quan-

tivity of capelin was found to have taken an unusual route, resulting in an additional fishing quota being set at the beginning of March 2008.

We ran the 2007-2008 simulation for 1900 time steps (95 d) between early January and early April. Figure 3.3 shows the simulated migration's initial placement and simulations of days 47, 59, and 65, roughly mid-February, late February, and early March. Figure 3.4a shows acoustic measurements from 26 and 27 February, and Figure 3.4b shows observations gathered between 29 February and 3 March. Comparing Figure 3.3c with Figure 3.4a reveals that the bulk of the particles in the simulation headed towards the shore almost exactly where the research vessels later found them to be. Furthermore, Figure 3.3d shows a school of particles east of Iceland in almost precisely the same location as the school of fish farthest to the right in Figure 3.4b. This indicates that the route and proportions of the particles in the simulated spawning migration were remarkably accurate, especially because the simulation was completed in early February 2008, before fishing was closed.

3.3 Sensitivity analysis

We now look more closely at the behavior of the model when parameters are varied. We choose the run from the 2007-2008 simulation, see Section 3.2.3, as a reference case to which we compare the other simulations. This choice of parameters successfully predicted the unusual spawning migration of that year, in addition to producing good results for the two other years [3].

We explore the model's sensitivity to three different sets of parameters. First, we change the preferred temperature range, $[T_1, T_2]$, which clearly affects the migration pattern because particles seek into waters with temperature within this range. Second, we vary the parameter β , which determines how strongly and quickly particles sense temperature,

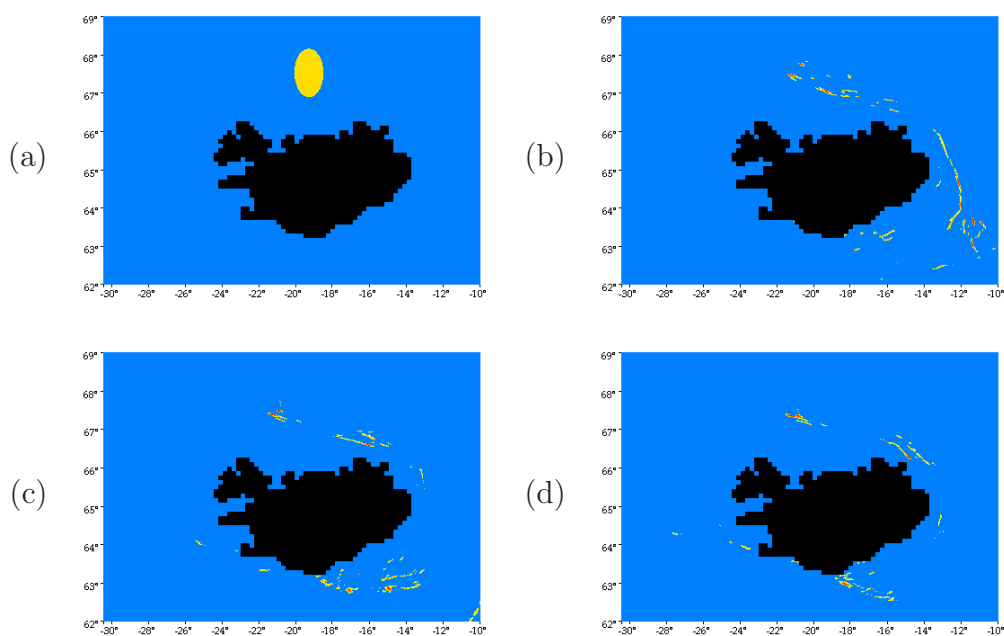


Figure 3.3: Simulation of the 2007-2008 spawning migration [3]. (a) early January, day 0, (b) mid-February, day 47, (c) late February, day 59, (d) early March, day 65. Compare to Figure 3.4 and see Section 3.2.3 for details.

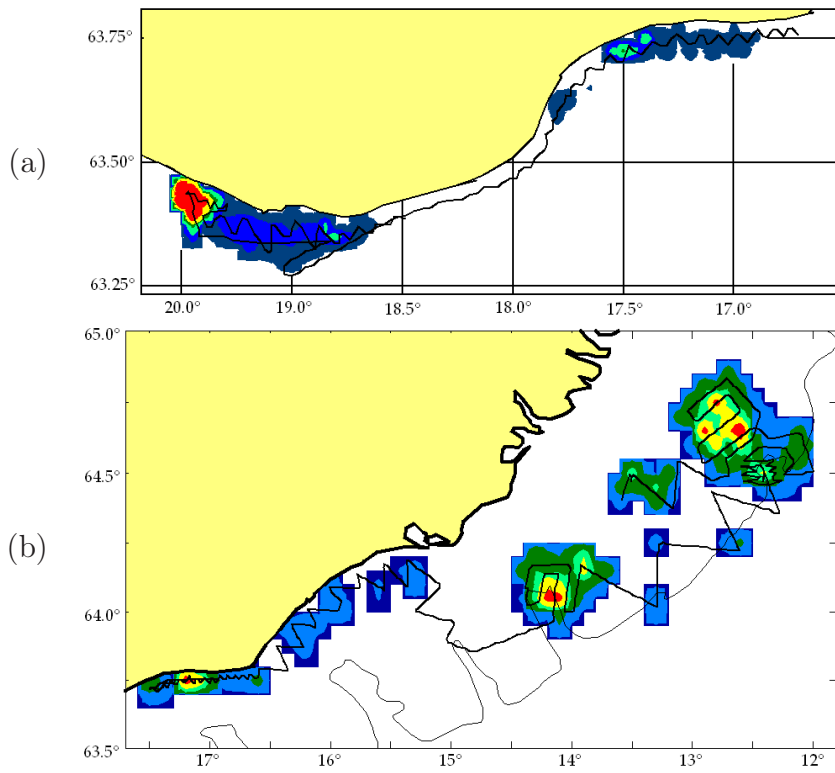


Figure 3.4: (a) Measured distribution of capelin near the south coast of Iceland from 26 to 27 February 2008. (b) Measured distribution of capelin near the southeast coast of Iceland from 29 February to 3 March 2008.



Figure 3.5: Compartments used for the sensitivity analysis. See section on the sensitivity analysis and Tables 3.1, 3.2, and 3.3.

and is an interesting parameter for the simulations. Finally, we vary the radii, r_r , r_o , and r_a , which affect the interacting behavior of the particles. These scenarios are described in Section 3.3.1.

In order to quantify the outcome of the sensitivity analysis, the area of the simulation is divided into 21 numbered compartments, as shown in Figure 3.5. In each new simulation, only one parameter value is changed in order to understand its role in the model. The new values for each parameter are presented in Table 3.1, giving rise to nine scenarios.

In none of the scenarios do we change the time step, and thus the ratio between the time step and the reaction time of the particle to its neighbors, τ_N , remains constant. This is especially important for the scenarios where we change the value of β . The reason is that β depends in some way on the ratio between the reaction times to neighbors and temperature, as discussed in Section 2.5, and thus on how strongly the particle reacts to temperature.

The number of particles in all runs was approximately 41 800. At days

47 and 65, the numbers of particles in each compartment were counted, then divided by the initial number of particles in these simulations to obtain the distribution as percentages. This was done for Scenarios (a)-(i) (Table 3.1) as well as the 2007-2008 reference case on days 47 and 65 (Tables 3.2 and 3.3). Note that the percentage values of the reference simulation do not add to 100% nor do the differences in the remaining simulations add to 0%. The reason is that particles crossing the boundary of the model region are lost. The percentage of lost particles in the reference case on days 47 and 64 was 8.9% and 20.3%, respectively.

3.3.1 Scenarios

In Scenario (a), only the upper bound of the preferred temperature range was increased. The runs therefore look similar until the particles reached the upper limit of the preferred temperature range in the east of Iceland. On day 47, the difference in compartments 13, 14, and 21 was the result of the particles not having reached this upper limit. They therefore stayed closer to shore and were in turn translated by the current to the south. The distribution on day 65 was, however, similar to the reference case. In Scenario (b), the lower bound of the temperature range was lowered and the particles lingered in the north (see compartments 5 and 6 on day 47). The reason for this is that the cold front in the north did not push the particles down into the stronger currents. The current then slowly moved the particles to the east, and on day 65 most of the particles were located in compartment 14. We note that the particles did not reach the spawning grounds, as compartments 17-19 showed.

In Scenarios (c)-(f), the value of β was changed. This parameter determines how strongly the particles sense their temperature environment compared with the strength of interaction. The time step remained unchanged in all scenarios. By changing β and not the time step, we con-

sistently change how quickly particles adjust their directions according to the temperature. In Scenarios (c) and (d), the value of β was lowered, so the effect of the current was the main environmental factor in the particles' movement. They therefore did not sense the temperature as strongly, causing them to swarm to the north.

In extreme Scenario (c), where the value of β was one-fifth of the reference value, the particles traveled slowly to the northern and the eastern boundary, and close to 65% of the particles were lost. In Scenario (d), lack of an aggregate direction caused a more northerly distribution than in the reference case, on days 47 and 65. For both (c) and (d), the particles did not arrive at the spawning grounds. In (c), a small proportion of the particles traveled south, but did not come close to land because the effect of temperature was not strong enough to drive them to shore. The particles passed by the spawning grounds and finished in compartments 9 and 16, far off the coast of Iceland.

Scenarios (e) and (f) had a higher value of β than in the reference simulation, so the particles sensed their environment more strongly. Interestingly, even in (e) with β 50% higher than in the reference case, the particles did not arrive at the spawning grounds. When they reached the 6.5°C isotherm, they were diverted to the west. Most of the particles then came to shore in southeast Iceland, because they were not able to enter water that was too warm. Close to 58% of the particles finished in compartments 12, 13, 19, and 20.

In Scenario (f), the high value of β resulted in an interesting behavior when the particles reached the 6.5°C isotherm. The strong current translated the particles into warm water, to which they reacted strongly. Unable to enter the warm water, the particles were reflected to the east and continued off the boundary. About 72% of the particles were lost to the east in this way.

Finally, Scenarios (g)-(i) explored the behavior of the system as the

ratio of the radii changed. In Scenario (g), the radius of repulsion, r_r , was half the value used in the reference case and in (h) it was twice the value. In Scenario (g), the particles formed smaller schools, because the small value of the radius of repulsion did not force them to spread out. Some particles reached the spawning grounds via a similar route to the reference case, but more quickly (see compartments 16-18 in Table 3.3). In Scenario (h), the particles also reached the spawning grounds similarly to the reference case. The main difference in distribution can be explained by the fact that many fewer particles were lost: in the reference case more than 20% were lost on day 65, but less than 8% in Scenario (h). The schools were also more spread out, as expected from a larger value of the radius of repulsion. Finally, Scenario (i) includes a non-trivial zone of attraction. In this case the particles clumped unnaturally and moved in small clusters. This led to less cohesion among the particles as a whole, which is uncharacteristic of the migration patterns [64].

3.4 Discussion

Our work in [3] indicates that it is possible to explain the migration route of the Icelandic capelin stock without a homing instinct, and that oceanic temperature is of great importance to the path of the migration. With tens of thousands of particles, information about the environment propagates through the simulated schools much more effectively than in previous models, which makes the system more able to sense the environment. This improvement could account for not needing attraction potentials to reproduce the migration.

The success of such a biologically simplistic model demonstrates the profound effects that temperature and local interaction among the fish have on the migration route. Using a preferred temperature range and an adjustable strength of the interactions between particles suffices to re-

Table 3.1: Parameter values used in the scenarios of the sensitivity analysis.

Parameters varied:	Lost on day 47 [%]	Lost on day 65 [%]
(a) $T_2 = 7.5^\circ C$	10.7	14.7
(b) $T_1 = 2.0^\circ C$	18.4	22.7
(c) $\beta = 0.002$	38.3	64.9
(d) $\beta = 0.005$	9.3	23.4
(e) $\beta = 0.015$	9.0	11.1
(f) $\beta = 0.050$	12.3	72.4
(g) $r_r = 0.005$	14.5	29.8
(h) $r_r = 0.020$	4.6	7.6
(i) $r_a = 0.200$	8.8	10.0

Parameter values used in the reference case of 2007-2008:

$[T_1; T_2] = [3.0; 6.5]^\circ C$, $\beta = 0.010$, $(r_r, r_o, r_a) = (0.010, 0.100, 0.100)$.

Table 3.2: The entries in the first block show the distribution into the compartments shown in Figure 3.5 on day 47 in the reference case of the 2007-2008 simulation, which is described in Section 3.2.3. For a description of Scenarios (a)-(i) see Table 3.1, and the difference between the scenarios and the reference simulation of 2007-2008 is shown. The entries in (a)-(i) correspond to the 21 compartments shown in Figure 3.5, and are arranged in the same order. And a negative entry signifies more particles being in the reference simulation of 2007-2008.

	Distribution into compartments:						
Reference	0.0	0.0	0.0	13.2	3.2	0.0	0.0
	0.0	0.0	0.0	0.0	1.2	22.0	13.0
	0.0	0.0	0.0	0.6	7.4	8.0	22.5
Scenarios:	Difference of distribution into compartments:						
(a)	0.0	0.0	1.9	0.6	1.2	0.0	0.0
	0.0	0.0	0.0	0.0	4.6	14.9	-9.2
	0.0	0.0	0.0	0.7	-1.8	1.7	-16.5
(b)	0.0	0.0	6.4	-1.5	14.3	19.3	0.3
	0.0	0.0	0.0	0.0	-1.2	-9.2	-12.2
	0.0	0.0	0.0	3.8	-2.4	-4.8	-22.5
(c)	0.0	0.0	4.6	-4.8	-0.1	8.3	0.0
	0.0	0.0	0.0	0.0	-1.2	-11.0	-3.5
	0.0	0.0	0.0	-0.6	-7.2	0.1	-14.1
(d)	0.0	0.0	0.0	9.5	7.2	2.5	0.0
	0.0	0.0	0.0	0.0	-1.2	3.1	-11.1
	0.0	0.0	0.0	1.5	4.4	-6.9	-9.5
(e)	0.0	0.0	0.0	-8.6	3.1	1.2	0.0
	0.0	0.0	0.0	0.0	3.1	4.8	-10.4
	0.0	0.0	0.0	-0.6	-0.1	15.3	-8.0
(f)	0.0	0.0	0.0	-6.1	3.9	0.3	0.0
	0.0	0.0	0.0	0.0	-1.2	-10.2	37.5
	0.0	0.0	0.0	-0.6	-7.4	-2.7	-17.1
(g)	0.0	0.0	0.0	-1.3	-2.7	0.0	0.0
	0.0	0.0	0.0	0.0	1.0	-2.1	-5.3
	0.0	0.0	0.0	3.1	-1.5	6.1	-3.1
(h)	0.0	0.0	0.0	-11.2	-2.9	0.0	0.0
	0.0	0.0	0.0	0.0	2.5	-0.3	-10.5
	0.0	0.0	0.0	2.9	6.4	8.6	8.8
(i)	0.0	0.0	0.0	-6.1	6.5	0.1	0.0
	0.0	0.0	0.0	0.0	-1.2	7.9	-3.2
	0.0	0.0	0.0	-0.1	2.9	15.7	-22.5

Table 3.3: The entries in the first block show the distribution into the compartments shown in Figure 3.5 on day 65 in the reference case of the 2007-2008 simulation, which is described in Section 3.2.3. The Scenarios (a)-(i) are described in Table 3.1, and the difference between the scenarios and the reference simulation of 2007-2008 is shown. The entries in (a)-(i) correspond to the 21 compartments shown in Figure 3.5, and are arranged in the same order. And a negative entry signifies more particles being in the reference simulation of 2007-2008.

	Distribution into compartments:						
Reference	0.0	0.0	0.0	7.3	6.0	0.0	0.0
	0.0	0.5	0.0	0.0	0.0	18.9	0.0
	0.0	0.4	11.1	19.6	7.6	1.7	6.7
Scenarios:	Difference of distribution into compartments:						
(a)	0.0	0.0	2.6	-0.1	-0.9	0.0	0.0
	0.0	-0.5	0.0	0.0	0.0	9.1	0.0
	0.0	-0.4	3.1	-2.8	-0.1	2.3	-6.7
(b)	0.0	0.0	2.8	6.1	-4.7	0.5	0.0
	0.0	4.0	0.0	0.0	0.9	1.0	25.9
	0.0	-0.4	-3.4	-19.6	-7.1	-1.7	-6.7
(c)	0.0	0.7	3.8	-1.7	-5.4	4.3	0.0
	0.0	-0.5	0.0	0.0	0.0	-3.5	4.4
	0.0	-0.4	-10.9	-19.5	-7.6	-1.7	-6.7
(d)	0.0	0.0	0.2	2.6	3.7	0.4	0.0
	0.0	6.4	0.0	0.0	5.5	2.5	3.7
	0.0	3.6	-7.0	-18.6	-7.5	0.8	0.5
(e)	0.0	0.0	0.0	-7.3	-3.6	0.0	0.0
	0.0	-0.5	0.0	0.0	1.5	13.3	0.2
	0.0	-0.4	-11.1	-19.6	39.8	3.3	-6.4
(f)	0.0	0.0	4.8	-6.0	-5.3	0.0	0.0
	0.0	-0.5	0.0	0.0	0.1	-5.6	2.4
	0.0	-0.4	-11.1	-19.6	-7.6	-1.4	-2.0
(g)	0.0	0.0	0.0	-1.8	-1.8	0.3	0.0
	0.0	-0.5	0.0	0.0	0.0	-0.3	0.0
	0.0	3.8	6.9	-7.2	-0.5	-1.6	-6.7
(h)	0.0	0.0	0.2	-5.6	-5.6	0.0	0.0
	0.0	5.3	0.0	0.0	0.0	0.7	0.0
	0.0	-0.4	3.0	19.0	2.0	0.6	-6.6
(i)	0.0	0.0	0.0	-0.2	-6.0	0.0	0.0
	0.0	0.2	0.0	0.0	0.0	-5.9	0.0
	0.0	-0.4	6.1	-10.3	22.6	11.0	-6.6

produce the spawning migration qualitatively. Although it is impossible to determine with certainty how organisms behave, one hopes to produce a model that is at least able to reproduce the behavior. Doing so with a model that uses interaction strength and measured environmental factors is therefore a significant result for the model being used.

Of special interest is how low the value of β is in Section 3.2. A low value resonates with the Discussion in Chapter 2, where we argue that the reaction time to neighbors is shorter than the reaction time to temperature, thus requiring a low value of β .

As noted in Section 3.2.2, the average initial spatial resolution Δq is similar to the radius of repulsion, r_r , for the simulations in Section 3.2.3. When a particle updates its directional heading, most of them take into account all neighboring particles which they could encounter in the next time step. This ensures that most particles tend to avoid collisions at each time step. However, faster moving particles could collide, or even travel past each other. Once the speed is drastically increased, particles could travel past each other, even through the zones of orientation. We need to choose the parameters carefully to avoid this problem. Shortening the time step or increasing the radii would ensure particles reacting to all neighboring particles. Finally, we see in Scenario (h) that doubling the radius of repulsion results in a more realistic migration pattern.

With our choice of Δt and v_k , in the simulations of the spawning migrations, each particle travels on average $\Delta q \simeq 0.12$ km per time step. This means that it takes a particle about 100 time steps to move from one grid point to another. Taking time steps that are too large for the grid resolution would force particles to skip over grid points, and therefore to miss the information located at these grid points. Refining the spatial resolution of the grid should go hand in hand with a refined temporal resolution. By choosing Δt and v_k as we have, we are simulating well within the limits of the spatial resolution of the environmental data,

thereby using all of the information available.

The sensitivity analysis showed that there is an interplay between the preferred temperature range and the currents around Iceland, thus affecting the route of the spawning migration. We see that if the upper bound of the preferred temperature range, T_2 is too high, the particles enter waters which normally should be too hot and get carried away with the fast currents. The temperature gradients off the southeast coast of Iceland have been observed to slow down migrating capelin, but with a high T_2 the particles moved past these boundaries. However, lowering the lower bound, T_1 , we see that particles linger in the north and do not enter waters with stronger currents, which carries them along their way to the spawning grounds.

The sensitivity analysis indicates that the value of β controls a fine balance between how strongly the particles sense their environment and the strength of interaction among particles. The value of β has to be high enough to allow a school to sense the environment, but low enough to allow it to enter water outside the preferred temperature range of the fish.

It is important to note that the value of β seems to affect where the particles come onto the continental shelf of Iceland. This is an interplay between the currents and the shape of the temperature contour lines around Iceland, see Figures 3.1 and 3.2, along with the upper bound of the preferred temperature range. The fast current off the southeast coast drives the particles into warm water, and in return the value of β determines how the particles respond to that warm water.

We also note that the values of β used in the scenarios are low. Even in the extreme case of Scenario (f) the value of β is 0.050. But in that scenario, the particles react so quickly to the temperature boundaries that they effectively reflect the whole school of particles hitting the boundary. The balance between neighbor interactions and temperature reaction is

indeed a fine one.

We note that the schools of particles in the simulations seem “thin” compared with acoustic measurements. Adding noise to the directional angle of the particles could have the effect of spreading them out. Noise has not been added into the simulations at this stage, to facilitate the interpretation of the behavior of the system. Future simulations will incorporate noise, which requires a statistical interpretation of the simulations.

The radius of repulsion effectively spreads out particles. With the value of r_r too small, the particles form dense schools which sense temperatures on a small scale, compared to larger and less dense schools. The Scenario (h), with the radius of repulsion double that of the reference case, does create a simulation which looks realistic and might be a better value than used in the reference case. In Section 4.3.1 we see that doubling the value of radius of repulsion is within reasonable biological bounds. We only explored one extreme case with the radius of attraction active, which had the effect of forming many dense schools. Since that behavior is uncharacteristic of capelin we have not investigated the parameter further.

Finally, we note that the radii of interaction are biological parameters for individual fish, and could be found from experiments. We show in Section 4.3.1 how the values used in the simulations of the spawning migrations should change, were we to simulate at the level of individual fish, and obtain biologically reasonable values.

4

Scaling of parameters

4.1 Introduction

We now focus our attention on the relationship between the number of particles in a simulation, the radii of interaction and the time step. As described in Section 2.3 the model is a discrete one, with an inherent biological reaction time, τ .

Optimally, one would have estimations of the reaction time, τ , and the radii of interactions, based on some measurements. The time step in the simulations would then be set to the reaction time, and the radii in the simulations would be determined by the values of the biological counterparts. Since data on these parameters are typically hard to measure, one must know how to handle different scenarios.

Preferably, one would be able to simulate at the level of individual fish. However, computational recourses do not allow such a feat in a reasonable time when it comes to the capelin. Stock sizes are usually measured in billions of individual fish, and we therefore have to make do with fewer particles in the simulations. These individual particles, each of which represents many individual fish, we call superindividuals.

We think of the superindividual as a school of fish, moving as a whole entity. The dynamics of a school of superindividuals need not be identical to the dynamics of a large school of individuals. Here, we assume that the superindividual follows the same equations of motion as the individual fish.

However, care must be taken when simulating under such circumstances. Both the radii of interactions and the time step are somehow related to the number of fish each superindividual represents. The time step and the reaction times of individuals, τ , versus the reaction times of superindividuals needs to be considered. The time step also holds hand in hand with the radii of interactions.

In [3] we presented arguments for how parameters of the interacting particle model should change when the number of particles is changed. In Section 4.2 we restate the model under investigation and describe the proposed scaling arguments in Section 4.3. We propose in Section 4.4 several measures to be used to investigate the veracity of the scaling arguments, and the behavior of the system of particles.

Numerical simulations for the scaling arguments are presented in Section 4.5. There, we show that with the scaling relationships between parameters in Section 4.3 we do in some sense achieve the same behavior in a system of individuals, across a spectrum of simulations with different number of particles. We show that the average number of neighbors stays constant. Of special interest is the system's dependence on the time step and how quickly the system of particles reaches a local consensus, which we discuss in Section 4.6.

4.2 Model description

We focus on the dynamics of the underlying interacting particle model without any environmental factors or a grid. For the sake of analysis, we

take the speeds $v_k(t) = v$ to be fixed. By fixing the speeds of the particles we ensure that the time step is the only parameter which affects how far a particle travels during each iteration.

The model under consideration consists of N particles in an area of size $L \times L$ with periodic boundary conditions. Particle k has position $\mathbf{q}_k(t)$ at time t as before. As before, we let $\theta_k(t)$ denote particle k 's directional angle at time t and

$$\mathbf{e}_k(t) := \begin{pmatrix} \cos(\theta_k(t)) \\ \sin(\theta_k(t)) \end{pmatrix} \quad (4.1)$$

thus denotes the unit direction vector of particle k at time t .

The equation for the movement of the particles is the same as Equation (2.2) but the directional angle is updated as

$$\begin{pmatrix} \cos(\theta_k(t + \Delta t)) \\ \sin(\theta_k(t + \Delta t)) \end{pmatrix} = \frac{\mathbf{d}_k(t)}{\|\mathbf{d}_k(t)\|}, \quad (4.2)$$

where the vector \mathbf{d}_k is the one in Equation (2.7). The zones of interactions are the same ones as before, they can be seen in Figure 2.1, and are discussed in Section 2.3.1.

We note that if the only sensory zone is the zone of orientation, the model is exactly that presented in [63] with $R = r_o$. In that paper, a phase transition was shown to occur in the thermodynamic limit, with directional noise as the temperature. We do not, however, add noise to the system, but analyze the system's behavior with varying particle density and parameter values.

4.3 Scaling arguments

For a given year, let F be the number of individual fish in the actual migration. We assume F to be constant, ignoring predation and other natural factors. Also, let N be the number of particles in a given simulation. Define $F^s := F/N$ to be the number of fish that each particle, or superindividual, represents in that simulation.

We let Δq denote the distance a particle travels in one time step at speed v . We note that the time step is related to the reaction time of individuals, τ , as described in Section 2.3. Here, the time step Δt is a parameter in the simulations and we use Δq as a measure of the spatial resolution in the simulations. The time step is implicitly taken to be the reaction time of individuals. The simple relationship $\Delta q = v\Delta t$ indicates that there is a linear scaling between the spatial and temporal variables:

$$\Delta q \propto \Delta t. \quad (4.3)$$

We note that Equation (4.3) also shows how the parameters should scale if the speed were varied. However, in our scaling simulations in Section 4.5, we fix the speed to be $v = 1$. By doing so, we have made the time step the parameter which determines the spatial resolution, Δq .

The radii of the zones of repulsion r_r , orientation r_o , and attraction r_a are parameters which are known in the literature to affect the behavior of the system [2, 12, 16, 27, 34, 35, 40]. We assume that $r_r \propto r_o \propto r_a$.

Each particle travels a distance of Δq at every time step and senses other particles within its sensory zones. In order for the movements and interactions among particles to be consistent across simulations, the radii of these sensory zones should also scale with Δq , i.e.

$$\Delta q \propto r_\gamma, \quad \gamma \in \{r, o, a\}, \quad (4.4)$$

and from (4.3) we see that the same holds for Δq replaced by Δt .

Now, when adding more particles to the system, we require the dynamics of the simulations to be comparable. Let us consider the number of fish in a region of area R , assuming uniform density. Let us now spread N superindividuals evenly throughout this region. Then each superindividual in effect represents the fish contained in an area of R/N . Thus, as the number of superindividuals increases, the number of fish which each particle represents decreases with this area. We assume that $(\Delta q)^2$ scales with the size of the area of the region which each superindividual represents. Accordingly,

$$\Delta q \propto \frac{1}{\sqrt{N}}, \quad (4.5)$$

or equivalently

$$\Delta q \propto \sqrt{F^s}, \quad (4.6)$$

because $F^s := F/N$. First, this ensures that the number of particles that each particle will interact with during one time step will not depend significantly on F^s . Second, from Equation (4.4), the same holds for the number of particles within each zone of interaction.

4.3.1 Case study

One ambitious goal of our research is to be able to simulate each fish in the migration, i.e. when the number of particles is the same as the number of fish, $N = F$. Using relations (4.3) through (4.6), it is of interest to investigate how the parameters should scale when we take $F^s = 1$, i.e. when each particle in the simulation corresponds to one fish.

In [3] we presented a simulation which successfully predicted the route of the spawning migration of the Icelandic capelin in 2008. In that simulation, the number of particles was in the order of 5×10^4 . A conservative estimate of the stock size of the migrating capelin is $F \simeq 5 \times 10^{10}$ indi-

vidual fish. Thus, the number of fish each superindividual represents in that case studies is $F^s \simeq 10^6$.

Now, let a superscript 0 denote the parameters and values of the above simulation. We gave these values in Section 3.2.2 but write them here with the superscript. Thus, $\Delta t^0 = 0.050$ days, or 4320 seconds. The initial speed was set on average to be $v_k^0 \simeq 2.4$ km/day and the corresponding spatial resolution is on average $\Delta q^0 \simeq 120$ meters. Once the particles increase their speeds to about 15 km/day, the corresponding spatial resolution increases to about 750 meters. The radius of repulsion was set $r_r^0 = 0.01$ grid units, or about 120 meters. The radius of orientation (and attraction) was set $r_o^0 = 0.10$ grid units, or about 1.20 km.

Now, we look at another simulation, with parameters N , Δt , and radii r_r and $r_o = r_a$, in which we want to have the same dynamics as the above simulation. We see that if the number of particles is changed, $N = \eta N^0$, then from Equations (4.3) and (4.5) we arrive at

$$\begin{aligned} \Delta t &\propto \frac{1}{\sqrt{N}} \\ &= \frac{1}{\sqrt{\eta N^0}} \\ &= \eta^{-1/2} \frac{1}{\sqrt{N^0}} \end{aligned}$$

which shows that

$$\Delta t = \eta^{-1/2} \Delta t^0. \quad (4.7)$$

From Equation (4.4) we see that the same holds for the radii, and that all parameters should scale by the factor $\eta^{-1/2}$.

When simulating individuals in the simulation of the 2008 spawning migration, we find $\eta = 10^6$. The spatial resolution turns out to be $\Delta q \simeq 12$ cm and the temporal resolution to be $\Delta t \simeq 4.3$ s. The radius of

repulsion scales down to $r_r \simeq 12$ cm, which is just under 1 body length. The radius of orientation scales to $r_o \simeq 1.2$ m. It is worth noting that these values are quite reasonable from a biological perspective [52, 53]. Furthermore, while modern computational capabilities may allow for simulations at this scale, allowing us to model at the level of an individual, it is of interest to establish whether the same results can be deduced by working with superindividuals at a much lower computational cost.

4.4 Measures

We now describe several pertinent measures which we use to determine the behavior of the system. The pertinent measures will be a global order parameter, an average local order parameter, and average number of neighbors, defined in Equations (4.8), (4.10), and (4.12), respectively. We describe in each section some characteristics of these measures.

In Section 4.5 we perform several simulations for each set of parameter values. A set of parameter values is used to define a base case which we use to compare other simulations to. In all simulations we find the values of the measures presented in this section. We argue that we are able to ensure that the parameters reach a steady state, which indeed turns out to be the case. In Section 4.4.6 we define how we find the time it takes for the system to reach these steady states and investigate the relaxation times' dependence on the parameters.

4.4.1 Global order parameter, R

Inspired by the order parameters commonly used to analyze synchronization in systems of coupled phase oscillators, e.g. the model presented by

Kuramoto [42] and in [63], we define

$$R(t) \begin{pmatrix} \cos(\Psi(t)) \\ \sin(\Psi(t)) \end{pmatrix} := \frac{1}{N} \sum_{i=1}^N e_i(t). \quad (4.8)$$

Here, $R(t)$ is a global order parameter of the system with $R \in [0, 1]$ for all t . The angle Ψ denotes the global direction angle.

It is clear that for $R = 1$ the whole school is completely synchronized, with all particles moving in the same direction. In a completely chaotic school, with particles moving in all directions, the value of R is zero. However, a low value of R could also be achieved with the particles breaking into smaller schools, each highly synchronized.

In Section 4.4.4 we establish what particle density, as a function of the radius of repulsion, is required in order to ensure that the connectivity of the system is high enough to avoid small unconnected schools. By ensuring high enough particle density, we can be sure that the system is highly connected, and can thus find the time it takes to reach equilibrium, as described in Section 4.4.6.

4.4.2 Average local order parameter, \bar{r}

We also define a local order parameter for each particle,

$$r_k(t) \begin{pmatrix} \cos(\psi_k(t)) \\ \sin(\psi_k(t)) \end{pmatrix} := \frac{1}{|I_k|} \sum_{i \in I_k} e_i(t), \quad (4.9)$$

where I_k is the set of indices of all the particles within particle k 's zone of interactions, see Equation (2.5) in Section 2.3.1.

Note that $r_k \in [0, 1]$ for all t and behaves similarly to R . However, if $r_k = 0$ (or close to zero) we know that because of the connectivity of neighbors of particle k , we have local chaotic behavior near particle k .

Finally, we define the average local order parameter,

$$\bar{r}(t) := \frac{1}{N} \sum_{i=1}^N r_i(t), \quad (4.10)$$

which will serve as a useful tool to determine the behavior of the system.

4.4.3 Global versus local

It is tempting to speculate whether that the value of the global order parameter will always be smaller or greater than that of the corresponding average local order parameter. If the number of particles is large and several schools exists, then generally $R \leq \bar{r}$ in simulations. However, this needs not be the case, as we show below.

We look at all possible arrangements for $N = 3$ which serve as examples for how particles can be arranged for a general N with R both smaller and larger than \bar{r} . We arrange the analysis in order of connections between particles, where two particles are said to be connected if they are within zones of interaction of one another.

$N = 3$, no connectivity

Here, every particle has no neighbors and so $r_i = 1$ for all i . We therefore have $\bar{r} = 1$ but it is clear that R can take any value in $[0, 1]$.

$N = 3$, one connection

Here, two particles are neighbors but the third particle is far away. We look at Figure 4.1(a) and see that $r_1 = r_2 = \frac{1}{2}\|e_1 + e_2\|$ and $r_3 = \|e_3\| = 1$. Thus, $\bar{r} = \frac{1}{3}(\|e_1 + e_2\| + 1)$.

$$R = \frac{1}{3}\|e_1 + e_2 + e_3\| \leq \frac{1}{3}(\|e_1 + e_2\| + \|e_3\|) = \bar{r}.$$

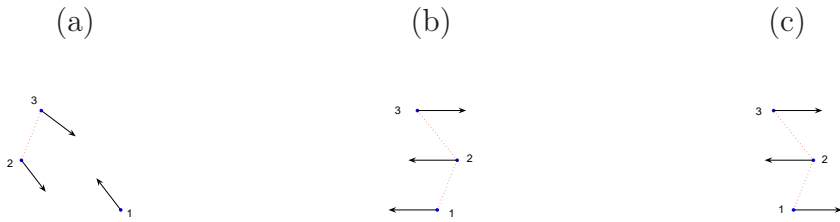


Figure 4.1: Configurations discussed in Section 4.4.3.

An example of inequality is shown in Figure 4.1(a) and easily verified.

$N = 3$, **two connections**

In this case, two particles have one neighbor but the third one is neighbor to both of the other ones. It is quite easy to find configurations with $R < \bar{r}$ and $R > \bar{r}$ where either R or \bar{r} is equal to 0 or 1. We therefore present the following cases:

- a) We look at the arrangement in Figure 4.1(b) with the following directional angles $(\theta_1, \theta_2, \theta_3) = (\pi, \pi, 0)$. We have $r_1 = 1$, $r_2 = 1/3$, and $r_3 = 0$, resulting in $\bar{r} = 4/9$. However, $R = 1/3$ and so $R < \bar{r}$.
- b) In Figure 4.1(c) we have $(\theta_1, \theta_2, \theta_3) = (0, \pi, 0)$ and so $r_1 = 0$, $r_2 = 1/3$, and $r_3 = 0$. We calculate $\bar{r} = 1/9$ and $R = 1/3$, thus $R > \bar{r}$.

$N = 3$, **all connected**

In this case we have $R = \bar{r}$ at all times.

We therefore see that a system of particles can at any time be either more globally synchronized than locally synchronized or vice versa. However, in Section 4.5 and from Figure 4.3, we see numerically that the system reaches local consensus much faster than a global consensus.

4.4.4 Particle density and the radii

We note that our scaling arguments assume a uniform density of particles. We therefore confine the system to a torus of size L^2 . By doing so we avoid problems with boundary issues and issues associated with infinite domains.

The particles' tendency to avoid other particles within their zone of repulsion will effectively spread out the particles. If the number of particles is high compared to the radius of repulsion, then the particles will spread out and the system eventually becomes path connected. However, the time it takes for the system to reach an equilibrium can vary greatly and will depend on the initial distribution of particles and their directional angles.

If the number of particles is low compared to the radius of repulsion, then the system can enter a long transient state where several small schools travel on their own, possibly eventually finding each other. When that happens, the evolution of the global and local order parameters will be characterized by periods of constant values, with sharp increases following initial fluctuations when schools collide and align. Eventually, the value of both order parameters will reach 1, unless e.g. two schools happen to circle the torus at a 90 degrees angle to each other and with frequency difference of 0.5, thus neither school senses the other and they never merge. The probability of the latter scenario will sharply drop to zero as the number of particles increases or as the radius of repulsion increases.

A particle has an area of repulsion of size πr_r^2 . We therefore see that we require $N \cdot \pi r_r^2$ to be greater than the whole area, L^2 , in order for the system not to linger in metastable partially synchronized states. We define

$$N_{min} := \frac{L^2}{\pi r_r^2} \quad (4.11)$$

and note that it is the minimal number of particles required for the system to maintain a path connected graph, where two particles are considered to be connected if they are within each others' zones of interaction. In the simulations below, Section 4.5, we let the number of particles be well above the minimum N_{min} in all cases.

Now, if the radius of repulsions is varied then the scaling arguments would require the number of particles to vary accordingly. For example, if the radius of repulsion is changed to one quarter of its original value, then both the number of particles, N , and N_{min} should double. The ratio between N and N_{min} is thus maintained across simulations. It is therefore clear that our scaling arguments indeed ensure consistency when it comes to N_{min} .

4.4.5 Average number of neighbors, \bar{n}

Now, let $n_k(t) := |I_k| - 1$ denote the number of neighbors which particle k has at each time step. We define the average number of neighbors of the system as

$$\bar{n}(t) := \frac{1}{N} \sum_{i=1}^N n_i(t). \quad (4.12)$$

Now, let us again assume that we are on a torus of size L^2 with N particles. If the particles are uniformly distributed then the particle density is N/L^2 . The average number of neighbors for particle k will be determined by all particles within its zone of attraction, and thus the average number of neighbors at uniform density is

$$\bar{n}_U := \frac{N}{L^2} \pi r_a^2 - 1, \quad (4.13)$$

where the neighbor being subtracted is the particle itself. We shall see in the simulations in Section 4.5 how the inclusion of the radius of repulsion

increases this value, resulting in a mostly uniform distribution with a ripply or wavy pattern, seen in Figure 4.2 (b).

By inspecting (4.13) we see that our scaling arguments indeed maintain \bar{n}_U constant. Below, in Section 4.5, we show that our scaling arguments also maintain the equilibrium value of \bar{n} constant, as expected.

4.4.6 Relaxation times to equilibrium

As mentioned above, one expects the system to reach a consensus with the value of both the global order parameter and the average local order parameter close to 1. With enough particles, this should be ensured and happen with few, if any, metastable transient states of partial synchrony. The system should therefore remain connected and we find the time it takes a system to reach an equilibrium state. To this end, we look at the order parameters from Equations (4.8) and (4.10). Indeed, by looking at Figure 4.3 from the base case, described below, the system does reach a consensus.

We run all simulations for long enough in order for the system to have fully relaxed to a steady state. As we see below, e.g. Figure 4.3(a), the order parameters both reach a value close to 1, meaning that the system is almost fully synchronized.

The average number of neighbors also reaches a steady state which we will define as

$$\bar{n}_E := \lim_{t \rightarrow \infty} \bar{n}(t). \quad (4.14)$$

In the simulations we define this value as the average of the last few hundred iterations, in which the system should have remained at equilibrium. In Figure 4.3(b) we see that the average number of neighbors does indeed reach an equilibrium value. We compare this value, which depends on the simulation parameters, to the average number of neighbors at uniform distribution, see (4.13).

Now, we define the consensus or equilibrium to have been reached if the measures have fallen within a certain range of the final value. We define ϵ_R , ϵ_r , and ϵ_n to be the deviation from the final values of R , \bar{r} and \bar{n} . The order parameters both have final values very close to 1 in all simulations. The final value of \bar{n} is defined as (4.14), and as mentioned above, is found as the average of the last few hundred iterations. We let t_R , t_r and t_n be the resulting relaxation times, which we define as the first time R , \bar{r} and \bar{n} remain within ϵ_R , ϵ_r , and ϵ_n of their final value, respectively.

It is not immediately clear how ϵ_R , ϵ_r , and ϵ_n should be chosen. Below, we investigate the relaxation times' dependence on these parameters by finding the resulting relaxation times for seven different values of ϵ_R , ϵ_r , and ϵ_n . These values and resulting relaxation times for each of the scenarios are given below in Tables 4.3, 4.4, and 4.5, respectively.

4.5 Simulations

We confine the simulations to a torus in order to avoid determining boundary conditions. In all simulations we fix $L = 10$, so the area (i.e. the torus) has size $L^2 = 100$. The particles' speed is kept constant at 1 unit/day. Thus, the time step is the only control parameter which determines the distance a particle travels at each time step, i.e. the spatial resolution of the system.

We choose a base scenario to which we compare other scenarios. The parameter values of the base Scenario (a) are given in (4.15), which the following scenarios modify, as described below. Each scenario consists of nine simulations.

The next three Scenarios (b)-(d) increase the number of particles by a factor of 4, thus simulating with $N = 200\,000$ particles. Scenario (b) varies parameter values according to the scaling arguments of Equations

(4.3) - (4.5). With the particles increased by a factor of 4, the radii and time step change by a factor of 1/2 in Scenario (b). In Scenario (c) we only change the radii by a factor of 1/2, but do not change the time step. Finally, Scenario (d) sees only the number of particles varied, and thus other parameter values are as in the base Scenario.

Scenarios (e)-(g) we take the number of particles to be a quarter of that of the base Scenario (a), thus simulating with $N = 12\,500$ particles. In Scenario (e), we scale the radii and time step in the same way as in Scenario (b), but now with a factor of 2. Scenario (f) only varies the radii but maintains the time step of the base scenario. Finally, Scenario (g) only varies the number of particles from that of the base scenario, similarly to Scenario (d).

Lastly, in order to further determine the system's sensitivity to the time step, we create two scenarios; one scenario with the time step halved, and one scenario with the time step doubled. Thus, we use the parameter values in (4.15), with the time step halved in Scenario (h), and the time step doubled in Scenario (i).

In each of these scenarios we choose one of the nine simulations and plot in Figures 4.3-4.6 the evolution of the global and average local order parameters, as well as the average number of neighbors. The simulations were run up to an absolute time of $t = 30$ even though the simulations were run for twice as long, because the relaxation times show that most simulations had reached an equilibrium by that time.

4.5.1 Scenarios (a)-(i)

We now describe the Scenarios (a)-(i) in more detail. Scenario (a) is a base scenario to which we compare the other scenarios. The parameter values of that scenario are as described in Equation (4.15). Variations from those parameter values are shown in Table 4.1.

(a)	N	r_r	r_o	Δt
(b)	$4N$	$r_r/2$	$r_o/2$	$\Delta t/2$
(c)	$4N$	$r_r/2$	$r_o/2$	
(d)	$4N$			
(e)	$N/4$	$2r_r$	$2r_o$	$2\Delta t$
(f)	$N/4$	$2r_r$	$2r_o$	
(g)	$N/4$			
(h)				$\Delta t/2$
(i)				$2\Delta t$

Table 4.1: A description of how the Scenarios (b)-(i) vary from the base Scenario (a). Values of the parameters of the base Scenario (a) are given in (4.15).

The number of interactions was chosen to be 6000 in the base Scenario (a) which results in the absolute time of 60 (days). This value was found by trial and error in order to ensure that the system indeed had relaxed to a steady state. Scenarios (c), (d), and (g) are run for the same number of iterations. In the other scenarios the time step changes, and we change the number of iterations so that the same absolute time of 60 (days) is achieved.

We performed 9 simulations for each set of parameter values, because the initial spatial distribution and angular distribution were set randomly. However, with the large number of particles and radius of repulsions we claim that the system is path connected. The resulting values shown in Tables 4.2-4.5 are the average values from the 9 simulations of each scenario.

Figures 4.3-4.6 show plots of the evolution of the global order parameter, average local order parameter, and the average number of neighbors from one of the nine simulations of each scenario.

(a) Base Scenario

The following values of the radii and the time step were used as a base case scenario:

$$\begin{aligned}
 N &= 50000 \\
 r_r &= 0.120 \\
 r_o &= 0.240 \\
 r_a &= 0.240 \\
 \Delta t &= 0.010
 \end{aligned} \tag{4.15}$$

We see that with the parameter values and $L = 10$ as the size of the torus, we get $N_{min} \simeq 2210$ particles. With fifty thousand particles we are well above the required number of particles needed for the system not to linger in metastable partially synchronized states. And indeed the system quickly reaches a steady state of consensus.

We note that the above parameter values are different from the ones in Equation (3.1), used in the simulation of the 2008 spawning migration in Section 3.2.3. There, the ratio r_r/r_o was 0.1, whereas it is 0.5 with the parameter values from (4.15). In the Scenarios described below, we therefore keep in mind that the repulsion is stronger than in the simulation of the 2008 spawning migration. However, as discussed in Section 3.4, the ratio between the radius of repulsion and the spatial resolution small, allowing some particles to collide. With parameter values as in (4.15) we note that particles travel $v\Delta t = 0.010$ units per time step, thus meaning that once particles are within each others' zone of repulsion, they should be about 5 time steps apart, which gives them time to react accordingly.

(b) Scaling of parameters, $4 \cdot N$

In Scenarios (b)-(d) we quadruple the number of particles to that of the base Scenario (a), resulting in 200 000 particles. Here, in Scenario (b),

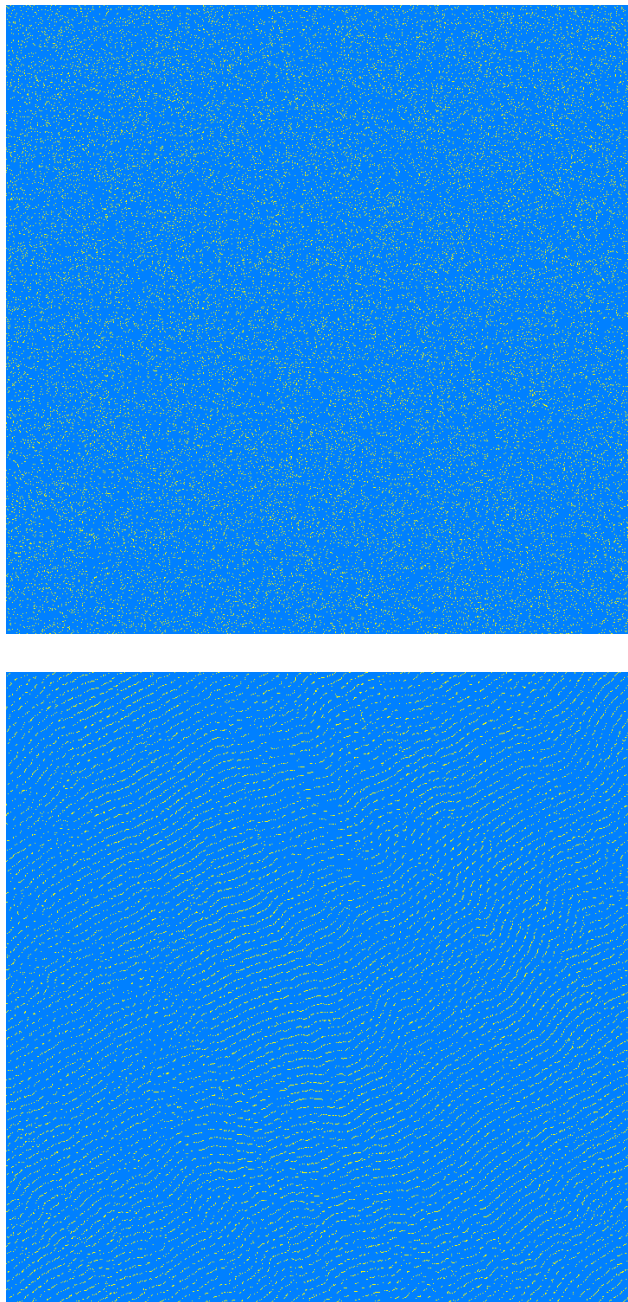


Figure 4.2: A simulation of the base Scenario (a) with 50.000 particles. Top: The initial distribution of particles. Bottom: Final distribution at equilibrium after 6000 iterations with time step $\Delta t = 0.01$. We discuss the peculiar “wave” pattern in Section 4.7.

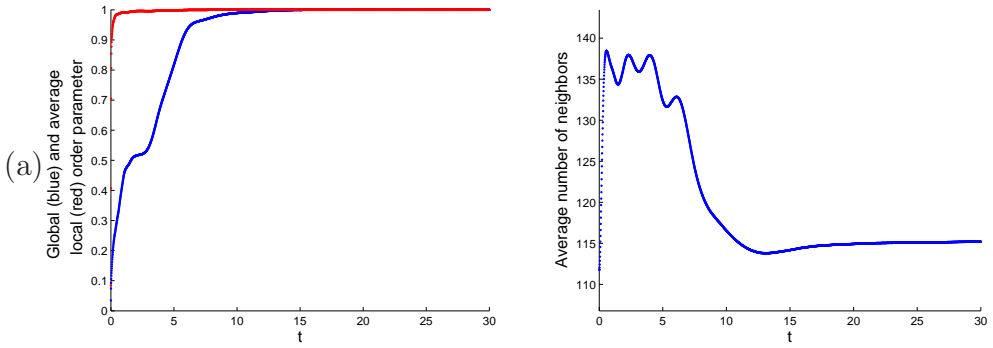


Figure 4.3: A simulation of the base scenario (a) with 50 000 particles. Left: The global order parameter, R , and the average local order parameter, \bar{r} . Right: The average number of neighbors, \bar{n} .

we vary the radii and the time step according to the scaling arguments of Section 4.3, see (4.3) - (4.5). Since the number of particles was changed by a factor of 4, the radii and time step were halved.

In Figure 4.4 we show the evolution of the global order parameter, average local order parameter, and the average number of neighbors for the Scenarios (b)-(c).

(c) Scaling of parameters except time step, $4 \cdot N$

Here, the number of particles was set to $N = 200\,000$ and the time step kept the same as in the base Scenario (a). However, the radii were changed according to the scaling arguments, thus halving the radii.

(d) Changing only the number of particles, $4 \cdot N$

The number of particles is again $N = 200\,000$ particles. Both the time step and the radii are the same as in the base Scenario (a). We therefore investigate how the system depends on the number of particles.

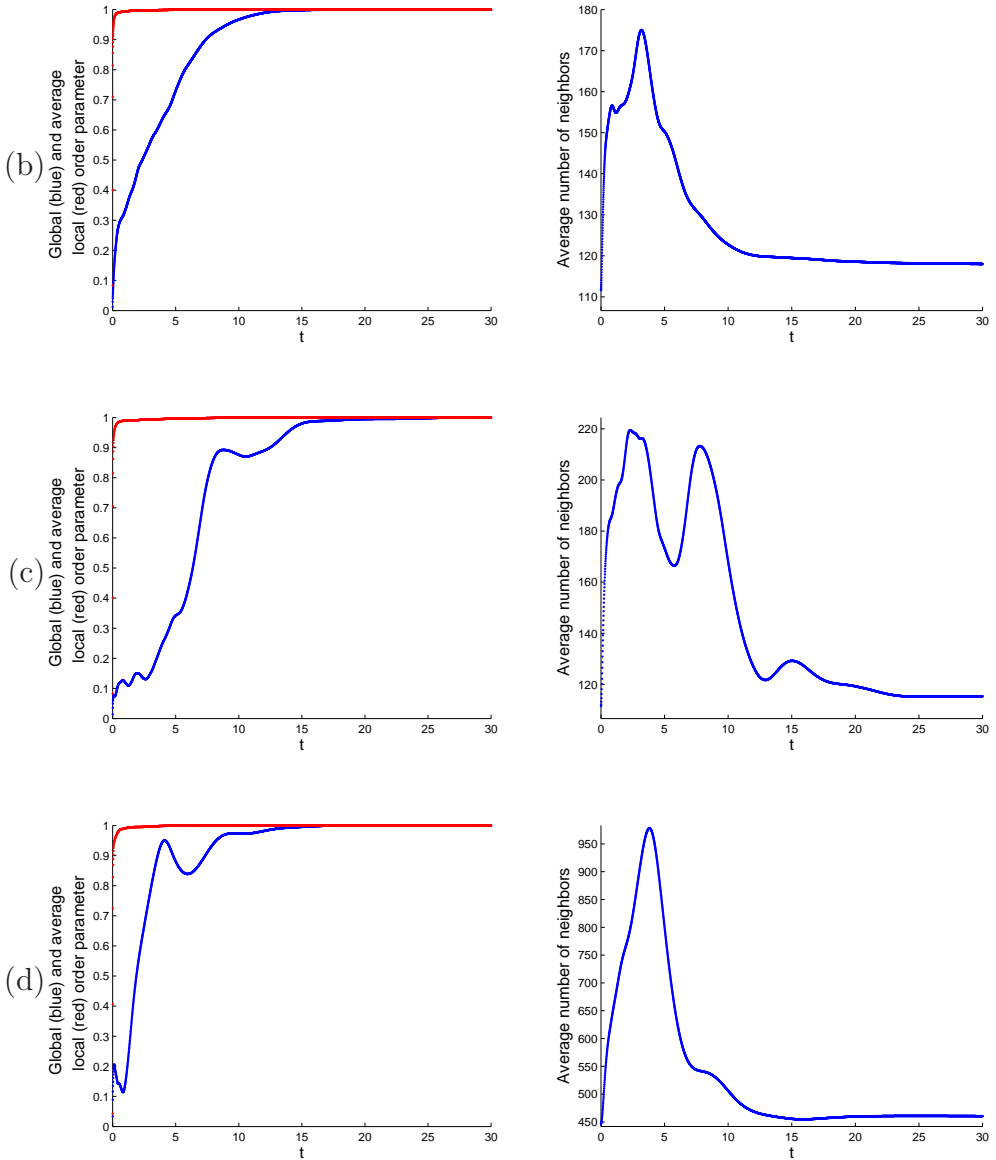


Figure 4.4: A simulation of the Scenarios (b), (c), and (d), described in Section 4.5.1. The number of particles is $N = 200\,000$ in all scenarios. The time step is (b) $\Delta t = 0.005$, (c) $\Delta t = 0.010$, and (d) $\Delta t = 0.01$. Left: The global order parameter, R , and the average local order parameter, \bar{r} . Right: The average number of neighbors, \bar{n} .

(e) Scaling of parameters, $\frac{1}{4} \cdot N$

Scenarios (e)-(f) correspond to the Scenarios (b)-(d) but we now take the number of particles to be one quarter of that of the base Scenario (a), resulting in $N = 12\,500$ particles. Here, in Scenario (e), we vary the radii and the time step according to the scaling arguments of Section 4.3, see (4.3) - (4.5). Since the number of particles was changed by a factor of $1/4$, the radii and time step were doubled.

In Figure 4.5 we show the evolution of the global order parameter, average local order parameter, and the average number of neighbors for the Scenarios (e)-(g).

(f) Scaling of parameters except time step, $\frac{1}{4} \cdot N$

Similarly to Scenario (e), we set the number of particles to $N = 12\,500$, now one fourth of that of the base Scenario (a). The time step was kept the same, but the radii were changed according to the scaling arguments, thus halving the radii.

(g) Changing only the number of particles, $\frac{1}{4} \cdot N$

We now investigate how the system reacts to only changing the number of particles, similarly to Scenario (d). Here, we take a quarter of the base Scenarios's, resulting in $12\,500$ particles. The time step and the radii are the same ones as in the base Scenario (a) and Scenario (d).

(h) Only time step, $\frac{1}{2} \cdot \Delta t$

Finally, we create two scenarios where only the time step is changed. In this Scenario (h), the time step is halved. The other parameter values are the same as in the base Scenario (a).

In Figure 4.6 we show the evolution of the global order parameter, average local order parameter, and the average number of neighbors for

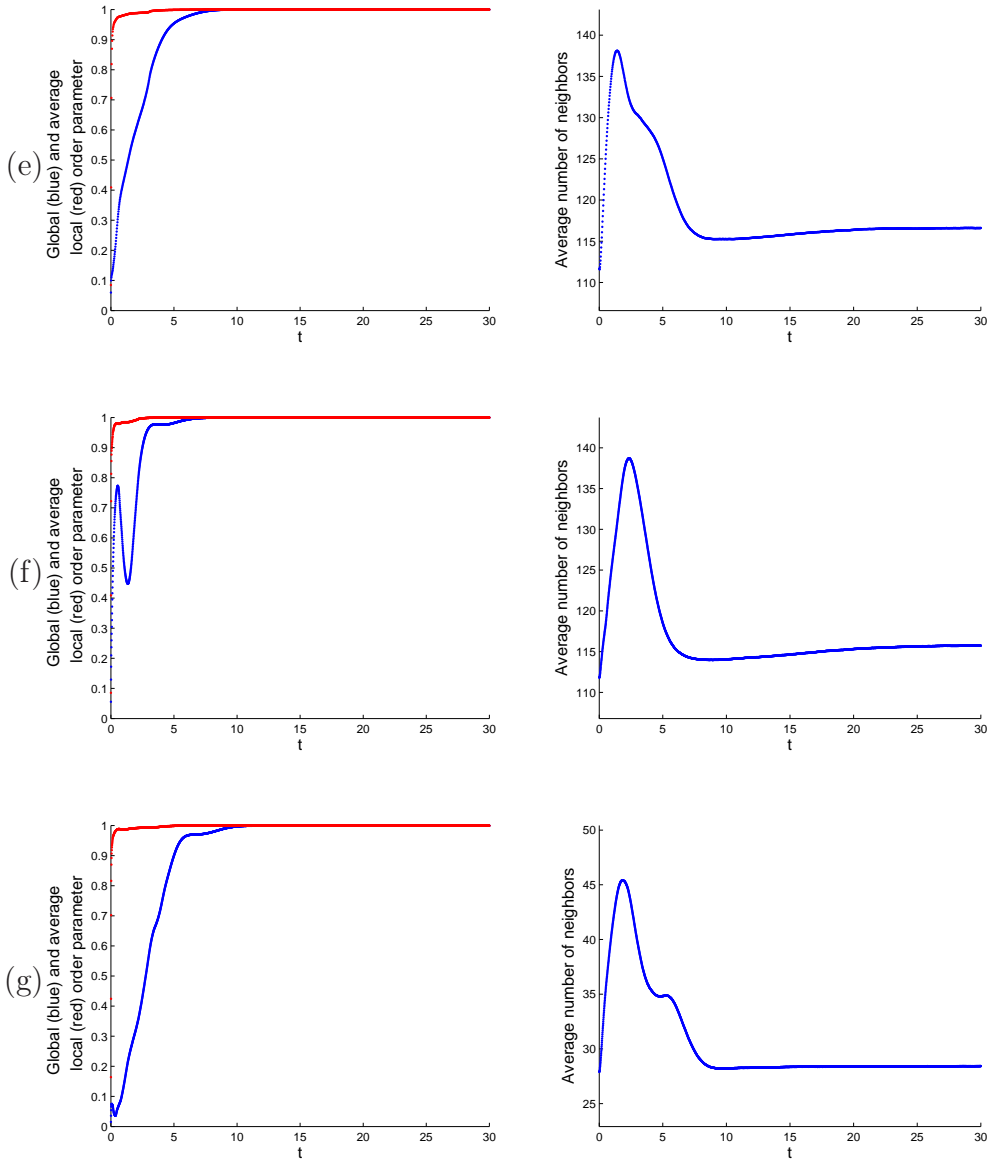


Figure 4.5: A simulation of the Scenarios (e), (f), and (g), described in Section 4.5.1. The number of particles is $N = 12\,500$ in all scenarios. The time step is (b) $\Delta t = 0.02$, (c) $\Delta t = 0.010$, and (d) $\Delta t = 0.01$. Left: The global order parameter, R , and the average local order parameter, \bar{r} . Right: The average number of neighbors, \bar{n} .

the Scenarios (h) and (i).

(i) Only time step, $2 \cdot \Delta t$

Again, similarly to Scenario (h), we change only the time step and maintain other parameter values of the base Scenario (a).

We note this since the time step was doubled, the simulations require only 3000 iterations in order for the absolute time in the simulations to be 60 (days) as in the other scenarios. Since it was a possibility that with a larger time step the system would not reach an equilibrium, we ran the simulations for 6000 iterations. However, the results are very similar considering 3000 or 6000 iterations.

4.6 Results

Scaling of parameters

A good result of the scaling arguments are how parameters of the simulation of the 2008 spawning migration, scale down to biologically realistic values at the individual lever, as found in Section 4.3.1. We note that the radius of repulsion should scale down to about one bodylength. However, this value could even be doubled to remain within realistic bounds [52,53]. As described in Section 3.4 we obtained an even better simulation of the 2008 spawning migration than the one presented in Section 3.2.3, by doubling the radius of repulsion. In that simulation, the particles were more realistically spread out, and formed larger schools. Future simulations of spawning migrations could therefore be made with a doubled radius of repulsion as that of Equation (3.1). A double radius of repulsion would result in each particle having fewer neighbors, thus reducing the computational cost of the simulations.

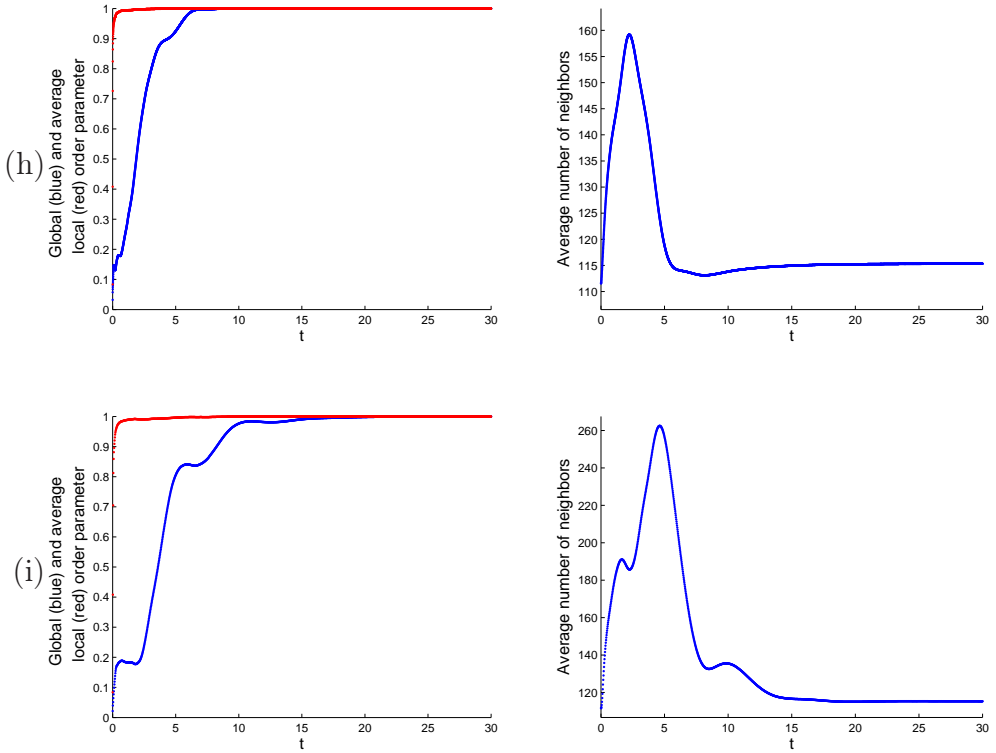


Figure 4.6: A simulation of the Scenarios (h) and (i) described in Section 4.5.1. The number of particles is $N = 50\,000$ in both scenarios. The time step is in (h) $\Delta t = 0.005$ and in (i) $\Delta t = 0.02$. Left: The global order parameter, R , and the average local order parameter, \bar{r} . Right: The average number of neighbors, \bar{n} .

	\bar{n}_E	\bar{n}_U	\bar{n}_E/\bar{n}_U
(a)	116.2	89.5	1.298
(b)	116.5	89.5	1.302
(c)	116.2	89.5	1.298
(d)	463.0	360.9	1.283
(e)	116.0	89.5	1.296
(f)	115.6	89.5	1.292
(g)	28.6	21.6	1.324
(h)	115.4	89.5	1.289
(i)	116.0	89.5	1.296

Table 4.2: Average number of neighbors, \bar{n}_E from Equation (4.14), and \bar{n}_U from Equation (4.13), from the Scenarios (a)-(i) described in Section 4.5.1.

Simulations of Scenarios (a)-(i)

We now simulate the Scenarios (a)-(i) described in Section 4.5.1. The parameter values of the base Scenario (a) are given in Equation (4.15). Table 4.1 shows the difference between the base Scenario (a) and the Scenarios (b)-(i), by showing which parameters were varied. Figures 4.3-4.6 show plots of the evolution of the global order parameter, average local order parameter, and the average number of neighbors from one of the nine simulations of each scenario.

We find for each scenario the resulting average number of neighbors, \bar{n}_E , and the expected number of neighbors at a uniform distribution, \bar{n}_U . The values, along with the ratio \bar{n}_E/\bar{n}_U , are given in Table 4.2.

The resulting relaxation times, t_R , t_r , and t_n from Section 4.4.6, are shown in Tables 4.3, 4.4, and 4.5, respectively. The tables show the relaxing times for seven different values of ϵ_R , ϵ_r , and ϵ_n for each scenario.

ϵ_R :	0.1	0.05	0.04	0.03	0.02	0.01	0.005
(a)	6.37	8.10	8.45	8.84	9.31	10.30	11.90
(b)	6.95	8.53	8.85	9.21	9.61	11.53	13.54
(c)	11.35	14.40	14.94	15.98	16.83	18.11	21.59
(d)	6.07	7.80	8.14	8.50	9.72	11.12	12.32
(e)	3.20	4.09	4.38	4.69	6.16	7.27	7.27
(f)	1.84	2.13	2.40	2.80	3.89	4.81	5.65
(g)	5.06	5.86	6.26	7.40	8.58	9.48	10.16
(h)	3.80	4.74	4.92	5.11	5.64	6.27	7.13
(i)	7.74	9.51	10.46	11.04	12.70	14.43	16.42

Table 4.3: Average relaxation times, t_R , of the global order parameters, R , from the Scenarios (a)-(i) described in Section 4.5.1.

ϵ_r :	0.1	0.05	0.04	0.03	0.02	0.01	0.005
(a)	0.07	0.16	0.20	0.28	0.44	1.06	2.80
(b)	0.03	0.08	0.09	0.13	0.19	0.48	1.13
(c)	0.06	0.12	0.15	0.21	0.33	0.79	2.11
(d)	0.06	0.15	0.19	0.25	0.43	1.17	3.21
(e)	0.12	0.26	0.32	0.42	0.76	2.43	3.01
(f)	0.08	0.22	0.28	0.36	0.66	1.35	1.73
(g)	0.07	0.16	0.20	0.27	0.39	0.99	2.64
(h)	0.03	0.10	0.12	0.17	0.28	0.63	1.54
(i)	0.13	0.25	0.31	0.42	0.74	1.91	3.94

Table 4.4: Average relaxation times, t_r , of the average local order parameters, \bar{r} , from the Scenarios (a)-(i) described in Section 4.5.1.

ϵ_n :	5	4	3	2	1	0.5	0.25
(a)	9.6	10.0	10.5	12.3	16.4	19.1	21.59
(b)	10.2	10.9	11.3	12.9	15.9	19.5	24.1
(c)	18.3	19.6	20.2	21.0	23.8	28.9	32.04
(d)	16.0	16.7	17.9	18.7	23.9	29.0	35.1
(e)	6.6	6.89	7.4	9.5	14.1	22.8	30.16
(f)	4.5	4.7	5.1	6.2	11.0	20.1	28.7
(g)	6.03	6.36	6.73	7.19	7.99	9.29	12.8
(h)	4.90	5.07	5.31	7.71	10.26	12.66	17.16
(i)	13.63	14.40	15.48	16.47	21.04	25.56	31.46

Table 4.5: Average relaxation times, t_n , to the average number of neighbors, \bar{n}_E , from the Scenarios (a)-(i) described in Section 4.5.1.

Number of neighbors

Now, by inspecting the values in Table 4.2 we see that the resulting average number of neighbors, \bar{n}_E , is higher than the expected number of neighbors, \bar{n}_U . The expected number of neighbors is $\bar{n}_U = 89.5$ neighbors, except for Scenarios (d) and (g), and the average number of neighbors was roughly $\bar{n}_E = 116.0$. In Scenario (d) only the number of particles was increased, resulting in more particles being within the zones of interaction. Similarly in Scenario (g), only the number of particles was decreased. However, the ratio \bar{n}_E/\bar{n}_U is about 1.298 which remarkably holds true for approximately all the simulations. We discuss a possible explanation below in Section 4.7.

It is worth noting that there is very little variance in the resulting average number of neighbors in the simulations of the scenarios. The variance is in all scenarios less than 2 neighbors, which means a variance of less than 1%.

Finally, we note that in all Figures 4.3 - 4.6 of the average number of neighbors, we see a sharp initial increase in the number of neighbors.

The system then finally relaxes to an equilibrium value. In some cases, e.g. Figure 4.5(f) the peak is smooth, but in Figure 4.3 the peak is quite rough. Figure 4.4(c) shows two peaks, but it is interesting to note that the corresponding order parameters do not appear to reflect this behavior.

Relaxation times

We now look at the resulting values for the relaxation times t_R , t_r , and t_n , which are given in Tables 4.3 - 4.5. Table 4.1 gives a visual overview of the parameters in each scenario.

Now, Scenarios (b) and (e) are the versions of the base Scenario (a) which maintain full scaling according to our scaling arguments. We see that t_R is similar in Scenarios (a) and (b), but note that this is not the case for t_r , where the values in Scenario (b) are approximately half those of Scenario (a). However, in Scenario (e) the relaxation time t_R is significantly lower than in Scenario (a), even though the time step was scaled with other parameters.

Scenarios (c) and (f) changed all parameter values except the time step. Even though the average number of neighbors is maintained, the global relaxation time t_R almost doubles from Scenario (a) when the number of particles is quadrupled in Scenario (c). However, this behavior is reversed for the local relaxation time t_r . Scenario (f) has a quarter of Scenario (a)'s number of particles and the global relaxation times are close to being halved.

We also see that even though the number of particles in Scenarios (d) and (g) are the same as in Scenarios (c) and (f), the global relaxation time is similar to the base Scenario (a). In fact, the only difference between the base Scenario (a) and the Scenarios (d) and (g) is the number of particles.

Changing only the time step in Scenarios (h) and (i), has a similar effect on the global relaxation time t_R as on the local relaxation time t_r ,

which we discuss directly below.

Looking at the local relaxation times t_r , we see that the most influential parameter is the time step. We note that this dependence on the time step is not as pronounced for the global relaxation time, t_R . Scenarios (c), (d), (f), and (g) have the same time step as the base Scenario (a), and the relaxation times to local consensus are very similar to the base scenario. In Scenarios (b) and (h), halving the time step has the effect of halving the relaxation times. Similarly, doubling the time step in Scenarios (e) and (i) doubles the relaxation times. We note that the relaxation times are given in absolute time which means that in both cases, i.e. in Scenarios (b), (e), (h), and (i), the simulations have taken a similar number of time steps to reach the consensus.

Finally, we observe the relaxation time t_n . As with the relaxation time t_R , Scenario (b) has a similar relaxation time t_n to Scenario (a), and Scenario (e) has a relatively lower relaxation time t_n . Scenarios (c) and (f) exhibit similar behavior compared to Scenario (a) with respect to both t_n and t_R . However, t_n differs from t_R in Scenarios (d) and (g), by being similar to Scenarios (c) and (f). Finally, in Scenarios (h) and (i), where only the time step was changed from Scenario (a), we see that t_n is affected in a similar way as the relaxation times t_R and t_r .

Perhaps the most noteworthy conclusion is that for both the relaxation times t_R and t_r we maintain the closest resemblance to the reference case when we only change the number of particles in Scenarios (d) and (g), whereas for the relaxation time t_n , we maintain the closest resemblance by adhering to the full scaling in Scenarios (b) and (e). Another interesting result is $t_r \ll t_R$, which we discuss below.

Global vs. local relaxation time

Of particular interest is how quickly the system of particles reaches a local consensus, even though the value of either of the two order parameters

can be larger than the other as we showed in Section 4.4.3. This means that locally the system reaches a consensus, but the whole system is not completely aligned yet. We see that the relaxation time for the average local order parameter is much lower than the relaxation time for the global order parameter, requiring $\epsilon_r \ll \epsilon_R$ in order to fully explore the relaxation time for average local order parameter. The local consensus is even maintained when the global order parameter passes through several levels of consensus, as clearly seen in Figure 4.4 from Scenario (d).

It is fairly easy to convince oneself that this phenomenon is due to local interactions aligning particles effectively, since the time step denotes in this case the reaction time to neighbors. Thus, locally the particles adjust to their neighbors in an efficient manner, but the discrepancies can gradually build up over larger distances, causing a lower value of the global order parameter. However, the groups in turn interact, sending and receiving information, and it takes that information time to propagate through the whole system and for all the groups to align. This difference could be one way to measure the propagation speed through a school of particles.

4.7 Discussion

Radii of interactions and temperature weight factor

A point of interest is the relationship between the temperature weight factor β , the time step, Δt , the radii of interaction, r_r , r_o , r_a , and the number of particles in a simulation, N . The weight factor governs how strongly each particle reacts to the environmental data versus the interactions at each iteration. It depends on the reaction time τ and thus the time step used. The radii of interactions are somehow linked to the individuals' vision, and in the case of the capelin, to the sensing of the

lateral line. We argue a linear relationship between the weight factor and the time step.

Both the weight factor and the radii are therefore intrinsic parameters to the organism at hand. Optimally we would know the values of the weight factor, radii and the reaction times. If we are not able to simulate at the level of individuals, the values of these parameters would then scale according to our scaling arguments, as computational powers allow. Now, the scaling arguments hold for a simulation of identical situations. The number of individual fish varies from year to year, which would result in different parameter values needed for the simulations. However, the dynamics of the system of particles could change, which could explain some of the differences between migration routes.

Pattern formation

In Figure 4.2(b) we see a pattern at equilibrium which all simulations exhibit. This pattern can be described as a “wave” pattern, or alternatively as a “ripple” pattern. The reason for this emerging pattern is not obvious, and one might have expected a uniform distribution of particles.

The pattern could be due to the presence of the zone of repulsion in the simulations. In fact, the ratio between the resulting average number of neighbors, \bar{n}_E , and the expected number of neighbors, \bar{n}_U , could be related to the ratio of the zone of repulsion and the zone of orientation. Another note of interest regarding the pattern is the distance between the waves. As with the ratio, it is interesting to investigate whether this distance can be linked to the radius of repulsion and possibly other parameters. Investigation of all these phenomena is a subject of further research [17].

Part II

Dynamic Energy Budget models

5

Dynamic Energy Budget (DEB) model

5.1 Introduction

In this part of the thesis we consider a Dynamic Energy Budget (DEB) model which is a model for the energy uptake and usage of individuals. We focus our attention to female capelin, because they determine several aspects of the migration, as explained in Section 1.3 and mentioned briefly below. We tailor the DEB model to the Icelandic capelin and estimate several of the species-specific parameters. Furthermore, we introduce a new variable to describe the roe production of capelin, and then compare the output of the DEB model to data from the Marine Research Institute of Iceland. This chapter is mostly based on [18].

The model in Part I, presented in [3], used no maturity model and only indirectly included that effect in the simulations. It is however well known that the stage of maturity has a significant effect on the behavior on migrating capelin [64, 65]. When mature capelin return from the feeding grounds to the continental shelf north off Iceland, they prefer

relatively cold waters. As they start their spawning migration they have been reported to slow down and even come to a halt upon reaching warmer waters near the southeast of Iceland [64, 65].

The capelin normally stay on the colder side of the sharp temperature boundaries between the warm Atlantic water and the colder water until the weight of the female ovaries is about 8%-10% of their total body weight. They commonly increase their speeds at this point and have been recorded to swim at about 15 km d^{-1} , and 25 km d^{-1} including the effect of translation by currents [64]. As they enter the warm waters their roe production increases rapidly, as does their metabolism. After entering the warm waters they have a limited time to spawn, and it is crucial for them to succeed in finding suitable spawning grounds. This happens relatively fast, in several days, and it is important for a model to capture this aspect of the spawning migration of the capelin.

It is therefore clear that inner dynamics of individual capelin play an important role in the route and timing of the spawning migration. Following on the work of [5], who proposed a bioenergetics model to be integrated into a capelin migration model, and [4], we have developed and implemented the DEB model to capture the growth, energy usage, and roe production of individual capelin. In Chapter 6 we describe how we combine the DEB model with the interacting particle model of Part I. By doing so we hope to capture most of the characteristics of the spawning migration of the Icelandic capelin.

In Section 5.2 we describe the DEB theory, and in Appendix A we show the derivations of the equations of the standard DEB model. Appendix B shows how growth equations of von Bertalanffy can be derived from the DEB model. Data from the Marine Research Institute of Iceland (MRI) and Matis, an Icelandic Food and Biotech R&D, is described in Section 5.3. In Section 5.4 we describe how the observable quantities such as length, weight, fat content and roe content, are related to the

state variables of the DEB model. We fit parameters to the data from the MRI and Matis, and present the results in Section 5.5.

5.2 DEB theory

Dynamic Energy Budget (DEB) theory is the study of the mechanisms of acquisition and use of energy by individuals, that has consequences in physiological organization and the dynamics of populations and ecosystems. It is closely related to bioenergetics that focuses on molecular aspects and metabolic pathways in a thermodynamic setting. DEB theory treats individuals as nonlinear dynamics systems that follow predictable patterns during their life cycle. This approach has firm physiological roots and provides a sound basis for population dynamic theories [38,51]. We refer to [38] for a full description of the DEB theory. A conceptual introduction is given in [37], and further guides and discussion can be found in [61] and [59].

DEB theory is ultimately the theory of life. Its aim is to describe all life forms within the same framework. The complexity of the DEB model will depend on the complexity of the species at hand. For the Icelandic capelin, we use a basic form of the DEB model with one food substrate and one type of reserve. These assumptions can be generalized [38].

DEB theory has been successfully applied to anchovy (*Engraulis engrasicolus*) in the Bay of Biscay [56] where their whole life cycle was modeled. The capelin and anchovies are similar fish in size and energetics, and both store energy mostly as lipids in their muscle. We fit the DEB parameters to the data on capelin and compare the resulting parameter values to those of the anchovies, obtaining similar results.

In Section 5.2.2 we give a brief account of the state variables of the standard DEB model. Although the equations for the state variables can be found in [39] and [38], we derive the equations in Appendix A

because the connection between the original state variables and the resulting equations is by no means obvious or straight forward.

The standard DEB model does not specify the dynamics of roe production, since the details of reproduction differs greatly between species. Producing roe is a particular feature of most species of fish. That aspect has to be dealt with for the species at hand, and we introduce a new variable to account for the roe production of individuals in Section 5.2.4.

5.2.1 The κ -rule:

According to DEB theory, each individual allocates a fixed fraction κ of utilized energy from reserves to growth and somatic maintenance. The rest, $(1 - \kappa)$, is then allocated to maturity maintenance and reproduction. This energy flow can be seen in Figure 5.1. The energy has been converted from food with constant efficiency. The DEB theory states that the value of κ stays fixed throughout the whole life cycle of an individual. It is species-specific and therefore is one of the characteristic parameters of each species. In Section 5.5 we obtain a relatively low value for κ compared to other fish, which we discuss below in Section 5.6.

We note that energy requirements due to swimming could be accounted for as part of the utilized energy for growth and maintenance, as shown on Figure 5.1. These requirements would depend on swimming speeds, but are not taken into account here. We do believe that this energy expenditure is not necessary because the capelin are a small constantly moving animal, making this energy expenditure fairly constant.

5.2.2 State variables

The state variables of the standard DEB model are structural volume, reserve energy, maturity energy and reproduction energy. These variables are not directly observable and have complex dynamics. Measur-

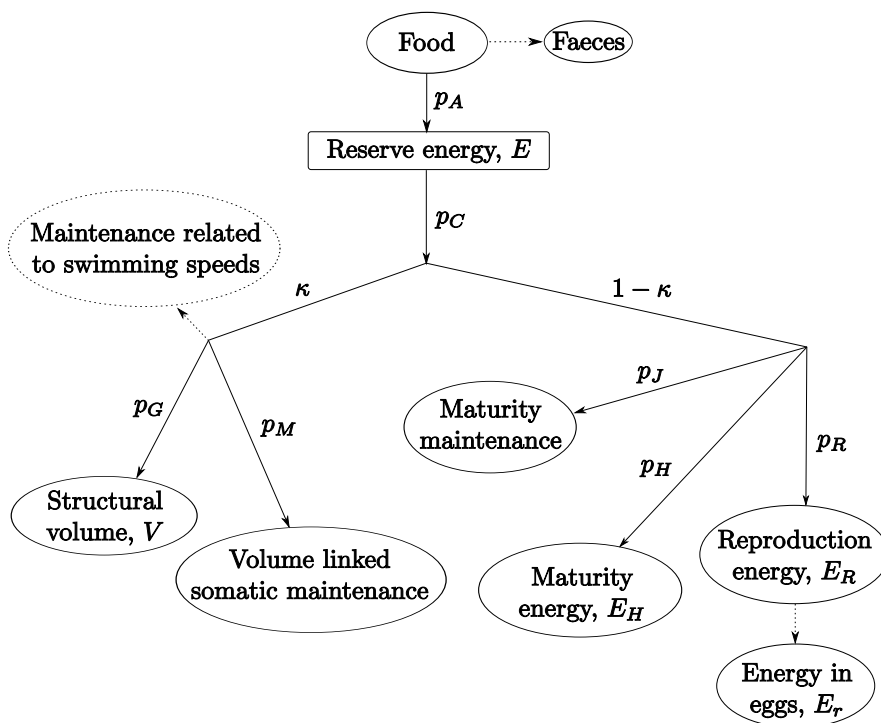


Figure 5.1: Energy fluxes and the κ -rule. It is assumed that a fixed fraction κ of utilized energy flows to structural volume and somatic maintenance. See Section 5.2.1.

able quantities have contributions from one or more state variables as described in Section 5.4 below. We now give a brief description of the state variables and the dynamics involved.

The structural volume, V (cm^3), is the amount of biomass. The dynamics are such that maintenance is assumed to take precedence over growth. The contribution of energy reserves and reproduction energy to structural volume is assumed to be small, hence we quantify structure with length [62]. We let the variable $L = V^{1/3}$ denote the structural (volumetric) length of an individual, which relates to actual physical length as detailed in Section 5.4.1.

The reserve energy, E (J) is the energy available to the individual. Its source is food uptake and it is the energy an organism utilizes for growth and somatic maintenance on one hand, and maturity, reproduction and maturity maintenance on the other hand.

Following [39] and [59], we let E_H denote a maturity energy in order to determine the onset of puberty. It is important to note that this variable is abstract and does not contribute directly to the weight of the fish. Initially, energy is allocated to this variable, and the maturity maintenance will be a fraction of this energy, $k_J E_H$. When E_H exceeds a certain threshold, E_H^p , the fish is mature and allocation of energy to E_H ceases.

Thus E_H reaches a final value E_H^p which determines when an individual reaches puberty. It is important to note that puberty is therefore neither determined by the volumetric length nor the physical length of a fish. Data corroborate this fact, as there is a great variance in the physical length of individuals at the onset of puberty.

After puberty has been reached, the energy starts to flow to E_R , which is the total energy available for reproduction. This energy will, in turn, be converted into roe. We assume that the dynamics of the energy flow to maturity is the same as that to reproduction. In other words, both

dE_H/dt and dE_R/dt have the same form, except that the former one is nonzero when $E_H < E_H^p$ but after that point is reached, the latter flow becomes nonzero. We assume that there are no maintenance costs associated with E_R , but maturity still requires maintenance of $k_J E_H^p$, explaining the term in Equation (5.8).

In Section 5.2.4 we introduce E_r as the energy converted from the reproduction energy to eggs. We assume that there are no maintenance costs associated with roe. This quantity is not a state variable in the DEB theory and has to be specified for the species in question, as well as its dynamics.

5.2.3 Equations of the standard DEB model

We non-dimensionalize the standard state variables of the DEB model, E , V , E_H , and E_R , and obtain the non-dimensional variables e , l , u_H , and u_R , respectively, where

$$E = [E_m] L_m^3 e l^3 \quad (5.1)$$

$$V = (L_m l)^3 \quad (5.2)$$

$$E_H = [E_m] L_m^3 u_H \quad (5.3)$$

$$E_R = [E_m] L_m^3 u_R. \quad (5.4)$$

Here $[E_m]$ (J cm^{-3}) is the maximum energy density and L_m (cm) is the maximum structural (volumetric) length, the structural (volumetric) length being denoted with $L = L_m l$. The dynamics of the non-dimensionalized state variables can be deduced from the ones in [39] and are the following:

$$\frac{de}{dt} = \frac{\nu}{L_m l} (f - e) \quad (5.5)$$

$$\frac{dl}{dt} = \begin{cases} \frac{\nu}{3L_m} \frac{e-l}{e+g}, & l < e \\ 0, & \text{else} \end{cases} \quad (5.6)$$

$$\frac{du_H}{dt} = \begin{cases} \frac{\nu}{L_m} (1 - \kappa) e l^2 \frac{l+g}{e+g} - k_J u_H, & u_H < u_H^p \\ 0, & \text{else} \end{cases} \quad (5.7)$$

$$\frac{du_R}{dt} = \begin{cases} 0, & u_H < u_H^p \\ \frac{\nu}{L_m} (1 - \kappa) e l^2 \frac{l+g}{e+g} - k_J u_H^p, & \text{else} \end{cases}, \quad (5.8)$$

where ν (cm d^{-1}) is called the energy conductance, f (dimensionless) denotes the functional food response (see Section 5.3.3 below), and g (dimensionless) is the energy investment ratio.

In DEB theory [39] maximum assimilation rate per surface area, $\{J_{EAm}\}$ ($\text{mmol d}^{-1} \text{cm}^{-2}$), and yield of structure from reserve in growth, y_{VE} (dimensionless), are taken to be primary parameters along with ν , k_J , E_H^p and κ . The relationship of $[E_m]$ and g to these parameters is

$$[E_m] = \frac{\bar{\mu}_E \{J_{EAm}\}}{\nu}, \quad (5.9)$$

and

$$g = \frac{\nu [M_V]}{\kappa \{J_{EAm}\} y_{VE}}, \quad (5.10)$$

where $[M_V]$ (mmol cm^{-3}) is volume specific structural mass and $\bar{\mu}_E$ (J mmol^{-1}) is chemical potential.

We note that we fix the value of E_H^p to 3930 J which is the value used for anchovies [54]. We consider this appropriate here since we are not simulating the whole life cycle of the capelin. We are simulating capelin which we assume to have reached puberty, and thus discrepancies in E_H^p are corrected with the value of k_J . However, E_H^p will be a true parameter of the model once the full life cycle is simulated, and k_J might change accordingly.

We also note that $[E_m]$ is a biological constant characteristic to each

species. Data on the energy density was reported in [1] to be 5866 ± 0.43 (J g^{-1}) for capelin (both sexes combined) in the northern Gulf of Alaska, collected from May through September in 1995 and 1996. We therefore take care choosing the parameters above such that the value of $[E_m]$ is close to that value, which we discuss further in Section 5.5.

The parameters ν and k_J are temperature dependent as will be described in Section 5.2.5. In Table 5.1 we give values of the parameters and constants used in the simulations presented in Section 5.5.

In Section 5.4.1 we discuss the condition on the dynamics of the volumetric length in Equation (5.6). A full description and derivations are in Appendix A.

5.2.4 Roe energy, E_r , and roe production

As stated above, the process of roe production is not a component of the DEB framework. We therefore need to handle the production of roe separately. We introduce a new variable, E_r , which denotes the accumulated energy content of roe. We remember that E_R is the total energy available for roe production, and therefore we expect E_r to depend on that value and not exceed E_R . Below, we use the variable E_r to determine the roe percentage of capelin, see Equation (5.21), as well as Equations (5.17) and (5.19).

We introduce the equation for E_r as follows:

$$\frac{dE_r}{dt} = \gamma(E_R - E_r) \frac{E_r}{[E_m]L_m^3} \quad (5.11)$$

i.e. it increases proportionally to E_r with a proportional coefficient γ (d^{-1}) depending on the difference between E_R and E_r .

Similarly to E_R we non-dimensionalize E_r by setting

$$e_r := \frac{1}{[E_m]L_m^3} E_r, \quad (5.12)$$

which yields the elegant equation

$$\frac{de_r}{dt} = \gamma(u_R - e_r)e_r. \quad (5.13)$$

We note that the parameter γ depends on temperature in the same way as ν and k_J as detailed in Section 5.2.5 below. Also worth mentioning is that we have assumed that the energy invested in roe grows logistically to the asymptote u_R , which is a variable. We do not address here the implications this has on the timing of the actual spawning since we are working with data on capelin before spawning takes place.

5.2.5 Arrhenius temperature

Physiological rates depend on temperature and we use the Arrhenius temperature T_A to express this effect [36]. We assume that all rates are affected in the same way for a species-specific range of temperatures according to

$$p(T) = p(T_r) \exp\left(\frac{T_A}{T_r} - \frac{T_A}{T}\right) \quad (5.14)$$

where T_r (K) is a chosen reference temperature, T_A (K) the species-specific Arrhenius temperature, p the physiological rate (J d^{-1}).

In [20], the relationship between egg development time D (d) and temperature T (K) for the Icelandic capelin (*Mallotus villosus*) was reported to be $\ln(D) = 4.29 - 0.63 \ln((T - 273) + 1)$, derived from experimental data from [21] amongst others. Also, [20] found a near identical relationship by field experiments on beach spawning capelin in Newfoundland.

To estimate the Arrhenius temperature for the Icelandic capelin we

used the data from [21]. Plotting $\ln(1/D)$ against $1/T$ results in a straight line scatter. We obtained $T_A = 9100$ K ($n = 9$, $r^2 = 0.981$), as the slope of the linear regression.

We emphasize that Equation (5.14) applies to a temperature range specific to the species in question. Data from a temperature range which the species experience during their life cycle should be used. The temperature used in [21] ranged from 0°C to 18°C . We have chosen to exclude the last data point, since it is a temperature the capelin do rarely experience, if at all, in the waters around Iceland, and gives a clear outlier to the data.

5.3 Measurements and DEB

DEB theory is the theory of energy uptake and utilization of individuals, but not of whole populations of individuals. In order to truly compare the theory to measurements we would need data on individuals from their whole life cycle. Then we would have growth curves which are faithful to the nature of DEB theory. However, in the case of the capelin, this is not so easy.

Capelin is quite small and far from trivial to locate. Furthermore, tagging individual capelin is quite costly and difficult. When individuals are caught for measuring, it usually means the end of their lives. Samples are usually collected and frozen on board and processed in land.

We have data from the Marine Research Institute of Iceland from as early as 1979 to 2009. The great majority of the spawning stock is 3 and 4 year old capelin, contributing on average 70% and 27%, respectively. The spawning stock of 3 year old is usually divided between females and males in a 3:2 ratio, since the males usually mature at an older age [64].

We use MRI data from the 1999-2000 season because of numerous data available. To be as consistent as possible, we look at mature 3

year old female capelin. The data include location as well as length, wet weight, and weight of reproductive organs. Here, we choose to compare the DEB to the daily averages of these data. In Figures 5.2, 5.3, and 5.4 we show the data on the left and the daily averages on the right.

Additionally, we have measurements from Matis of the fat percentage of capelin, shown in Figure 5.5. These data are different from the MRI data since they are from commercial capelin catches, where samples were collected and processed on land. We do therefore not have any location associated with these data. We however believe, that these data represent the same schools of fish as the MRI measurements sampled during their research expeditions, and are therefore comparable.

5.3.1 Daily averages from the 1999-2000 season

About 100 individual capelin were caught on each of 56 different days, resulting in a total of 5596 measured capelin. Figure 5.6(a) shows the location of the capelin measurements from research expeditions of the MRI during the 1999-2000 season. We discuss in Section 5.3.2 how we estimate the temperature at those locations using the oceanographic model CODE [43]. In Chapter 6 we show both maps of temperature and currents from that model and discuss differences to the data previously used. We show in Figures 6.3 and 6.4 a comparison between measured temperature and output from the model.

5.3.2 Temperature estimates for the 1999-2000 season

As equations governing metabolic rates are dependent on temperature, see Equation (5.14), we need to estimate the temperature the capelin experienced in the 1999-2000 season. In Figure 5.6(a) we see the location of the capelin measurements in the 1999-2000 season. Figure

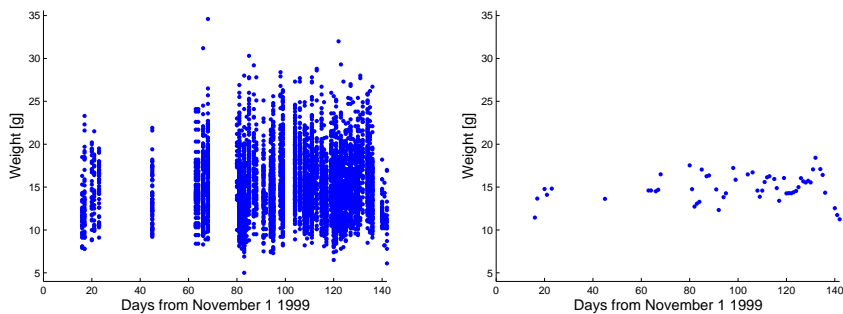


Figure 5.2: Data from the MRI. Left: Distribution of the weight of 3 year old capelin in the 1999-2000 season. Right: Day averages of same data.

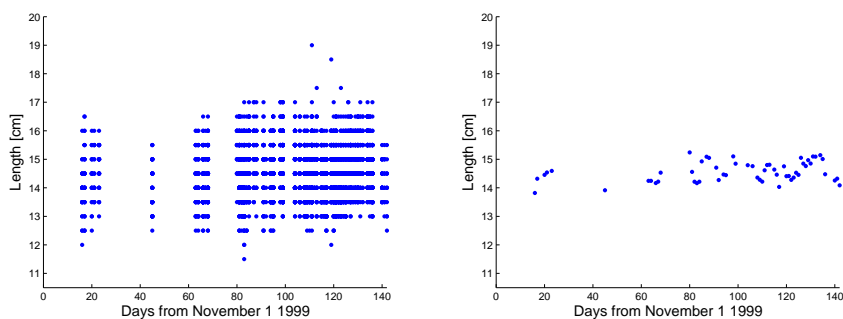


Figure 5.3: Data from the MRI. Left: Distribution of the length of 3 year old capelin in the 1999-2000 season. Right: Day averages of same data.

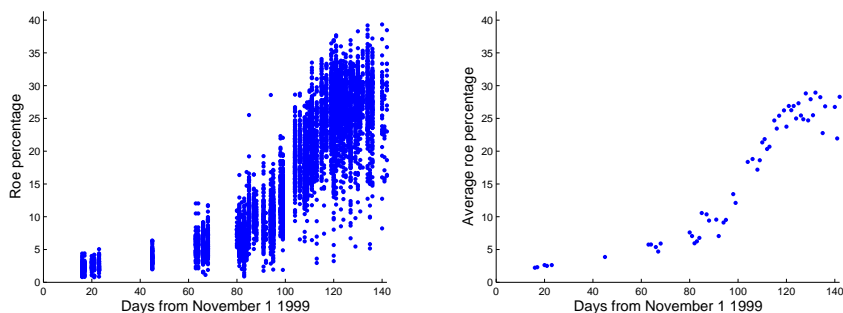


Figure 5.4: Data from the MRI. Left: Distribution of the roe percentage of 3 year old capelin in the 1999-2000 season. Right: Day averages of same data.

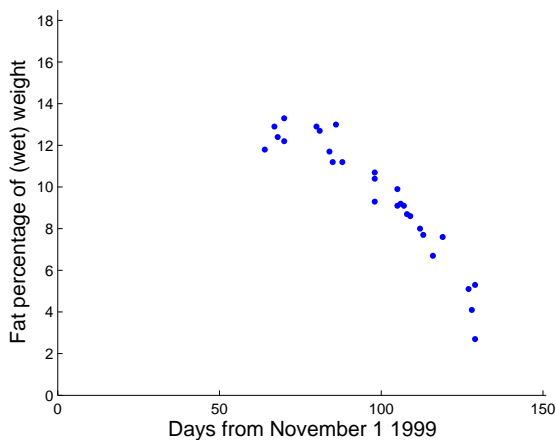


Figure 5.5: Day averages of the fat percentage of capelin catches in the 1999-2000 season. Data from Matis.

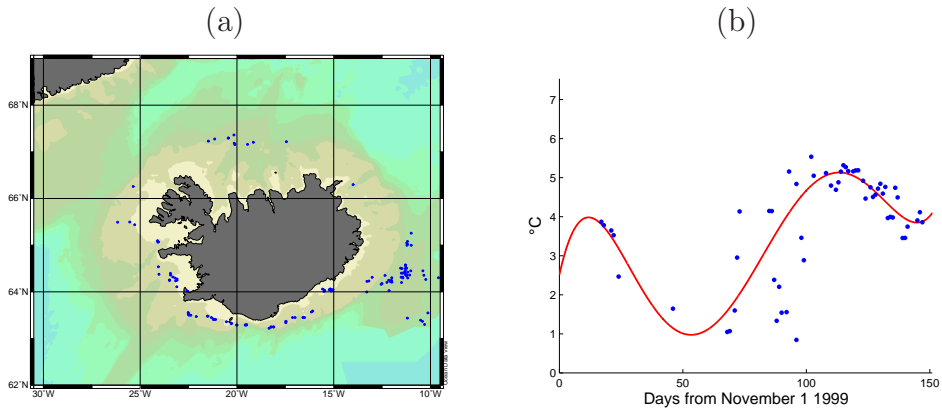


Figure 5.6: (a) Location of measurements on 3 year old spawning capelin from the Marine Research Institute during the 1999-2000 season. (b) Estimated temperature (blue dots) from locations of measurements on capelin in 1999-2000 along with the temperature which was used for the DEB simulations (red curve).

5.6(a) was created in Ocean Data View (Schlitzer, R., Ocean Data View, <http://odv.awi.de>, 2010). Using temperature data from the CODE model [43], we estimate the temperature at 45m depth for each individual measured capelin. In Figure 5.6(b) we show the daily averages of these estimates as (blue) dots. We fit a quintic polynomial through these estimates, shown as a (red) curve, which will be the temperature we use in the simulations of Equations (5.5)-(5.8), and (5.13). We believe that by doing so we have a fairly accurate and the best available estimate of the temperature the schools of capelin experienced.

5.3.3 Food availability

Food availability in the cold seas around Iceland in fall and winter is low compared to the plankton-rich areas north of Iceland. During the spawning migration, mature capelin have been observed to feed only when they

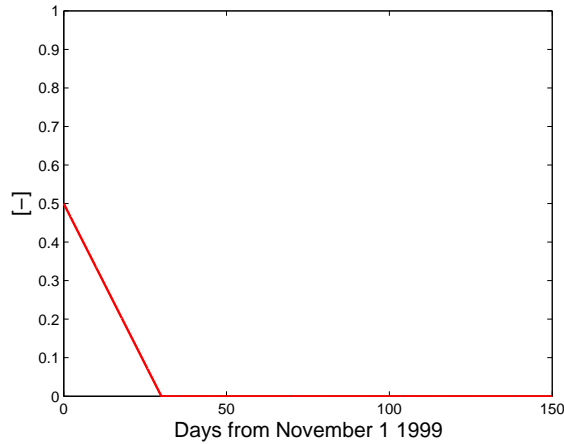


Figure 5.7: Food availability and utilization used in Equation (5.5).

encounter food, but not to actively seek it out [64]. Measurements are rare and hard to acquire and we therefore choose the simple form for the function for functional food response, f , in Equation (5.5), shown in Figure 5.7.

5.4 DEB and observed quantities

As stated before, the state variables of the DEB model are not directly observable. Rather, the observable variables are weight, length, fat content and roe content. In turn, the state variables have to be obtained from these measurable quantities as we detail here below.

5.4.1 Physical length

Around the time of the spawning migration the physical length of the capelin is close to being constant, see Figure 5.4. We therefore add the

condition to Equation (5.6):

$$\frac{dl}{dt} = 0, \quad \text{if } e \leq l, \quad (5.15)$$

which prevents negative growth. This was also done in the case of the anchovy [56].

In order to link the volumetric length, $L = V^{1/3}$, to the actual length of the capelin, \mathfrak{L} , we treat the capelin as an isomorph [36] after it develops from the larvae stage, and estimate the shape coefficient, δ , such that

$$\mathfrak{L} = \frac{1}{\delta} L. \quad (5.16)$$

We have assumed that the immature capelin have no reproduction reserves, and neglected the contribution of the reserves to the total weight. The latter assumption is justified by the fact that capelin do hardly feed much or at all during the winter [64]. We obtained an approximate value $\delta = 0.161$ ($n = 22, p < 0.001$) by fitting a weight-length relationship of the type $\mathfrak{W} = (\delta \mathfrak{L})^3$ to immature capelin measured in January-February [64]. The value of the shape coefficient for capelin is similar to the shape coefficient 0.172 found for anchovy, reported in [56].

5.4.2 Physical weight

Physical weight, \mathfrak{W} , has contributions from structure, the energy reserves, the reproduction energy and roe. These are general compounds, which are rich in lipids, which are mostly stored in the muscle, but also contain e.g. protein. We assume that the reserve energy and reproduction energy have the same composition and thus the same energy content.

The roe has a different energy content than the reserves, and thus the weight of roe needs to be treated separately from the fat content. It is characteristic to capelin to convert almost all of its available fat

content into roe, and we thus subtract the energy already converted into roe from fat.

$$\mathfrak{W} = d_V V + \frac{E + E_R - E_r}{\rho_E} + \frac{E_r}{\rho_r} \quad (5.17)$$

where the constant d_V (g cm^{-3}) denotes the density of the structural volume, ρ_E (J g^{-1}) denotes the energy content of one gram of reserve, and ρ_r (J g^{-1}) denotes the energy content of one gram of roe. This representation of physical weight is found in a similar way as in [38].

5.4.3 Fat and roe content

Lipid content (in dry mass) is the primary determinant of energy density [1], and since the capelin store most of their energy as lipids in their muscle, we let $\rho_E = 39.3$ (kJ g^{-1}), which is the energy content of lipids reported in [1]. We do not have a measured value of ρ_r and therefore find a plausible value for the simulations. We find a value for ρ_r which is lower than ρ_E , as expected, since the roe have considerable more water. The water content of roe has to be taken into account, which we detail in Section 5.4.4.

We let the fat content of individuals be determined by

$$W_{fat} = \frac{E + E_R - E_r}{\rho_E}. \quad (5.18)$$

and the weight of roe by

$$W_{roe} = \frac{E_r}{\rho_r}. \quad (5.19)$$

We denote by F the percentage of fat of the total body weight, i.e.

$$F = 100 * \frac{W_{fat}}{\mathfrak{W}}, \quad (5.20)$$

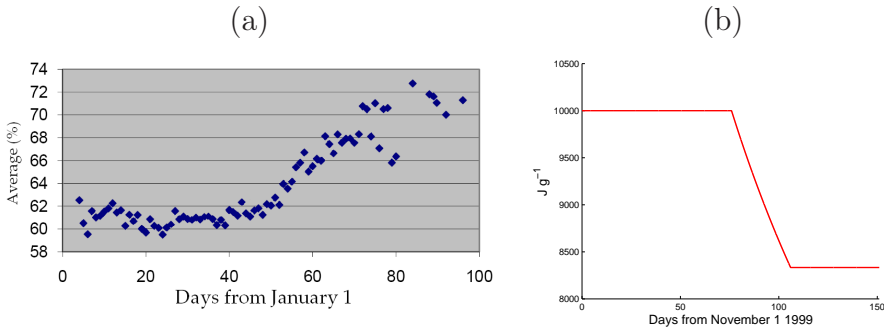


Figure 5.8: (a) Water content of capelin roe. Averages from 1984-2009. Data from Matis [22] (b) The parameter ρ_r , see equations (5.17) and (5.19). It assumes an increase of the water content of roe of 20% in about one month.

and also by R the percentage of the roe of the total body weight, i.e.

$$R = 100 * \frac{W_{roe}}{\mathfrak{M}}. \quad (5.21)$$

We plot the output of the Equations (5.16), (5.17), (5.20), and (5.21) in Figure 5.9 and describe the fit to data in Section 5.5.

5.4.4 Water content of roe

We note that the energy content of roe is low compared to the energy content of the energy reserves. Data from Matis show how the water content of capelin roe increases as the roe matures, and becomes the best measure on roe maturity once the roe percentage exceeds 20% [22]. In Figure 5.8(a) we show data from Matis and in Figure 5.8(b) we show how we take the water content into account by changing the value of ρ_r over time. The change in ρ_r corresponds to a 20% increase of water content of the roe over a period of one month.

5.5 Results

We now simulate the Equations (5.5)-(5.13) using a fourth order Runge-Kutta method with the parameter values as described in Table 5.1, the first six parameters being primary DEB parameters. The results are described below and a comparison between measurements and theory can be seen in Figures 5.9(a)-(d).

We plot in Figure 5.9(a), (c), and (d) the following derived quantities: weight, \mathfrak{W} , fat percentage, F , and roe percentage, R , from Equations (5.17), (5.20), and (5.21), respectively. Figure 5.9(b) shows the physical length from Equation (5.16). The (blue) dots in Figure 5.9 represents the data.

Firstly, we look at Figure 5.9(a) of the weight. The data from the MRI are shown as (blue) dots and the derived physical weight \mathfrak{W} from Equation (5.17) as a (red) solid curve in the Figure. We obtain a weight which is higher than measurements, but the difference is relatively small. Note that the derived weight increases as the individual comes closer to spawning. We notice that the scatter of the data does not seem to render this increase in weight implausible. We are plotting wet weight in both cases, and thus this increase can be explained by the water content of roe increasing, as discussed in Section 5.4.4.

We show in Figure 5.9(b) the measured length of the capelin and the DEB simulations of the length in Equation (5.16). We see that the simulated length is very similar to the measured one, but note that the simulations are sensitive to the shape coefficient δ in Equation (5.16). Because the shape coefficient is only a parameter in the model it indirectly affects the simulations. A smaller value of δ would increase the length, but other parameters would have to be changed to get similar results.

Figure 5.9(c) shows the fat percentage from data from Matis as (blue)

Table 5.1: Values of parameters and constants.

κ	0.4	-	Fraction of energy to somatic growth and maintenance ³
ν	0.02	cm d ⁻¹	Energy conductance ³
$\{J_{EA_m}\}$	0.23	mmol d ⁻¹ cm ⁻²	Maximum assimilation rate per surface area ³
y_{VE}	0.8	-	yield of structure from reserve growth ⁶
k_J	0.001	d ⁻¹	fraction of maturity maintenance ²
E_H^p	3.93	J	Maturity energy at puberty ⁷
γ	0.20	d ⁻¹	Growth rate of roe ³
T_A	9100	K	Arrhenius temperature ¹
T_r	6.5 + 273	K	Reference temperature ²
$[M_V]$	4.4	mmol cm ⁻³	Volume specific structural mass ³
$\bar{\mu}_E$	500	J mmol ⁻³	Chemical potential ⁷
δ	0.161	-	Shape coefficient ¹
L_m	2.82	cm	Maximum structural (volumetric) length ¹
d_V	1	g cm ⁻³	Density of structural volume ⁴
ρ_E	39.30	kJ g ⁻¹	Energy reserve density ⁵
ρ_R	10.00-8.33	kJ g ⁻¹	Energy density of roe (see Figure 5.8(b)) ³

1) Estimated from data

2) Chosen

3) Calibrated to data

4) From [62]

5) From [1]

6) From [55]

7) From [54]

dots. The DEB simulations of the derived quantity F from Equation (5.20) is shown as a (red) solid curve. The fit is reasonably good, although the data suggest a sharper drop in the fat percentage, which could be explained by the roe production not fully reaching its maximum fast enough close to spawning, as described below.

Finally, and most importantly, Figure 5.9(d) shows the roe percentage from data from MRI as (blue) dots. Here we clearly see the sharp increase in roe production of the capelin once they start maturing. The DEB simulations of the roe percentage R is shown as a (red) solid curve. The DEB theory gives a good fit, with the main discrepancies towards the end of the migration. The maximum roe percentage eventually reaches values similar to measurements, but the data suggests an even faster increase of roe production. On the other hand, most notably we see that the sharp increase of roe production starts at the same time as the measured one. This will allow us to use the DEB theory to model behavioral triggers in the interacting particle model in [3], which we discuss further in Chapter 6.

Finally, we calculate the values of several derived quantities which the parameter values in Table 5.1 give. First, the value of g , the energy investment ratio from Equation 5.10, becomes

$$g = \frac{\nu[M_V]}{\kappa\{J_{EAm}\}y_{VE}} = 1.20, \quad (5.22)$$

which for anchovies was reported as 6 [56]. The value of $[E_m]$, the maximum energy density from Equation 5.9 turns out to be

$$[E_m] = \frac{\bar{\mu}_E\{J_{EAm}\}}{\nu} = 5750, \quad (5.23)$$

where $\{J_{EAm}\}$ was chosen so that $[E_m]$ would have a similar value to the one given in [1], where a value of 5860 J cm^{-3} is reported. Similarly,

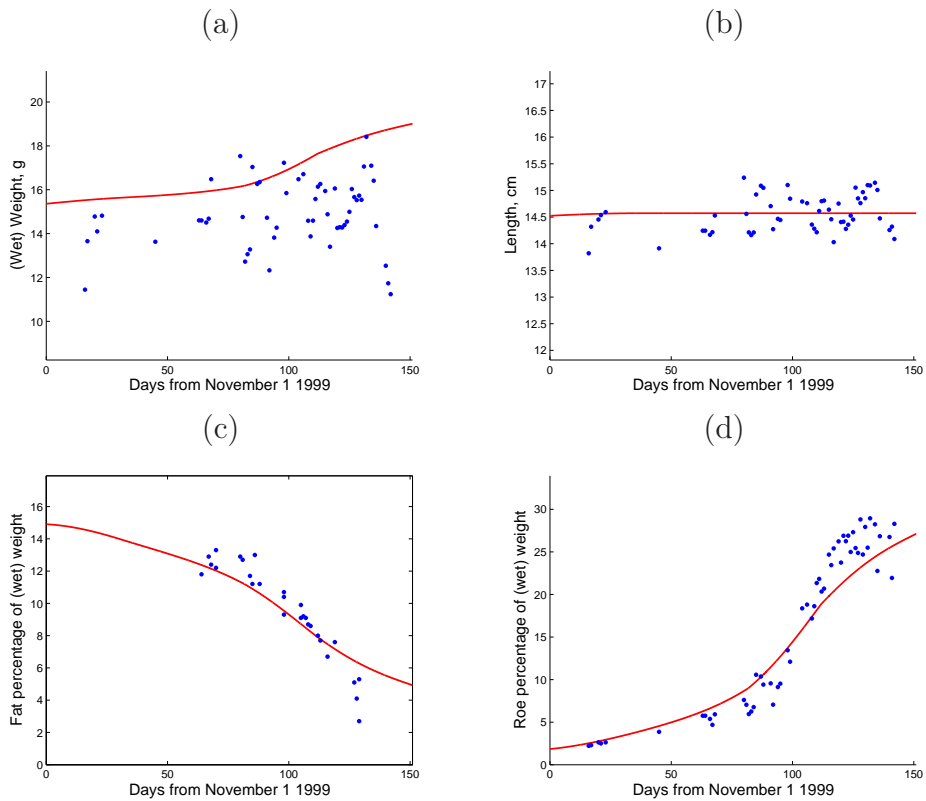


Figure 5.9: Comparison between measurements of 3 year old mature female capelin during the 1999-2000 season (blue dots) and the DEB model (red curves), see equations (5.16)-(5.21). (a) Weight, (b) Length, (c) Fat percentage, (d) Roe percentage.

we get the value of $[E_G]$ (J cm^{-3}), which is the volume specific cost of growth, as the following

$$[E_G] = \frac{\bar{\mu}_E[M_V]}{y_{VE}} = 2750, \quad (5.24)$$

where $[M_V]$ was chosen so that the value of $[E_G]$ is similar to the value 2800 for anchovies [54]. The volume specific somatic maintenance rate, $[p_M]$ ($\text{J d}^{-1} \text{cm}^{-3}$), can be calculated from Equation A.13, with $\{p_{Am}\} = \bar{\mu}_E\{J_{EAm}\}$, as follows

$$[p_M] = \frac{\kappa\bar{\mu}_E\{J_{EAm}\}}{L_m} = 16.3 \quad (5.25)$$

where [54] gives the value 19.0 for anchovies. The maximum structural volumetric length of the capelin was chosen so that the maximum physical length of capelin, according to Equation (5.16) with $L = L_m$, would be 17.5 cm, which was estimated from the data from the MRI.

5.6 Discussion

With the DEB model, we now have a good model for the growth and energy use of the Icelandic capelin. The model successfully reproduces the length, weight, fat content and roe content of mature capelin. Most importantly, it captures the timing of the accelerated roe production, which we can then use as an internal trigger in a migration model. We show in Chapter 6 how these results will be integrated into the interacting particle model of Part I. Most notably, both the speed and the preferred temperature range will be determined by the stage of the maturity of each individual, see Sections 6.1 and 6.2, respectively.

It also is also of interest to note that the DEB depends on oceanic temperature. With the DEB model we can now directly model how changes

in temperature affect both the timing and the route of the migration. This gives us another tool to understand and predict how changes in water temperature can affect the migrations of capelin.

5.6.1 Low value of κ

We note that the value of κ , or the fraction of utilized energy each individual spends on somatic growth and maintenance, which was calibrated to be 0.4, is quite low compared to other species of fish. For example, in [62] the value of κ is given for four different species of flatfish; plaice *Pleuronectes platessa* (L.), flounder *Platichthys flesus* (L.), dab *Limanda limanda* (L.), and sole *Solea solea* (L.). The values given for these species is 0.85, 0.65, 0.85, and 0.9, respectively. If we compare to anchovy, the value $\kappa = 0.65$ is found in [56]. However, the anchovy can spawn up to twenty times per season [50], whereas capelin spawns only once.

The spawning behavior of capelin is quite dramatic in the sense that once it has decided to spawn it puts nearly all its efforts into roe production. After spawning the spawning stock dies. This strong requirement for success probably explains the low value of κ . It is possible that during the earlier life stages of the capelin this value is higher, which is reminiscent of the „bang-bang“ strategy for organisms, e.g. [9]. In future work, when the whole life cycle of the capelin is modeled, it will be interesting to see whether this is the case so that the DEB model needs to be modified, or a single value for κ will suffice.

5.6.2 Scatter in data plots

In Figures 5.9 (a)-(d) of the data from the MRI and Matis we note that there is considerable scattering. The plots show average values of all caught fish each day, from various locations. When investigating the data set we find that the locations (i.e. the data points) are mostly close

to each other, both spatially and temporally, but discrepancies in the measurements could explain some of the scattering.

We also note that we do not have the history of the whole life cycles of each individual, but rather we have samples from schools of fish. Some of the scatter could be explained by measurements being taken from individuals who experienced different conditions during their life. It would be optimal, and true to the essence of DEB theory, to follow individuals and measure them several times on their migration, if this were possible. We have however, samples of capelin which experienced similar conditions and therefore hopefully give a reasonable representation of a typical life cycle of the capelin.

6

A model for the spawning migration of capelin

In Part I we presented a model for the spawning migration for the Icelandic capelin. Simulations were carried out and the spawning migration of the capelin was reproduced for three different years in [3]. However, that model uses no maturity cues, which observations clearly indicate play an important part [64, 65]. Combined with the DEB model of part II, we can now take into account the maturity of each individual [18].

We have presented a DEB model for the growth, energy utilization and reproduction for mature female capelin. Good fits of parameter values were found for the 1999-2000 season based on a large data set of 5596 individual 3 year old females. The most important contribution of the DEB model to the interacting particle model is the timing of the onset of increased roe production. With the DEB model we are now in a position to let the sexual maturity of individuals act as triggers for changes in their behavior.

Below we incorporate the DEB model of the capelin's inner dynamics into the interacting particle model of part I. Effects of maturation on

the particles' speeds were modeled indirectly in part I by increasing their speed once they passed a certain geographical location. In Section 6.1 we describe how changes in the speeds of individual particles can be linked directly to changes in maturity, and in Section 6.2 we describe how the preferred temperature range can be linked to maturity. In both cases maturity will be measured in terms of the roe content of the individual particle.

6.1 Speed and preferred speed

As mentioned before, the speed of a migrating capelin is dependent on its stage of maturity [64]. Once a certain roe percentage is reached, the capelin increase their speed and head into warmer water. We want to model this behavioral trigger and use the DEB for that end.

In part I [3] particles also have a preferred speed depending on how close they are to spawning, although the actual speed also depends on the average speed of certain neighboring particles. As mentioned in Section 3.2.2, this preferred speed is somewhat crudely modeled by starting to increase it when the particles have reached a geographical location, east of longitude 13.5°W. By integrating the DEB model into the particle model it is possible to let the preferred speed depend on the roe content.

In Equation (2.1) the speed v_k was updated as the average of the speed of its neighbors within the zone of orientation. We now rename that average speed as

$$v_{k,N}(t) = \frac{1}{|O_k|} \sum_{j \in O_k} v_j(t). \quad (6.1)$$

However, we now want to take into account the roe percentage of each individual, because the capelin have been noticed to vary their speed depending on the roe percentage. We therefore let $R_k(t)$ denote the roe

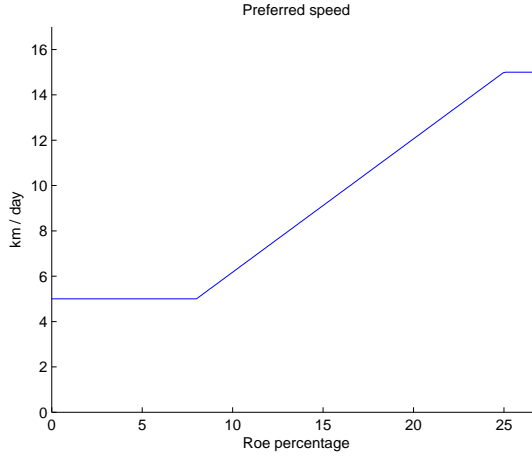


Figure 6.1: The proposed preferred speed, v_p , from Equation (6.2), as determined by the roe content. We let the roe content $R^m = 9\%$ determine when the speed starts to increase. We assume a linear increase of 15 km/day until a roe percentage of 25% has been reached.

percentage of individual k at time t , see Equation (5.21). Additionally, we let v_p denote a preferred speed of capelin, as a function of its roe percentage, R_k . In Figure 6.1 we show the proposed preferred speed as a function of the roe content.

Similarly to Equation (2.10) we propose a new rule for updating the speed of each particle as

$$v_k(t + \Delta t) = (1 - \alpha)v_{k,N}(t) + \alpha v_p(R_k(t)). \quad (6.2)$$

We refer to the factor α as the preferred speed weight factor. Similarly to Equation (2.11) we rewrite Equation (6.2) as

$$v_k(t + \Delta t) = v_{k,N}(t) + \alpha (v_p(R_k(t)) - v_{k,N}(t)). \quad (6.3)$$

The second term of the right hand side of Equation (6.3) is proportional

to α and the difference between the preferred speed and the average speed of the neighbors. The parameter α does therefore determine how much a particle adjusts its speed to the preferred speed at each time step. The weight factors β and α are therefore quite similar, both determining how an individual particle adjusts its interacting behavior to that of the environment and its roe content, respectively.

6.1.1 Speed of a particle during the 1999-2000 season

We use the DEB model, as described in Chapter 5, to obtain the roe percentage, R , as defined in Equation (5.21), of an individual particle. We use the roe percentage shown in Figure 5.9(d) for the 1999-2000 season. We show the evolution of the speed as defined in Equation (6.2) in Figure 6.2 with two different values of α . We note that the increase of speed starts when the roe percentage, R , has exceeded 9%.

As we see in Figure 5.9(d), and in Figure 6.2, the roe exceeds the 9% percentage mark in just under 82 days after November 1 1999, which corresponds to about January 22 2000. This timing is quite close to the actual time at which the capelin reached the high temperature gradients off the south east coast of Iceland. A percentage mark of 8% would mean that the trigger would be set at 76 days after November 1 1999, corresponding to January 17 2000. Were we to increase the percentage mark to 10% roe content, the percentage mark would be reached in 87 days, corresponding to January 27 2000. We therefore see that the percentage mark of 8-10% results in the required roe content being reached from between January 17 and January 27 of 2000.

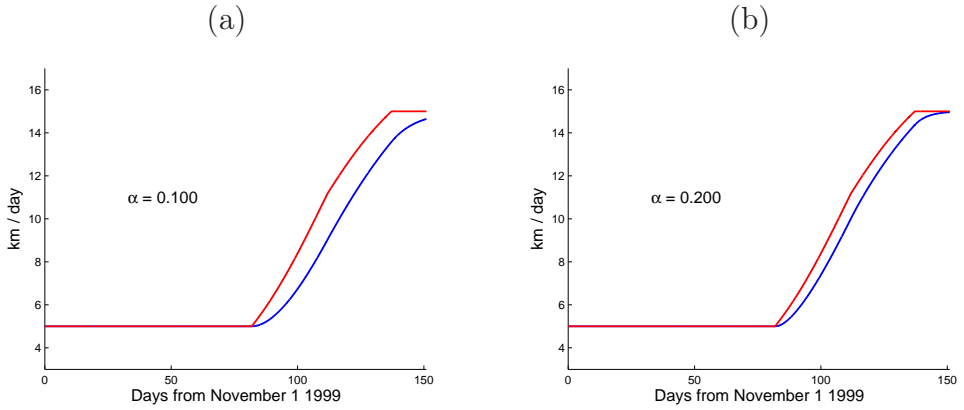


Figure 6.2: The red curve is the preferred speed v_p of a particle with the roe percentage calculated as described in Chapter 5, shown in Figure 5.9(d). The blue curve is the resulting speed from Equation (6.2). The percentage mark, used as a trigger for increasing the speed in the preferred speed v_p , is in both figures 9%. The preferred speed weight factor is (a) $\alpha = 0.01$, (b) $\alpha = 0.02$.

6.1.2 Reaction time τ_R

Now with the speed being updated as in Equation (2.1) we see that individuals would adjust their speed to that of their neighbors in one time step. That means that the time step should be interpreted as the capelin's reaction time to its neighbors, τ_N . In Section 2.5 we introduced a reaction time to the temperature, τ_T , and discussed how those two reaction times related to the temperature weight factor, β . We now introduce yet another reaction time, τ_R , denoting the time it takes the individual to react to changes to its roe content.

Similarly to Equation (2.13) we look at the following differential equation determining the change of particle k 's speed, $\tilde{v}_k(t)$:

$$\frac{d}{dt}\tilde{v}_k(t) = \frac{1}{\tau_N}(v_{k,N}(t) - \tilde{v}_k(t)) + \frac{1}{\tau_R}(v_p(R_k(t)) - \tilde{v}_k(t)). \quad (6.4)$$

Discretizing this equation results in

$$\tilde{v}_k(t + \Delta t) = \tilde{v}_k(t) + \frac{\Delta t}{\tau_N} (v_{k,N}(t) - \tilde{v}_k(t)) + \frac{\Delta t}{\tau_R} (v_p(R_k(t)) - \tilde{v}_k(t)). \quad (6.5)$$

We obtain Equation (6.4) by choosing $\Delta t = \tau_N \tau_R / (\tau_N + \tau_R)$, and thus α has the same form as β in (2.17), with τ_T substituted for τ_R . Now, choosing $\Delta t = \tau_N$ we get

$$\tilde{v}_k(t + \Delta t) = v_{k,N}(t) + \frac{\tau_N}{\tau_R} (v_p(R_k)(t) - \tilde{v}_k(t)), \quad (6.6)$$

which is again similar to Equation (6.3) with $\alpha = \frac{\tau_N}{\tau_R}$.

We see that if $\tau_R > \tau_N$ then with either choice of the time step we obtain $\alpha \in [0, 1]$. With similar arguments as in Section 2.5, we claim that it is indeed the case that the reaction time to roe content is longer than the reaction time to neighbors. It might, however, be hard to measure such a quantity, and we therefore leave the exact form of α to be decided from simulations.

6.2 Preferred temperature range

In [3], the individual particles have a preferred temperature range which they seek out. As mentioned in the Introduction, Section 1.3, the capelin have a tendency to time their entry into warmer waters when their roe percentage has exceeded 8-10%.

We therefore model this behavior by letting the preferred temperature range depend on the roe percentage. We let R^m denote the required percentage mark in order to change the preferred temperature range, $[T_1, T_2]$. The DEB model of Chapter 5 will therefore determine this change of temperature preference.

Now, we let $[T_1^p, T_2^p]$ denote the preferred temperature range of mi-

grating capelin which have not reached a roe content of R^m , and $[T_1^m, T_2^m]$ the preferred temperature range once the fish are sufficiently mature. The lower and upper bound of the preferred temperature range will therefore depend on the roe content, R , in the following way:

$$T_i(R) = \begin{cases} T_i^p & \text{if } R < R^m, \\ T_i^m & \text{if } R \geq R^m, \end{cases} \quad (6.7)$$

where $i \in \{1, 2\}$.

Now, in Section 6.1.1 we noted that the percentage mark of 9% was reached at January 27 2000. With a percentage mark of 8-10% the required roe content is reached from between January 17 and January 27 of 2000. The effect this will have on the simulations is that if particles reach the warm waters off the south east coast of Iceland before they are mature enough, they should react to the warm water gradients and be reluctant to enter the warm waters.

6.3 New maps of currents

In Section 5.3.2 we described how we used the temperature from an oceanographic model [43] for temperature around Iceland during the 1999-2000 season for the DEB simulations of Chapter 5. We show in Figures 6.3 and 6.4 a comparison between measured temperature and output from the model from two different time periods.

We have noted that the currents used in Chapter 3, shown in Figure 3.2, are a constant approximation to currents around Iceland. With data from the oceanographic model of Dr. Kai Logemann [43] we can now use dynamic currents. We show in Figure 6.5 currents from different days, corresponding to the ones in Figures 6.3 and 6.4. We discuss the difference between the different temperature and currents data below.

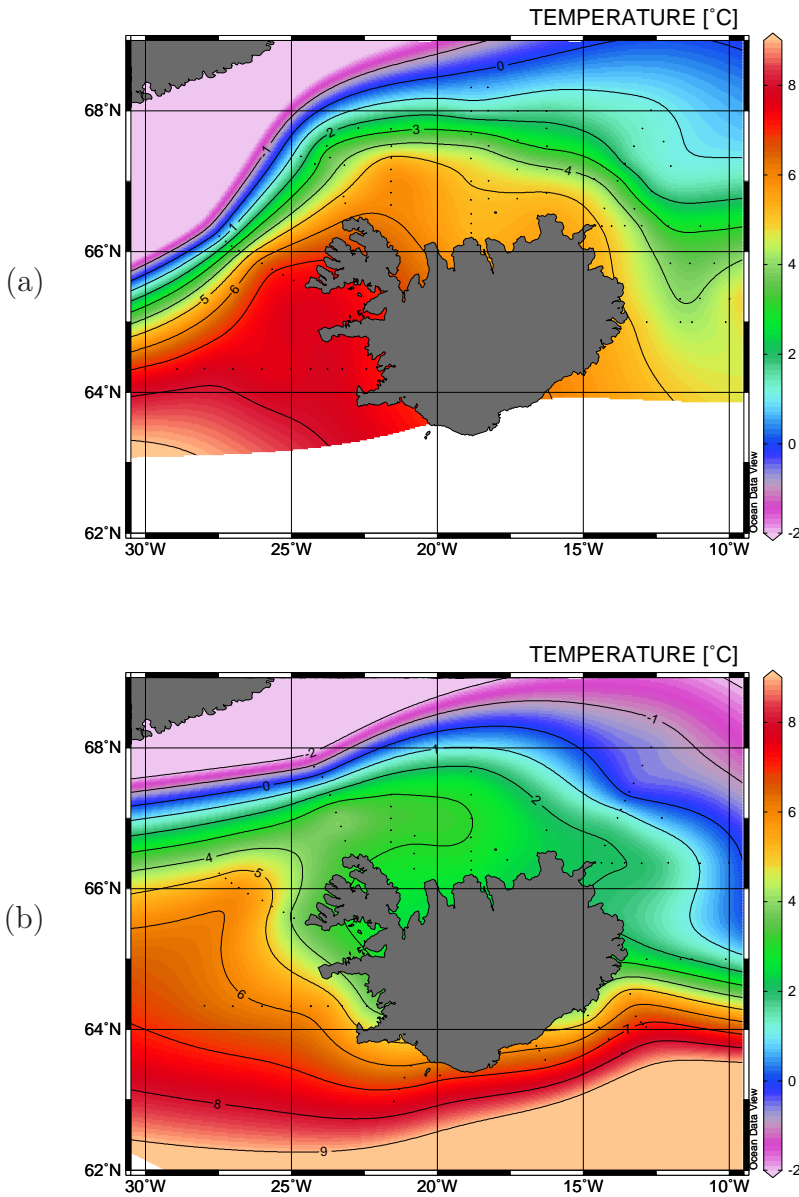


Figure 6.3: Interpolated data on sea temperature at 50m depth from the Marine Research Institute. Measurement sites are shown as black dots. Data from (a) November 11 to December 4 1999. The lower part is white due to lack of data. (b) February 16 to March 3 2000.

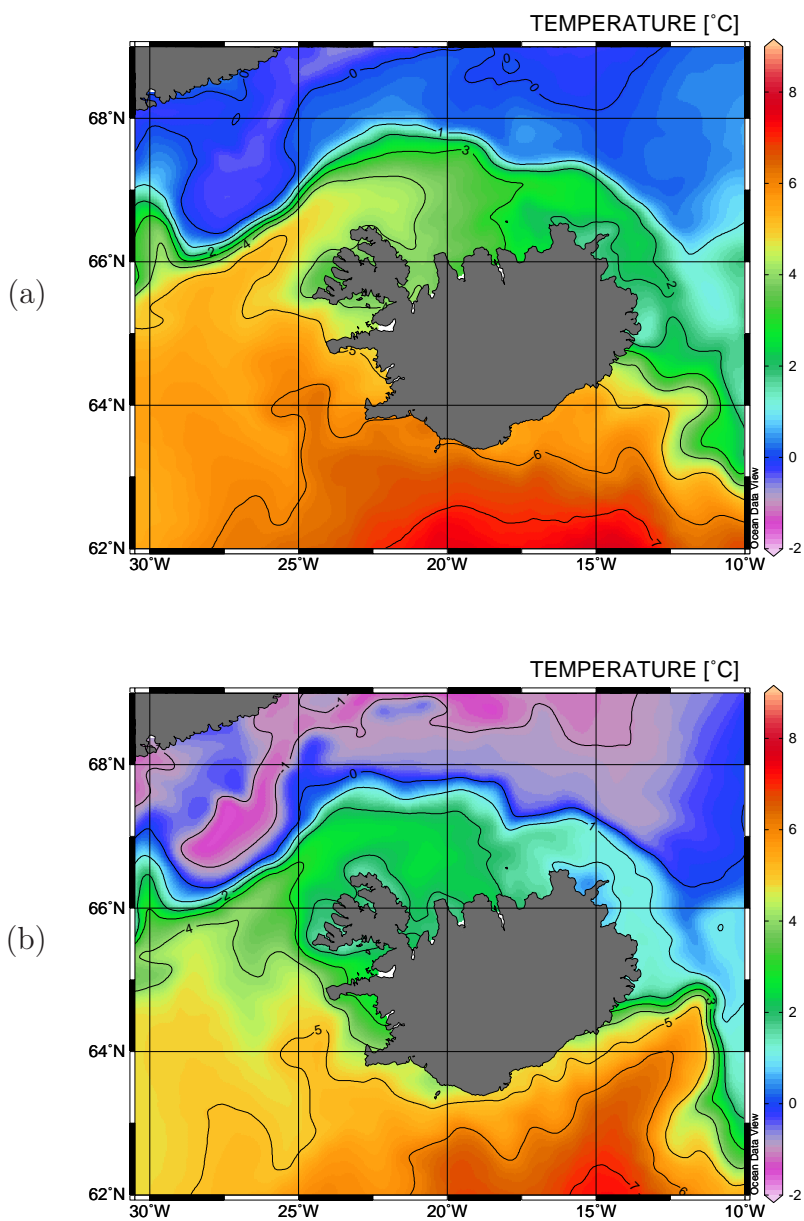


Figure 6.4: Sea temperature at 45m depth from the model of Dr. Kai Logemann [43]. Data from (a) November 11 to December 4 1999, (b) February 16 to March 3 2000.

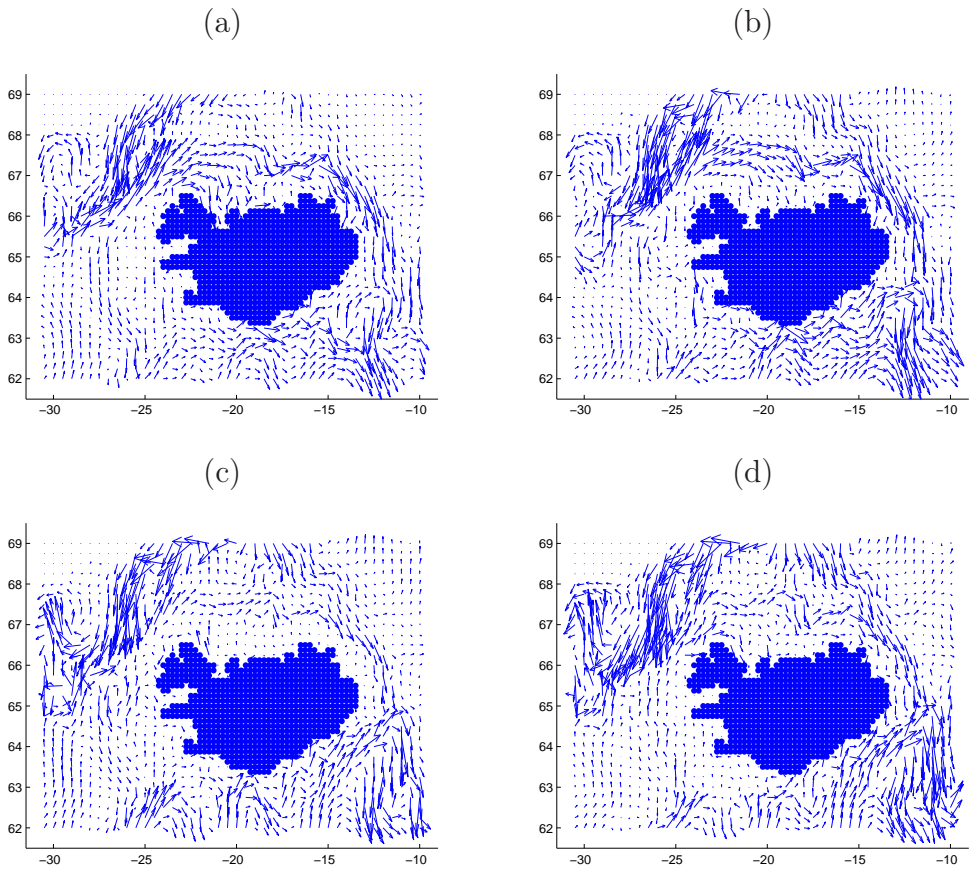


Figure 6.5: Simulated currents from an oceanographic model [43]. The strength of the current is given by the length of the line segments. Compare to Figure 3.2. (a) November 11 1999, (b) December 4 1999, (c) February 16 2000, and (d) March 3 2000.

6.4 Discussion

Above, we have only simulated the inner dynamics of only one particle, thus not taking into account the interactions of particles. Figure 6.2 was obtained from the DEB model of Chapter 5 with one particle, and we note that simulating with thousands of particles could result in a lower value of α being required to yield a realistic simulation.

We note that we have defined two different preferred temperature ranges, one for mature capelin not yet ready to enter warm waters, $[T_1^p, T_2^p]$, and another range for capelin whose roe content had surpassed a certain trigger R^m , $[T_1^m, T_2^m]$. It is possible to define yet another preferred temperature range, $[T_1^l, T_2^l]$, for capelin past the larvae stage which have not reached puberty, to be used once the whole life cycle of the capelin is modeled and simulated. This preferred temperature range would be determined by the maturity energy E_H having reached the threshold E_H^p , thus marking the onset of puberty, as described in Section 5.2.2. In this way we can fully determine the capelin's temperature preferences and could use the threshold E_H^p as a trigger for the capelin starting their feeding migration.

We now compare the measured temperature from the MRI, Figure 6.3, to the output of the data of Kai Logemann 6.4. Both Figure 6.3(a) and Figure 6.4(a) show temperature from November 11 to December 4. We note that the measured temperature shows warmer water reaching to the north west of Iceland, which could have the effect of pushing particles east and preventing them to take a western route to the spawning grounds. Figure 6.3(b) and Figure 6.4(b) show temperature from February 16 to March 3. Although the temperature from Logemann's model is not as high as the measured one, we clearly see more detailed temperature. Most importantly, off the south east coast we see the shape of the "tongue" of warm water extending to the east coast. This detail is not well captured

with sparse measurements, and will be interesting to incorporate into the simulations. The particles will show different behavior depending on where they encounter this tongue, as particles hitting the west part of the tongue will swim towards Iceland, while others might get pushed further east, as far as the Faroe Islands [66].

We compare the new currents in Figure 6.5 to the ones shown in 3.2. Off the north and northeast coast of Iceland, the currents run clockwise around Iceland. The main difference is that the currents off the south and southeast coast are counter clockwise, whereas the older currents were clockwise all around Iceland. The currents in Figure 6.5 are thus in the opposite direction to that of the migrating capelin. This is clearly of importance in the simulations, since the particles will not be aided in the same way by the currents to reach the spawning grounds off the southwest coast of Iceland.

The DEB model will further help to explain variations in migration patterns based on environmental factors. In particular, the DEB equations depend on oceanic temperature which allows us to determine the effect the environment has on the migration routes of the capelin, and thus predict what effect changes in the oceanic temperature will have on the behavior of the capelin.

Although DEB theory deals with individuals, and not populations as a whole, we hope that by combining the DEB model with the interacting particle model in [3] it will be possible to further explain phenomena of large schools of fish by the physiology of individual fish, resulting in a powerful model of the spawning migration of the Icelandic capelin and hopefully the migrations of other species of fish as well.

7

Conclusions

Interacting particle models are fascinating to work with, because relatively simple social rules, or interaction rules, create very interesting patterns. It is especially interesting to observe that the emerging patterns are similar to patterns observed in nature. By investigating and analyzing the behavior of such models, we come closer to understanding dynamics of animal movements. Differences between species could then be characterized by different parameter values or other behavioral rules.

Here, we have applied a two dimensional interacting particle model to the Icelandic capelin. We have integrated environmental fields into the model and modeled the fish's reaction to temperature. The success of such a biologically simple model is quite significant.

With the DEB model of Part I we are now in a position to further build on the migration model, by incorporating the effects of roe percentage on the migration. We hope that further development of the integrated models will ultimately lead to a powerful model, able to predict the migration route of the capelin.

We note that the model of Part I is limited to two spatial dimensions. Although the capelin is a pelagic fish, they have been reported to swim

to depths of several hundred meters. Even though violent storms in the winter cause mixing in the top layers of the ocean, the capelin could react to temperature variations at greater depths. Currents also vary with depth, and it is possible that capelin avoid strong currents by swimming into calmer waters at a depth. Lastly, recent advances in computational powers will make it a feasible task to include the computationally expensive third spatial dimension.

So far, limited data and computational resources have mostly determined the models' level of complexity. However, we note that the oceanographic model of Logemann [43] could provide sufficiently accurate data which previously has been unavailable. It is a model for currents, temperature and salinity, and is the first of its kind to be specifically developed for the waters around Iceland.

We are currently only modeling the spawning migration of the Icelandic capelin. But as mentioned in Section 1.3, the pubescent capelin undertake an equally extensive migration to the plankton-rich waters of the Iceland Sea as far north as the island of Jan Mayen. It would be of theoretical as well as practical interest, and adding a sense of completeness to the project, to model the full life cycle of the capelin, as has been done for the anchovies [56]. Such is indeed the long term goal, but scarcity of data has so far made the task impractical. However, the DEB model already addresses the dynamics of the whole life cycle of individuals. We have only focused on the spawning migration and therefore left open questions regarding the previous life stages. But a DEB model for the full life cycle of the capelin could readily be developed, and will prove a powerful tool when including the feeding migration into the interacting particle models.

The simulations of the Scenarios of Chapter 4 elicit unexpected behavior, seen in Figure 4.2(b). The emerging pattern is quite interesting and we have conjectured that the wave pattern is linked to the presence

of the radius of repulsion. A related observation is the fact that the eventual average number of neighbors is consistently higher than that expected from a uniform distribution. Chapter 4 thus provides us with interesting future research topics.

It should be noted that there is quite a variance in the relaxation times of the systems. We intend to further investigate these relaxation times, but without uniformly distributed directional angles. An interesting scenario would be to set all directional angles to zero, thus the system will then initially be completely aligned. By doing so, we would be better able to determine how quickly the system relaxes to the equilibrium pattern seen in Figure 4.2(b), which we discussed in Section 4.7.

However, it should be noted that the migrations of the capelin are inherently transient. Constantly varying external influences, such as temperature and currents, all act to prevent the schools of fish from obtaining the coherent equilibrium states of Chapter 4. It would therefore be of interest to further investigate the transient behavior.

Future computational powers will allow us to model with more and more particles. As mentioned in Chapter 4 we would optimally simulate at the level of individuals, but for now need to employ superindividuals. With more and more particles, the effectiveness of propagation of information through a school increases. Once the maximum number of particles is reached, other questions become more important to answer, such as the time step, reaction times, and the values of the weight factors, α and β .

It is my belief that modeling individuals, rather than a population as a whole, is realistic and a biologically feasible way of modeling living organisms. While many population models are in good agreement with observations for certain species, they are not a true description of nature in the sense that they treat populations as a single continuous entity. They are rather, in agreement with the outcome of a set of (very complex)

interactions between the individuals within the population. Modeling these interactions and behavior at the individual level is a more realistic approach to population dynamics.

Modeling at the population level must include assumptions about the behavior of a group of individuals as they were one entity. How can this be the case in real life, e.g. to what extent does an individual capelin take into account the state of the whole population when deciding how to spend its day? It should seem impossible for the individual to obtain that information, where distances are vast, as is the case in the ocean. Furthermore, different characteristic traits amongst individuals are hard to incorporate into continuous density models.

In real life, populations do not act as a single entity, but rather the actions of the individuals determine the behavior of the whole. By modeling at the individual level we obtain a much more powerful tool to understand the dynamics of the population of individuals. The behavior of individuals is much more directly observable and easier to model than the actions of a great number of individuals.

Population models are limited in that respect as the results are based on some assumptions on the population as a single entity. Additionally, at the individual level we obtain a powerful tool to predict what changes in the environment and individual behavior has on the whole population. Once we understand what effect the behavior of individuals has on the behavior of the whole population do we start to fully understand its behavior.

A

Appendix A

A.1 State variables and basic equations

We now derive the Equations (5.5)-(5.8) from the underlying state variables of the DEB model, E , V , E_H and E_R , which denote the *reserve energy*, *structural volume*, *maturity energy* and *reproduction energy*, respectively. The derivation is based on the equations and assumptions in [38].

A.1.1 Reserve energy

The reserve energy, E , is the energy available to the organism. Its source is food uptake and is the energy an organism utilizes for growth and somatic maintenance on one hand, and maturity, reproduction and maturity maintenance on the other hand. This division is further explained in Section 5.2.1 and in Figure 5.1.

We have the simple equation describing the inner dynamics of the reserves:

$$\frac{dE}{dt} = p_A - p_C \tag{A.1}$$

i.e. the difference between the assimilated energy and the utilized one, shown in Figure 5.1.

A.1.2 Volume, V , and volumetric length, L

The structural volume of an individual, V , denotes the volume of structural biomass. The equation governing the energy utilization of an individual is

$$\kappa p_C = [E_G] \frac{dV}{dt} + p_M \quad (\text{A.2})$$

where $[E_G]$ is the volume-specific cost of structure. By rewriting this equation we obtain another one which describes the growth of an individual:

$$\frac{dV}{dt} = \frac{\kappa p_C - p_M}{[E_G]} \quad (\text{A.3})$$

In addition, we define $L := V^{1/3}$ as the volumetric length of the individual. We note that L does not correspond to the physical length of an individual, but the relationship between the two is explained in Section 5.4.1. This distinction we will clarify by using the terms volumetric length and physical length.

A.1.3 Maturity energy and reproduction energy

As mentioned in Section 5.2.2, we introduce the variable E_H , which denotes a maturity energy, in order to determine the onset of puberty, see Figure 5.1. Initially, the energy from $(1 - \kappa)p_C - p_J$ is allocated to this variable, and the maturity maintenance will be a fraction of this energy, $k_J E_H$. When E_H exceeds a certain threshold, E_H^p , the fish is mature and allocation of energy to E_H ceases.

After puberty has been reached, the energy starts to flow to E_R , which is the total energy available for reproduction. This energy will, in turn, be converted into roe. We assume that there are no maintenance costs

related to roe, and the maintenance costs of E_R are proportional to E_H^p .

We note that the dynamics of the energy flow to maturity is the same as that to reproduction. In other words, both dE_H/dt and dE_R/dt have the same form, except that the former one is nonzero when $E_H < E_H^p$ but after that point is reached, the latter flow becomes nonzero. Thus, E_H reaches a final value E_H^p which determines when an individual reaches maturity, and that is neither determined by the volumetric length, nor the physical length of a fish.

The basic non-zero dynamics of E_H and E_R are the following:

$$\frac{d}{dt}E_* = (1 - \kappa)p_C - p_J \quad (\text{A.4})$$

where $*$ refers to either H or R depending on whether E_H has exceeded E_H^p or not.

Thus, the basic differential equations for the initial state variables in Table A.1 are as follows:

$$\frac{d}{dt}E = p_A - p_c \quad (\text{A.5})$$

$$\frac{d}{dt}V = \frac{\kappa p_C - p_M}{[E_G]} \quad (\text{A.6})$$

$$\frac{d}{dt}E_H = \begin{cases} (1 - \kappa)p_C - p_J, & E_H < E_H^p \\ 0, & \text{otherwise} \end{cases} \quad (\text{A.7})$$

$$\frac{d}{dt}E_R = \begin{cases} 0, & E_H < E_H^p \\ (1 - \kappa)p_C - p_J, & \text{otherwise} \end{cases} \quad (\text{A.8})$$

where E_H^p is the maturity energy required for the onset of puberty.

Table A.1: State variables and derived state variables of the standard DEB model.

E	J	Reserve energy
V	cm^3	structural volume
E_H	J	Maturity energy
E_R	J	Reproduction energy
$[E] := E/V$	J cm^{-3}	Reserve energy density
$L := V^{1/3}$	cm	Volumetric length
$U_H := E_H/\{p_{Am}\}$	$\text{cm}^2 \text{ d}$	Modified maturity energy
$U_R := E_R/\{p_{Am}\}$	$\text{cm}^2 \text{ d}$	Modified reproduction energy
$e := [E]/[E_m]$	-	Scaled energy density
$l := L/L_m$	-	Scaled volumetric length
$u_H := U_H\{p_{Am}\}/([E_m]L_m^3)$	-	Scaled maturity energy
$u_R := U_R\{p_{Am}\}/([E_m]L_m^3)$	-	Scaled reproduction energy

Table A.2: Parameters of the DEB model, see Figure 5.1

κ	-	Fraction of energy to growth and somatic maintenance
κ_R	-	reproduction efficiency
k_J	d^{-1}	Specific maturity maintenance
p_A	J d^{-1}	Assimilations rate of energy from food
$\{p_{Am}\}$	$\text{J d}^{-1} \text{ cm}^{-2}$	Maximum assimilation rate per surface area
$[p_A]$	$\text{J d}^{-1} \text{ cm}^{-3}$	Volume-specific assimilation rate
p_C	J d^{-1}	Reserve utilization rate
p_M	J d^{-1}	Somatic maintenance rate
$[p_M]$	$\text{J d}^{-1} \text{ cm}^{-3}$	Volume-specific somatic maintenance rate
p_J	J d^{-1}	Maturity maintenance rate
p_H	J d^{-1}	Maturity energy rate
p_R	J d^{-1}	Reproduction rate
$[E_G]$	J cm^{-3}	Volume-specific cost of structure
$[E_M]$	J cm^{-3}	Maximum reserve energy density

A.2 Further derivations

A.2.1 Assimilation and maintenance rates, p_A and p_M

An assumption of the DEB theory is that the functional response to food, f , is of the form

$$f = \frac{X}{X + X_K} \quad (\text{A.9})$$

where X is the food density and X_K is a saturation coefficient. There is a variety of functional responses available, but for now we choose the one above.

Now, we assume that the assimilation rate of food is proportional to the surface area of the animal, according to

$$p_A = \{p_{Am}\}fL^2 \quad (\text{A.10})$$

where $\{p_{Am}\}$ is the maximum area-specific assimilation rate. This comes from the assumption that the ingestion rate is proportional to the size of the mouth of the capelin, which indeed grows as the surface area of the individual.

Finally, we have $[p_M]$ as the volume-specific maintenance rate, thus

$$p_M = [p_M]V. \quad (\text{A.11})$$

A.2.2 Maximum length

Let L_m denote the maximum sustainable length of an individual at optimal food conditions, $f = 1$. Assuming that this holds when the maximum size is reached, we have an equilibrium between the assimilation rates and the maintenance rates. So, with the κ -rule in mind, the Equations (A.10)

and (A.11) give us a formulation of the maximum length:

$$[p_M]L_m^3 = \kappa\{p_{Am}\}L_m^2, \quad (\text{A.12})$$

where on the left hand side we have the maximum maintenance rate, and on the right we have the κ fraction of the maximum assimilation rate used for maintenance. This yields the formula for the maximum volumetric length of individuals:

$$L_m = \frac{\kappa\{p_{Am}\}}{[p_M]}. \quad (\text{A.13})$$

A.2.3 Reserve energy density, $[E]$

Now, we set $[E] = E/V$ as the reserve energy density of an individual. Then from (A.1) and (A.10) we get

$$\begin{aligned} \frac{d}{dt}[E] &= \frac{d}{dt}\left(\frac{E}{V}\right) \\ &= \frac{1}{V}\frac{dE}{dt} - \frac{E}{V^2}\frac{dV}{dt} \\ &= \frac{1}{V}\left(p_A - p_C - [E]\frac{dV}{dt}\right) \\ &= \frac{1}{V}\{p_{Am}\}fL^2 - \frac{1}{V}\left(p_C + [E]\frac{dV}{dt}\right) \\ &= \frac{\{p_{Am}\}f}{L} - \frac{1}{V}\left(p_C + [E]\frac{dV}{dt}\right). \end{aligned} \quad (\text{A.14})$$

We assume that the dynamics of the reserve density is a first degree homogenous function [38], thus requiring the second part of Equation (A.14) to be of the form $c[E]$, where c is a constant:

$$\frac{d}{dt}[E] = \frac{\{p_{Am}\}f}{L} + c[E]. \quad (\text{A.15})$$

At constant food abundances, $f = 1$, we furthermore assume that the dynamics of the energy densities asymptotically reach a maximum value $[E_m]$ at $\frac{d}{dt}[E] = 0$. Thus, from (A.15) we have

$$c = \frac{\{p_{Am}\}}{L[E_m]}. \quad (\text{A.16})$$

This gives the final form of Equation (A.14) for the scaled reserve energy density

$$\frac{d[E]}{dt} = \frac{\{p_{Am}\}}{L} \left(f - \frac{[E]}{[E_m]} \right). \quad (\text{A.17})$$

A.2.4 Volumetric length, L

We now further detail the dynamics of the volumetric length. First, we obtain an expression for the reserve utilization rate, p_C , from Equations (A.1) and (A.17):

$$\begin{aligned} p_C &= p_A - \frac{dE}{dt} \\ &= p_A - V \frac{d[E]}{dt} - [E] \frac{dV}{dt} \\ &= p_A - V \frac{\{p_{Am}\}}{L} \left(f - \frac{[E]}{[E_m]} \right) - [E] \frac{dV}{dt} \\ &= L^2 \{p_{Am}\} \frac{[E]}{[E_m]} - [E] \frac{dV}{dt}. \end{aligned} \quad (\text{A.18})$$

Rewriting (A.3) as

$$p_C = \frac{1}{\kappa} \left([E_G] \frac{dV}{dt} + p_M \right) \quad (\text{A.19})$$

we solve together with (A.18), collecting terms of dV/dt on the left hand side:

$$\left(\frac{[E_G]}{\kappa} + [E]\right) \frac{dV}{dt} = \frac{V}{L} \{p_{Am}\} \frac{[E]}{[E_m]} - \frac{V}{\kappa} \frac{p_M}{V}, \quad (\text{A.20})$$

which with Equation (A.11) becomes

$$\frac{dV}{dt} = V \left(\frac{\frac{\{p_{Am}\}}{L} \frac{[E]}{[E_G]} - \frac{[p_M]}{\kappa}}{[E] + \frac{[E_G]}{\kappa}} \right). \quad (\text{A.21})$$

Now, we finally arrive at

$$\begin{aligned} \frac{d}{dt} L &= \frac{1}{3L^2} \frac{dV}{dt} \\ &= \frac{V}{3L^2} \{p_{Am}\} \frac{\left(\frac{[E]}{L[E_m]} - \frac{[p_M]}{\kappa\{p_{Am}\}} \right)}{[E] + \frac{[E_G]}{\kappa}} \end{aligned}$$

which with Equation (A.13) gives an equation for the dynamics of the volumetric length:

$$\frac{dL}{dt} = \frac{\{p_{Am}\}}{3} \frac{\frac{[E]}{[E_m]} - \frac{L}{L_m}}{[E] + \frac{[E_G]}{\kappa}}. \quad (\text{A.22})$$

A.2.5 Maturity energy and reproduction energy

We now modify the maturity energy, E_H , and the reserve energy, E_R and obtain equations for the dynamics of those modified variables.

First, rewrite Equation (A.3) as we did in Equation (A.19). By subsequently using Equations (A.11) and (A.21) we obtain a new expression for p_C :

$$p_C = \frac{1}{\kappa} \left([E_G] \frac{dV}{dt} + p_M \right)$$

$$\begin{aligned}
&= \frac{1}{\kappa} \left([E_G]V \frac{\{p_{Am}\} \frac{[E]}{L} \frac{[E]}{[E_m]} - \frac{[p_M]}{\kappa}}{[E] + \frac{[E_G]}{\kappa}} + p_M \right) \\
&= \frac{1}{\kappa} \frac{[E_G]L^2 \{p_{Am}\} \frac{[E]}{[E_m]} - \frac{[E_G]}{\kappa} [p_M]V + [E]p_M + \frac{[E_G]}{\kappa} p_M}{[E] + \frac{[E_G]}{\kappa}} \\
&= \frac{1}{\kappa} \frac{[E_G]L^2 \{p_{Am}\} \frac{[E]}{[E_m]} + [E][p_M]L^3}{[E] + \frac{[E_G]}{\kappa}} \\
&= \frac{[E]L^2 \{p_{Am}\} \frac{[E_G]}{[E_m]} + [p_M]L}{\kappa \left([E] + \frac{[E_G]}{\kappa} \right)}
\end{aligned}$$

i.e.

$$p_C = \frac{[E]L^2 \{p_{Am}\} \frac{[E_G]}{[E_m]} + [p_M]L}{\kappa \left([E] + \frac{[E_G]}{\kappa} \right)}. \quad (\text{A.23})$$

We now introduce the modified maturity energy

$$U_H := \frac{E_H}{\{p_{Am}\}} \quad (\text{cm}^2 \text{ d}). \quad (\text{A.24})$$

and the modified reproduction energy,

$$U_R := \frac{E_R}{\{p_{Am}\}} \quad (\text{cm}^2 \text{ d}). \quad (\text{A.25})$$

We assume that the maturity maintenance rate, p_J , is proportional to the maturity energy, E_H :

$$p_J = k_J E_H. \quad (\text{A.26})$$

Furthermore, we note that when puberty has been reached and roe production is in full swing, the maturity maintenance rate is fixed at $p_J = k_J E_H^p$, independent of the reproduction energy and the roe production.

The non-zero dynamics of Equations (A.7) and (A.8), coupled with

Equations (A.13) and (A.23), thus become

$$\begin{aligned}
\frac{d}{dt}U_* &= \frac{1}{\{p_{Am}\}} \frac{dE_*}{dt} \\
&= \frac{1}{\{p_{Am}\}} ((1 - \kappa)p_C - p_J) \\
&= \frac{1}{\{p_{Am}\}} (1 - \kappa) \frac{[E]L^2 \{p_{Am}\} \frac{[E_G]}{[E_m]} + [p_M]L}{\kappa [E] + \frac{[E_G]}{\kappa}} - k_J E_H \\
&= (1 - \kappa) [E] L^2 \frac{\frac{[E_G]}{\kappa [E_m]} + \frac{L}{\kappa \{p_{Am}\} / [p_M]}}{[E] + \frac{[E_G]}{\kappa}} - k_J \frac{E_H}{\{p_{Am}\}} \\
&= (1 - \kappa) \frac{[E]}{[E_m]} L^2 \frac{\frac{[E_G]}{\kappa [E_m]} + \frac{L}{L_m}}{\frac{[E]}{[E_m]} + \frac{[E_G]}{\kappa [E_m]}} - k_J U_H
\end{aligned}$$

where * denotes either H or R , depending on whether E_H has reached the threshold E_H^p or not.

Now, we introduce the parameter

$$\nu := \frac{\{p_{Am}\}}{[E_m]} \quad (\text{cm d}^{-1}) \quad (\text{A.27})$$

which is called *energy conductance*, and

$$g := \frac{[E_G]}{\kappa [E_m]} \quad (-) \quad (\text{A.28})$$

which is called *energy investment ratio*.

So far the Equations (A.5)-(A.8) have become

$$\frac{d[E]}{dt} = \frac{\{p_{Am}\}}{L} \left(f - \frac{[E]}{[E_m]} \right) \quad (\text{A.29})$$

$$\frac{dL}{dt} = \frac{\{p_{Am}\}}{3} \frac{\frac{[E]}{[E_m]} - \frac{L}{L_m}}{[E] + \frac{[E_G]}{\kappa}} \quad (\text{A.30})$$

$$\frac{dU_H}{dt} = \begin{cases} (1 - \kappa) \frac{[E]}{[E_m]} L^2 \frac{g + \frac{L}{L_m}}{\frac{[E]}{[E_m]} + g} - k_J U_H, & E_H < E_H^p \\ 0, & \text{otherwise} \end{cases} \quad (\text{A.31})$$

$$\frac{dU_R}{dt} = \begin{cases} 0, & E_H < E_H^p \\ (1 - \kappa) \frac{[E]}{[E_m]} L^2 \frac{g + \frac{L}{L_m}}{\frac{[E]}{[E_m]} + g} - k_J U_H^p, & \text{otherwise} \end{cases} \quad (\text{A.32})$$

where

$$U_H^p := \frac{E_H^p}{\{p_{Am}\}} \quad (\text{cm}^2 \text{ d}) \quad (\text{A.33})$$

is the modified maturity energy at puberty.

A.2.6 Primary parameters

In DEB modeling one often works with

$\{J_{EAm}\}$	mol d ⁻¹ cm ⁻²	Surface area specific assimilation rate
y_{VE}	-	Yield of structure from reserve on growth
ν	cm d ⁻¹	Energy conductance

as primary parameters. The parameters $\{p_{Am}\}$, $[E_G]$, $[E_m]$, and g , are determined from these parameters as

$$\{p_{Am}\} = \bar{\mu}_E \{J_{EAm}\} \quad (\text{A.34})$$

$$[E_m] = \frac{\bar{\mu}_E \{J_{EAm}\}}{\nu} \quad (\text{A.35})$$

$$[E_G] = \frac{\bar{\mu}_E [M_V]}{y_{VE}} \quad (\text{A.36})$$

$$g = \frac{\nu [M_V]}{\kappa \{J_{EAm}\} y_{VE}}, \quad (\text{A.37})$$

where

$\bar{\mu}_E$	J mol^{-1}	chemical potential
$[M_V]$	mol cm^{-3}	volume specific structural mass.

A.2.7 Dimensionless state variables

Finally, we introduce the dimensionless variables

$$e := \frac{[E]}{[E_m]} \quad (\text{A.38})$$

$$l := \frac{L}{L_m} \quad (\text{A.39})$$

$$u_H := U_H \frac{\nu}{L_m^3} = \frac{E_H}{[E_m]L_m^3} \quad (\text{A.40})$$

$$u_R := U_R \frac{\nu}{L_m^3} = \frac{E_R}{[E_m]L_m^3}. \quad (\text{A.41})$$

The dynamics of these dimensionless variables are as follows:

$$\begin{aligned} \frac{de}{dt} &= \frac{1}{[E_m]} \frac{d[E]}{dt} \\ &= \frac{1}{[E_m]} \frac{\{p_{Am}\}}{L \frac{L_m}{L_m}} \left(f - \frac{[E]}{[E_m]} \right) \\ &= \frac{\nu}{L_m l} (f - e), \end{aligned}$$

$$\begin{aligned} \frac{dl}{dt} &= \frac{1}{L_m} \frac{dL}{dt} \\ &= \frac{1}{L_m} \frac{\{p_{Am}\}}{3} \frac{\frac{[E]}{[E_m]} - \frac{L}{L_m}}{\frac{[E]}{[E_m]} + \frac{[E_G]}{\kappa}} \\ &= \frac{\{p_{Am}\}/[E_m]}{3L_m} \frac{e - l}{\frac{[E]}{[E_m]} + \frac{[E_G]}{\kappa[E_m]}} \end{aligned}$$

$$= \frac{\nu}{3L_m} \frac{e-l}{e+g},$$

and finally for the non-zero dynamics of the reproduction variables:

$$\begin{aligned} \frac{du_*}{dt} &= \frac{\nu}{L_m^3} \frac{dU_*}{dt} \\ &= \frac{\nu}{L_m} (1-\kappa) e l^2 \frac{g+l}{e+g} - k_J \frac{\nu}{L_m^3} U_H \\ &= \frac{\nu}{L_m} (1-\kappa) e l^2 \frac{g+l}{e+g} - k_J u_H, \end{aligned}$$

where $*$ denotes H or R as before.

Similarly as before, we let

$$u_H^p := U_H^p \frac{\nu}{L_m^3} = \frac{E_H^p}{[E_m] L_m^3} \quad (\text{A.42})$$

and we have turned the Equations (A.5)-(A.8) into the following dimensionless equations:

$$\frac{de}{dt} = \frac{\nu}{L_m l} (f - e) \quad (\text{A.43})$$

$$\frac{dl}{dt} = \frac{\nu}{3L_m} \frac{e-l}{e+g} \quad (\text{A.44})$$

$$\frac{du_H}{dt} = \begin{cases} \frac{\nu}{L_m} (1-\kappa) e l^2 \frac{l+g}{e+g} - k_J u_H, & u_H < u_H^p \\ 0, & \text{otherwise} \end{cases} \quad (\text{A.45})$$

$$\frac{du_R}{dt} = \begin{cases} 0, & u_H < u_H^p \\ \frac{\nu}{L_m} (1-\kappa) e l^2 \frac{l+g}{e+g} - k_J u_H^p, & \text{otherwise} \end{cases} \quad (\text{A.46})$$

B

Appendix B

B.1 DEB and von Bertalanffy growth equations

We now show that the well known growth equations of von Bertalanffy can be derived from the DEB model. The derivation is based on that in [38].

At constant food density, f , as in Section A.2.3, the energy density, $[E]$, reaches a steady state, assuming that the organism ingests at a constant healthy rate. Then from Equation (5.5) we see that $\frac{de}{dt} = 0$ gives $e = f$. Substituting that into Equation (5.6) and setting

$$k := \frac{\nu}{3L_m(f + g)} \tag{B.1}$$

we get

$$\frac{dl}{dt} = k(f - l). \tag{B.2}$$

From Equation (B.2) we get from separating variables

$$\begin{aligned}\int \frac{dl}{f-l} &= k \int dt \\ -\ln|f-l| &= k(t+c), \quad c \in \mathbb{R} \text{ (constant)} \\ f-l &= e^{-k(t+c)} \\ l &= f - e^{-kc} e^{-kt}\end{aligned}$$

i.e.

$$l(t) = f - \zeta e^{-kt} \quad (\text{B.3})$$

where $\zeta \in \mathbb{R}_+$, constant. Here we have assumed that $f > l$ because the organism is growing, allowing us to drop the absolute value in the natural log above.

When determining the constant ζ , we require $l(0) = l_0$ at time $t = 0$, where l_0 is the length of an individual at the end of the larval stage. Thus,

$$l_0 = f - \zeta, \quad (\text{B.4})$$

giving

$$l(t) = f - (f - l_0)e^{-kt}. \quad (\text{B.5})$$

We can now find the time t_0 when an individual has length zero:

$$0 = f - (f - l_0)e^{-kt_0} \quad (\text{B.6})$$

$$e^{-kt_0} = \frac{f}{f - l_0} \quad (\text{B.7})$$

i.e.

$$t_0 = \frac{1}{k} \ln \left(1 - \frac{l_0}{f} \right). \quad (\text{B.8})$$

We note that $|t_0|$ corresponds to the development time of larvae at con-

stant food conditions. Substituting (B.7) into (B.5) we get

$$\begin{aligned}
 l(t) &= f - (f - l_0)e^{-kt}e^{kt_0}e^{-kt_0} \\
 &= f - (f - l_0)e^{-kt}e^{kt_0}\frac{f}{f - l_0} \\
 &= f - (f - l_0)e^{-kt}e^{kt_0}\frac{f}{f - l_0} \\
 &= f(1 - e^{-k(t-t_0)}),
 \end{aligned}$$

i.e.

$$l(t) = f(1 - e^{-k(t-t_0)}). \quad (\text{B.9})$$

And now, letting \mathfrak{L} denote the physical length of an individual and L the volumetric length, we have from Equation (5.16)

$$\mathfrak{L} = \frac{L_m}{\delta}l. \quad (\text{B.10})$$

We let \mathfrak{L}_∞ denote the maximum physical length of an individual at food response f . We have

$$\lim_{t \rightarrow \infty} l(t) = f, \quad (\text{B.11})$$

thus

$$\mathfrak{L}_\infty = \frac{L_m f}{\delta}. \quad (\text{B.12})$$

We also have the physical length at time $t = 0$:

$$\mathfrak{L}_0 := \frac{L_m l_0}{\delta}. \quad (\text{B.13})$$

The Equations (B.5), (B.10) and (B.12) now yield

$$\begin{aligned}
 \mathfrak{L} &= \frac{L_m}{\delta} (f - (f - l_0)e^{-kt}) \\
 &= \mathfrak{L}_\infty - (\mathfrak{L}_\infty - \mathfrak{L}_0)e^{-kt}
 \end{aligned} \quad (\text{B.14})$$

and similarly as above we get

$$\mathfrak{L} = \mathfrak{L}_\infty(1 - e^{-k(t-t_0)}), \quad (\text{B.15})$$

where

$$t_0 = \frac{1}{k} \ln \left(1 - \frac{\mathfrak{L}_0}{\mathfrak{L}_\infty} \right). \quad (\text{B.16})$$

Now, from (B.1) and (B.12) we have

$$\begin{aligned} \frac{1}{k} &= \frac{2L_m}{\nu}(f + g) \\ &= \frac{3L_m f}{\nu} + \frac{3L_m g}{\nu} \\ &= 3 \left(\frac{\mathfrak{L}_\infty \delta L_m g}{\nu} \right). \end{aligned}$$

From Equations (A.13), (A.27), and (A.28) we see that

$$\frac{L_m g}{\nu} = \frac{[E_G]}{[p_M]}. \quad (\text{B.17})$$

We therefore introduce the parameter

$$k_M := \frac{[p_M]}{[E_G]} \quad (\text{d}^{-1}) \quad (\text{B.18})$$

as the maintenance rate coefficient and get

$$\frac{1}{k} = 3 \left(\frac{\mathfrak{L}_\infty}{\nu} \frac{1}{k_M} \right). \quad (\text{B.19})$$

We have thus established connections between the DEB theory and the well known von Bertalanffy growth parameters. We note that we have implicitly described how k and t_0 depend on temperature. They both depend on ν , which is a biological rate which is affected by temperature according to Equation (5.14). However, the growth rates assume

constant feeding conditions, which does not apply to the life span of capelin. The von Bertalanffy growth equations could still be used to describe the earlier life stages of capelin, where they do experience more stable food conditions.

Bibliography

- [1] J. A. ANTHONY, D. D. ROBY, AND K. R. TURCO, *Lipid content and energy density of forage fishes from the northern Gulf of Alaska*, Journal of Experimental Marine Biology and Ecology, 248 (2000), pp. 53–78.
- [2] I. AOKI, *A Simulation Study on the Schooling Mechanism in Fish*, Bulletin of the Japanese Society of Scientific Fisheries, 48 (1982), pp. 1081–1088.
- [3] A. BARBARO, B. EINARSSON, B. BIRNIR, S. SIGURÐSSON, H. VALDIMARSSON, Ó. K. PÁLSSON, S. SVEINBJÖRNSSON, AND Þ. SIGURÐSSON, *Modelling and Simulations of the Migration of Pelagic Fish*, ICES Journal of Marine Science, 66 (2009), pp. 826–838.
- [4] —, *Simulations and scaling laws for a bioenergetic model of the Icelandic capelin stock*, in Proceedings of the 2009 ICES Conference, D. Secor, P. Petitgas, I. McQuinn, and S. Cadrin, eds., Berlin, 2009.
- [5] A. B. T. BARBARO, *An interacting particle model for the migrations of pelagic fish*, PhD thesis, University of California, Santa Barbara, 2008.
- [6] A. B. T. BARBARO, K. TAYLOR, P. TRETHERWEY, L. YOUSEFF, AND B. BIRNIR, *Discrete and continuous models of the behavior of*

- pelagic fish: applications to the capelin*, Mathematics and Computers in Simulation, 79 (2009), pp. 3397–3414.
- [7] B. BIRNIR, *An ODE model of the motion of pelagic fish*, Journal of Statistical Physics, 128 (2007), pp. 535–568.
- [8] J. BUHL, D. J. T. SUMPTER, I. D. COUZIN, J. J. HALE, E. DESPLAND, E. R. MILLER, AND S. J. SIMPSON, *From disorder to order in marching locusts*, Science, 312 (2006), pp. 1402–1406.
- [9] M. BULMER, *Theoretical Evolutionary Ecology*, Sinauer, Sunderland, 1994.
- [10] J. E. CARSCADDEN, B. S. NAKASHIMA, AND K. T. FRANK, *Effects of fish length and temperature on the timing of peak spawning in capelin (Mallotus villosus)*, Canadian Journal of Fisheries and Aquatic Sciences, 54 (1997), pp. 781–787.
- [11] Y. L. CHUANG, M. R. D’ORSOGNA, D. MARTHALER, A. L. BERTOZZI, AND L. S. CHAYES, *State transitions and the continuum limit for a 2d interacting, self-propelled particle system*, Physica D, 232 (2007), pp. 33–47.
- [12] I. D. COUZIN, J. KRAUSE, R. JAMES, G. RUXTON, AND N. FRANKS, *Collective memory and spatial sorting in animal groups*, Journal of Theoretical Biology, 218 (2002), pp. 1–11.
- [13] A. CZIRÓK, H. E. STANLEY, AND T. VICSEK, *Spontaneously ordered motion of self-propelled particles*, Journal of Physics A, 30 (1997), pp. 1375–1385.
- [14] A. CZIRÓK, M. VICSEK, AND T. VICSEK, *Collective motion of organisms in three dimensions*, Physica A, 264 (1999), pp. 299–304.

- [15] A. CZIRÓK AND T. VICSEK, *Collective behaviour of interacting self-propelled particles*, *Physica A*, 281 (2000), pp. 17–29.
- [16] M. R. D'ORSOGNA, Y. L. CHUANG, A. L. BERTOZZI, AND L. S. CHAYES, *Self-propelled particles with soft-core interactions: pattern, stability, and collapse*, *Physical Review Letters*, 96 (2006), p. 104302.
- [17] B. EINARSSON, A. BARBARO, B. BIRNIR, AND S. SIGURÐSSON, *Scaling behavior in an interactive particly system*, In preparation.
- [18] B. EINARSSON, B. BIRNIR, AND SIGURÐSSON, *A Dynamic Energy Budget (DEB) model for the energy usage and reproduction of the Icelandic capelin (Mallotus villosus)*, *Journal of Theoretical Biology*, (To appear).
- [19] Ó. FIKSEN, J. GISKE, AND D. SLAGSTAD, *A spatially explicit fitness-based model of capelin migrations in barents sea*, *Fisheries Oceanography*, 4 (1995), pp. 193–208.
- [20] K. T. FRANK AND W. C. LEGGETT, *Prediction of egg development and mortality rates in capelin (mallotus villosus) from meteorological, hydrographic, and biological factors*, *Canadian Journal of Fisheries and Aquatic Sciences*, 38 (1981), pp. 1327–1338.
- [21] E. FRIDGEIRSSON, *Observations on Spawning Behaviour and Embryonic Development of the Icelandic Capelin*, *Journal of the Marine Research Institute Reykjavik*, V (1976).
- [22] M. GISSURARSON, H. MAGNÚSSON, R. SVEINÞÓRSDÓTTIR, AND C. GARATE, *Compilation of previous test results of capelin roes*, report, Matis Food Research, Innovation and Safety, 2009.

- [23] H. GJØSÆTER, *The population biology and exploitation of capelin (Mallotus villosus) in the Barents sea*, Sarsia, 83 (1998), pp. 453–496.
- [24] H. GJØSÆTER, A. DOMMASNES, AND I. RØTTINGEN, *The Barents sea capelin stock 1972-1997. A synthesis of results from acoustic surveys*, Sarsia, 83 (1998), pp. 497–510.
- [25] D. GRÜNBAUM, S. VISCIDO, AND J. K. PARRISH, *Extracting Interactive Control Algorithms from Group Dynamics of Schooling Fish*, vol. 309, Springer-Verlag, 2004, pp. 103–117.
- [26] Á. GUÐMUNSDÓTTIR AND H. VILHJÁLMSOON, *Predicting total allowable catches for Icelandic capelin, 1978-2001*, ICES Journal of Marine Science, 59 (2002), pp. 1105–1115.
- [27] C. K. HEMELRIJK AND H. HILDENBRANDT, *Self-Organized Shape and Frontal Density of Fish Schools*, Ethology, 114 (2008), pp. 245–254.
- [28] C. K. HEMELRIJK AND H. KUNZ, *Density distribution and size sorting in fish schools: an individual-based model*, Behavioral Ecology, 16 (2005), pp. 178–187.
- [29] H. HILDENBRANDT, C. CARERE, AND C. K. HEMELRIJK, *Self-organized aerial displays of thousands of starlings: a model*, Behavioral Ecology, 21 (2010), pp. 1349–1359.
- [30] S. HUBBARD, P. BABAK, S. SIGURÐSSON, AND K. G. MAGNÚSSON, *A model of the formation of fish schools and migration of fish*, Ecological Modelling, 174 (2004), pp. 359–374.
- [31] G. HUSE, *Modelling habitat choice in fish using adapted random walk*, Sarsia, 86 (2001), pp. 477–483.

- [32] G. HUSE, G. JOHANSEN, L. BOGSTAD, AND H. GJØSÆTER, *Studying spatial and trophic interactions between capelin and cod using individual-based modelling*, ICES Journal of Marine Science, 61 (2004), pp. 1201–1213.
- [33] G. HUSE, E. STRAND, AND J. GISKE, *Implementing behaviour in individual-based models using neural networks and genetic algorithms*, Evolutionary Ecology, 13 (1999), pp. 469–483.
- [34] A. HUTH AND C. WISSEL, *The Simulation of the Movement of Fish Schools*, Journal of Theoretical Biology, 156 (1992), pp. 365–385.
- [35] —, *The Simulation of Fish Schools in comparison with experimental data*, Ecological Modelling, 75 (1994), pp. 135–146.
- [36] S. A. L. M. KOOIJMAN, *Dynamic Energy and Mass Budgets in Biological Systems*, Cambridge University Press, Cambridge, 2000.
- [37] —, *Quantitative aspects of metabolic organization: a discussion of concepts*, Philosophical transactions of the Royal Society of London B, 356 (2001), pp. 331–349.
- [38] —, *Dynamic Energy Budget Theory For Metabolic Organisation*, Cambridge University Press, Cambridge, 2010.
- [39] S. A. L. M. KOOIJMAN, T. SOUSA, L. PECQUERIE, J. VAN DER MEER, AND T. JAGER, *From food-dependent statistics to metabolic parameters, a practical guide to the use of dynamic energy budget theory*, Biological Reviews, 83 (2008), pp. 533–552.
- [40] H. KUNZ AND C. K. HEMELRIJK, *Artificial fish schools: collective effects of school size, body size, and body form*, Artificial Life, 9 (2003).

- [41] H. KUNZ, T. ZÜBLIN, AND C. K. HEMELRIJK, *On prey grouping and predator confusion in artificial fish schools* in *Proceedings of the Tenth International Conference of Artificial Life*, MIT Press, Cambridge, MA, 2006.
- [42] Y. KURAMOTO, *Self-entrainment of a population of coupled nonlinear oscillators*, *Lecture Notes in Physics*, 39 (1975), p. 420.
- [43] K. LOGEMANN AND I. HARMS, *High resolution modelling of the North Icelandic Irminger Current (NIIC)*, *Ocean Science*, 2 (2006), pp. 291–304.
- [44] K. MAGNÚSSON AND T. ASPELUND, *A model for estimating meal frequency and meal size from stomach data with an application to Atlantic cod (Gadus morhua) feeding on capelin (Mallotus villosus)*, *Canadian Journal of Fisheries and Aquatic Sciences*, 54 (1997), pp. 876–889.
- [45] K. MAGNÚSSON AND Ó. PÁLSSON, *Predator-prey interactions of cod and capelin in Icelandic waters.*, *ICES Marine Science Symposium*, 193 (1991), pp. 153–170.
- [46] K. G. MAGNÚSSON, S. SIGURÐSSON, P. BABAK, S. F. GUÐMUNDSSON, AND E. H. DEREKSDÓTTIR, *A continuous density Kolmogorov type model for a migrating fish stock*, *Discrete and Continuous Dynamical Systems-Series B*, 4 (2004), pp. 695–704.
- [47] K. G. MAGNÚSSON, S. SIGURÐSSON, AND E. H. DEREKSDÓTTIR, *A simulation model for capelin migrations in the North-Atlantic*, *Nonlinear Analysis-Real World Applications*, 6 (2005), pp. 747–771.
- [48] K. G. MAGNÚSSON, S. SIGURÐSSON, AND B. EINARSSON, *A discrete and stochastic simulation model for migration of fish with appli-*

- cation to capelin in the seas around Iceland*, Tech. Rep. RH-20-2004, Science Institute, University of Iceland, 2004.
- [49] O. A. MISUND, H. VILHJÁLMSSON, S. H. Í JÁKUPSSTOFU, I. RØTTINGEN, S. BELIKOV, Ó. ÁSTÞÓRSSON, J. BLINDHEIM, J. JÓNSSON, A. KRYSOV, S. A. MALMBERG, AND S. SVEINBJÖRNSSON, *Distribution, migration and abundance of Norwegian spring spawning herring in relation to the temperature and zooplankton biomass in the Norwegian sea as recorded by coordinated surveys in spring and summer 1996*, Sarsia, 83 (1998), pp. 117–127.
- [50] L. MOTOS, *Reproductive biology and fecundity of the Bay of Biscay anchovy populations (Engraulis engrasicolus L.)*, Scientia Marina, 60 (1996), pp. 195–2–7.
- [51] R. M. NISBET, E. B. MULLER, K. LIKA, AND S. A. L. M. KOOLJMAN, *From molecules to ecosystems through dynamic energy budget models*, Journal of Animal Ecology, 69 (2000), pp. 913–926.
- [52] B. PARTRIDGE, *The structure and function of fish schools*, Scientific American, 246 (1982), pp. 114–123.
- [53] B. PARTRIDGE AND T. PITCHER, *The sensory basis of fish schools - relative roles of lateral line and vision*, Journal of Comparative Physiology, 135 (1980), pp. 315–325.
- [54] L. PECQUERIE, 2009. www.bio.vu.nl/thb/deb/deblab/add_my_pet/...pars_Engraulis_encrasicolus.m Last accessed March 15 2011.
- [55] L. PECQUERIE, R. M. NISBET, R. FABLET, A. LORRAIN, AND S. KOOLJMAN, *The impact of metabolism on stable isotope dynamics: a theoretical framework*, Philosophical transactions of the Royal Society of London B, 365 (2010), pp. 3455–3468.

- [56] L. PECQUERIE, P. PETITGAS, AND S. KOUIJMAN, *Modeling fish growth and reproduction in the context of the dynamic energy budget theory to predict environmental impact on anchovy spawning duration*, *Journal of Sea Research*, 62 (2009), pp. 93–105.
- [57] M. REED AND J. G. BALCHEN, *A multidimensional continuum model of fish population-dynamics and behaviour: Application to the Barents Sea capelin (Mallotus Villosus)*, *Modeling Identification and Control*, 3 (1982), pp. 65–109.
- [58] S. SIGURÐSSON, K. G. MAGNÚSSON, P. BABAK, S. F. GUÐMUNDSSON, AND E. H. DEREKSDÓTTIR, *Dynamic continuous model of fish migration*, Tech. Rep. RH-25-2002, Science Institute, University of Iceland, 2002.
- [59] T. SOUSA, T. DOMINGOS, AND S. A. L. M. KOUIJMAN, *From empirical patterns to theory: a formal metabolic theory of life*, *Philosophical Transactions of the Royal Society*, 363 (2008), pp. 2453–2464.
- [60] C. M. TOPAZ, A. L. BERTOZZI, AND M. A. LEWIS, *A nonlocal continuum model for biological aggregation*, *Bulletin of Mathematical Biology*, 68 (2006), pp. 1601–1623.
- [61] J. VAN DER MEER, *An introduction to Dynamic Energy Budget (DEB) models with special emphasis on parameter estimation*, *Journal of Sea Research*, 56 (2006), pp. 85–102.
- [62] H. VAN DER VEER, S. KOUIJMAN, AND J. VAN DER MEER, *Intra- and interspecies comparison of energy flow in North Atlantic flat-fish species by means of dynamic energy budgets*, *Journal of Sea Research*, 45 (2001), pp. 303–320.

- [63] T. VICSEK, A. CZIRÓK, E. BEN-JACOB, I. COHEN, AND O. SHOCHET, *Novel type of phase transition in a system of self-driven particles*, Physical Review Letters, 75 (1995), pp. 1226–1229.
- [64] H. VILHJÁLMSOON, *The Icelandic capelin stock*, Journal of the Marine Research Institute Reykjavik, XIII (1994), p. 281 pp.
- [65] —, *Capelin (Mallotus villosus) in the Iceland-East Greenland-Jan Mayen ecosystem.*, ICES Journal of Marine Science, 59 (2002), pp. 870–883.
- [66] —, 2008. Personal communication.
- [67] H. VILHJÁLMSOON AND J. E. CARSCADDEN, *Assessment surveys for capelin in the Iceland-East Greenland-Jan Mayen area, 1978-2001*, ICES Journal of Marine Science, 59 (2002), pp. 1096–1104.
- [68] S. V. VISCIDO, J. K. PARRISH, AND D. GRÜNBAUM, *Individual behavior and emergent properties of fish schools: a comparison of observation and theory*, Marine Ecology Progress Series, 273 (2004), pp. 239–249.
- [69] —, *The effect of population size and number of influential neighbors on the emergent properties of fish schools*, Ecological Modelling, 183 (2005), pp. 347–363.
- [70] L. M. YOUSEFF, A. B. T. BARBARO, P. F. TRETHERWEY, B. BIRNIR, AND J. GILBERT, *Parallel modeling of fish interaction*, IEEE 11th International Conference on Computational Science and Engineering, (2008), pp. 231–241.

